Institut für Theoretische Physik

Universität zu Köln

Skyrmions in Chiral Magnets: The Influence of Vacancies

Master Thesis
Supervisor Prof. Dr. Achim Rosch

by
Jan Müller
Matrikel 5035678

June 2014, Köln

Contents

1. An Introduction to Skyrmions

1.1. Skyrmions in Chiral Magnets

Skyrmions were originally introduced by Tony Skyrme in the early 1960's as topological non-trivial quasi-particles in certain field theories [1]. Later, skyrmions appeared in various different fields of physics and also have been suggested by Bogdanov *et al.* [2] to appear as a metastable state in anisotropic non-centrosymmetric magnetic materials with chiral spin-orbit interactions in a magnetic field. The real break-through for skyrmions in solid state physics then happened in 2009 after the discovery of the magnetic skyrmion lattice in cubic chiral magnets by Mühlbauer *et al* [3]. For the phasediagram see figure 1.2. In these magnets the chiral B20 atomic crystal structure allows to include a Dzyaloshinskii-Moriya interaction term which in two dimensions is

$$H_{\mathrm{DMI}} = \int \mathrm{d}^2 r D\mathbf{M}(\mathbf{r}) \cdot [\nabla \times \mathbf{M}(\mathbf{r})] \tag{1.1}$$

with the continuous magnetization $\mathbf{M}(\mathbf{r})$ and the DMI coupling constant D and which results from spin-orbit interaction. This interaction term favours twisting the magnetic structure in a given handedness and hence can lead to an energetic stabilization of helices or chiral skyrmions. After the first discovery of skyrmion lattices they were found in many different types of B20 compounds such as the metals MnSi [3, 4] and FeGe [5], the semiconductor $Fe_{1-x}Co_xSi$ [6, 7] or even the insulator Cu_2OSeO_3 [8].
The magnetic skyrmions mainly gained such a broad attention due to their topological properties: the skyrmion obeys an integer winding number $\mathcal{W}$ which in two dimensions is defined as

$$\mathcal{W} = \frac{1}{4\pi} \int \mathrm{d}(x, y) \hat{\mathbf{M}} \left(\partial_x \hat{\mathbf{M}} \times \partial_y \hat{\mathbf{M}} \right) \tag{1.2}$$

with the unit vector in the direction of the magnetization $\hat{\mathbf{M}} = \mathbf{M}/|\mathbf{M}|$. This topological winding number is illustrated in figure 1.1, where it is shown how to map the magnetic structure of a chiral skyrmion onto a hedgehog: the hedgehog gets 'combed', meaning every spin is rotated around the axis connecting an arbitrary north and south pole, and afterwards is projected down to the two-dimensional plane. The combing here is not an essential step when building a skyrmion: a simple projection of the hedgehog down to the plane would also yield a skyrmion, but it would not be chiral. As in this thesis we want to explicitly work with the DM interaction resulting from the chirality of the underlying lattice structure, and hence with chiral skyrmions, in the following the term *chiral* is omitted if not stated otherwise.
The topological winding number defined in equation 1.2 leads to interesting results, e.g. a topological Hall effect [10, 11] or a skyrmion-flow Hall effect [12] in the metallic B20 compounds. As a motivation for these effects, see figure 1.3. More interestingly for possible later applications,

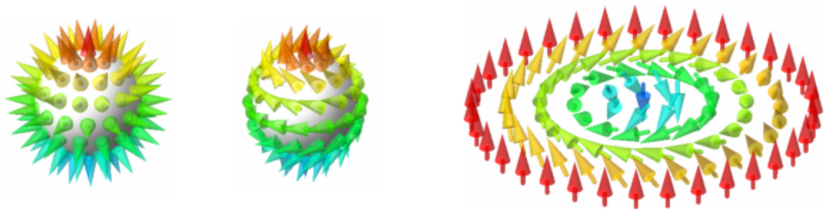

Figure 1.1: Building a chiral skyrmion texture. Original figure taken from [9].

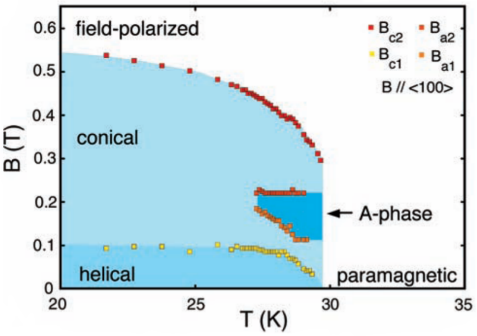

Figure 1.2: Phasediagram of MnSi. Skyrmion phase is 'A-phase'. Figure taken from [3].

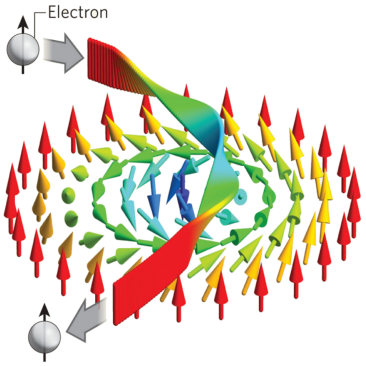

Figure 1.3: Electron follows the skyrmionic structure adiabatically. Figure taken from [17].

the winding number causes a very strong Magnus force acting on the spins [13–16]. As the Dzyaloshinskii-Moriya interaction results from spin-orbit interaction and hence is weak compared to the ferromagnetic coupling, the skyrmion texture is large compared to the underlying crystalline structure and thus very smooth. These very smooth skyrmion textures, supported by the strong Magnus force, can be moved at ultra-low threshold currents [14, 18–21]. Recently skyrmions could also be controlled written and deleted [22]. This is why magnetic skyrmions are a promising candidate for future spintronic applications [23, 24].
In this thesis we focus on single skyrmions in a ferromagnetic background, meaning at a magnetic field above the skyrmion phase in two dimensions. Their stability, espacially at very low temperatures, allows us to analytically and numerically study their behaviour in the presence of vacancies, that is unoccupied or empty sites in the crystalline lattice structure.

1.2. The Landau-Lifshitz-Gilbert Equation

The Landau-Lifshitz-Gilbert equation is the equation of motion for the direction of the local position- and time-dependent magnetization $\hat{\mathbf{M}}(\mathbf{r},t) \equiv \hat{\mathbf{M}} = \mathbf{M}/|\mathbf{M}|$ [25–27]

$$(\partial_t + \mathbf{j}\cdot\nabla)\,\hat{\mathbf{M}} = -\hat{\mathbf{M}}\times\mathbf{B}_{\text{eff}} + \alpha\hat{\mathbf{M}}\times\left(\partial_t + \frac{\beta}{\alpha}\mathbf{j}\cdot\nabla\right)\hat{\mathbf{M}}. \tag{1.3}$$

Here the new quantities which enter this equation are:

- the *effective magnetic field* $\mathbf{B}_{\text{eff}} \equiv -\frac{\delta F}{\delta \mathbf{M}}$
- the *damping parameters* α and β, which in general are small compared to 1 and not equal
- the *current density* $\mathbf{j}$.

As the free energy F of the chiral magnet is, as stated in the previous section, the free energy of a usual ferromagnet with an additional DMI term, see equation 1.1, the free energy F and hence the effective magnetic field $\mathbf{B}_{\text{eff}}$ is of the form:

$$F[\mathbf{M}] = \int \mathrm{d}^2 r \left[\frac{J}{2}\left[\nabla\mathbf{M}(\mathbf{r})\right]^2 + D\,\mathbf{M}(\mathbf{r})\cdot\left[\nabla\times\mathbf{M}(\mathbf{r})\right] - \mathbf{B}\cdot\mathbf{M}(\mathbf{r})\right] \tag{1.4}$$

$$\mathbf{B}_{\text{eff}} = J\Delta\mathbf{M}(\mathbf{r}) - 2D\,\nabla\times\mathbf{M}(\mathbf{r}) + \mathbf{B} \tag{1.5}$$

with J the ferromagnetic coupling constant, D the Dzyaloshinskii-Moriya interaction constant and $\mathbf{B}$ the external magnetic field. Furthermore it is already assumed that we consider the system to be at low temperatures, such that the local magnetization can only vary in direction but not in the absolute value. The standard Landau terms for the temperature dependent absolute value therefore are already omitted. The Landau-Lifshitz-Gilbert equation (LLG) is most commonly derived from phenomenological considerations by including the lowest order derivatives only. An example for a comprehensive derivation can be found in [28].

1.3. The Thiele Equation

To describe the movement of a skyrmion lattice the LLG equation 1.3 is not useful: it contains too many details, representing an equation of motion for the whole space-dependent magnetization in the system. Therefore we can use an ansatz provided by A. A. Thiele [29], where the LLG equation is projected down onto its translational modes. Basic requirements for this ansatz to work, besides breaking the translational symmetry which a skyrmion lattice obviously fulfills, are that the skyrmions are rigid objects and drift with a constant velocity. Both of these last requirements will be violated when later in this thesis considering the movement of a single skyrmion in a ferromagnetic background while interacting with vacancies. However, we just assume that we can take the same result as for the lattice to describe the movement of a single skyrmion. After calculating the projection suggested by Thiele one recovers the Thiele equation [15, 16, 28–30]

$$\mathbf{F}(\mathbf{r}) = \mathbf{G} \times (\dot{\mathbf{r}} - \mathbf{j}) + D\,(\alpha\dot{\mathbf{r}} - \beta\mathbf{j}) \tag{1.6}$$

where the velocity of the skyrmion $\dot{\mathbf{r}}$ is related to forces $\mathbf{F}(\mathbf{r})$, e.g. pinning forces, by the current density $\mathbf{j}$ via the damping parameters from the LLG equation 1.3 and the constants $\mathbf{G}$ and D. The constant vector $\mathbf{G}$ is called the *gyrocoupling vector* and it is quantized by the winding number $\mathcal{W}$ with

$$\mathbf{G} = \mathcal{G}\mathbf{n}, \quad \text{with } \mathcal{G} = 4\pi M\mathcal{W} \tag{1.7}$$

with $\mathbf{n}$ the unit vector in the direction of the external magnetic field $\mathbf{B}$ and M the absolute magnetization which in the following is always fixed to $M = 1$. The constant D is the *dissipative constant*, which results from an originally 3×3 matrix that turns out to be almost diagonal in the considered setup. This constant has been calculated for a single skyrmion and approximately it is $D \approx 15$ [31].
In the case of a pure system without any pinning forces, the dependency of the skyrmion velocity relative to the current density becomes [19]

$$v_{\parallel} = \left(\frac{\beta}{\alpha} + \frac{\alpha - \beta}{\alpha^3\left(\frac{D}{\mathcal{G}}\right)^2 + \alpha}\right) j \tag{1.8}$$

$$v_{\perp} = \frac{(\alpha - \beta)\left(\frac{D}{\mathcal{G}}\right)}{\alpha^2\left(\frac{D}{\mathcal{G}}\right)^2 + 1}\, j \tag{1.9}$$

where $v_{\parallel}$ and $v_{\perp}$ are the components of the velocity parallel and perpendicular to the current density $\mathbf{j}$.
For theoretical considerations, the general choice $\alpha \neq \beta$ is valid but only makes the analysis more difficult. Hence we use that we can extract all parts of the Thiele equation which are dependent on the current density or the damping β. We now introduce a new current density

$\mathbf{j}_\alpha$, which couples to the Thiele equation with a different damping $\alpha \neq \beta$ but has the same effect in the equation, that is

$$\begin{aligned}(\mathbf{G}\times+\beta D)\,\mathbf{j}_\beta &\stackrel{!}{=}(\mathbf{G}\times+\alpha D)\,\mathbf{j}_\alpha\\ \begin{pmatrix}\beta D & -\mathcal{G}\\ \mathcal{G} & \beta D\end{pmatrix}\mathbf{j}_\beta &\stackrel{!}{=}\begin{pmatrix}\alpha D & -\mathcal{G}\\ \mathcal{G} & \alpha D\end{pmatrix}\mathbf{j}_\alpha.\end{aligned} \tag{1.10}$$

Hence due to $\det(\mathbf{G}\times+\beta D)=\beta^2D^2+\mathcal{G}^2\geq\mathcal{G}^2>0$ this equation is always invertible. This means that we can always transform the current density according to 1.10 in such a way, that the damping β effectively is replaced by a damping α or vice versa. Using this transformation the Thiele equation can be written in a simplified form

$$\mathbf{F}(\mathbf{r})=\mathbf{G}\times(\dot{\mathbf{r}}-\mathbf{j})+\mathcal{D}\,(\dot{\mathbf{r}}-\mathbf{j}) \tag{1.11}$$

with the dissipative constant $\mathcal{D}(\alpha)=D\alpha$ including the remaining damping parameter. From this representation of the Thiele equation one can immediately read off that in the absence of other forces than the current density, the skyrmion moves with a velocity equal in direction and absolute value to the transformed current density. Note that this equation only holds in the Thiele approximation with the requirements stated above.

1.4. The System of Units

In the free energy functional we find, that the term for the ferromagnetic coupling by itself is already scale invariant: after a rescaling, the integration over the two-dimensional plane cancels the squared derivative of the magnetization. Hence it is reasonable to decide to express the unit of energy in terms of the ferromagnetic coupling J. The equation for the dimensionless free energy can then be obtained from equation 1.4 by dividing both sides of the equation by J.

This very basic decision in the numerical units also fixes the units of D and B to be equal to J. Furthermore then the unit of the effective magnetic field is also fixed to be J and via the LLG equation 1.3 then also the current density is fixed to units of J. From the derivative with respect to time, which has units $^1/_{\text{time}}$, then also the unit of time is fixed to $^1/_J$.

Going over from the numerical units where length is fixed by the lattice constant a to the units of the continuum model for the magnetization, there is no explicit length anymore. The characteristic lengthscale of the system is rather determined by the interplay of the different interaction constants of the free energy. Here we can again use a scaling transformation to find that one possibility to form a length is

$$R=\frac{D}{B}\,a \tag{1.12}$$

which we identify with the radius of the skyrmion. This way we have a connection between the lattice constant a and the unit for length R in the continuum model. Further we can form a third quantity

$$\zeta=\frac{JB}{D^2} \tag{1.13}$$

which is dimensionless. Its value affects the shape of the skyrmion in the rescaled system of units.

At a later point in this thesis, the potential of a point-like vacancy will be determined to obey a scaling law with respect to the size of the skyrmion, see section 2.4.4. The scaling which turns out is the same as expected from the a scaling transformation of a delta-potential. For a given shape ζ of the skyrmion and a hole radius $a_\mathrm{H} = r_\mathrm{H} a$, in numerical units the characteristic potential which obeys the same scaling as the potential function in numerical units hence is given as

$$V_0 = \text{energy}\,\frac{\text{area hole}}{\text{area SkX}} = J\,\frac{a_\mathrm{H}^2}{R^2} = J\left(\frac{B}{D}\right)^2 r_\mathrm{H}^2. \tag{1.14}$$

However, in the following in this thesis when considering point-like vacancies we will always use $r_\mathrm{H} = 1$.
A last unit that is needed is the unit for the current density. Hence we introduce a characteristic current density j_0 by the use of the Thiele equation 1.11. Here the force, which is the spatial derivative of the potential, in terms of units is equal to the velocity and the current density. Basically this happens because in the theoretical description we have $\hbar = c = 1$. Hence the characteristic current density is the potential devided by the most natural length scale which here must be the skyrmion radius R:

$$j_0 \approx \partial_r V(r) \approx \frac{V_0}{R} = J\left(\frac{B}{D}\right)^3 a\, r_\mathrm{H}^2. \tag{1.15}$$

With these units we can describe every relevant quantity in the continuum model.

2. Pinning a Skyrmion by a Vacancy in Two Dimensions

As skyrmions are a good candidate for spintronics due to their stability, one seeks to find a possibility to control them to a sufficient extent. The interaction of skyrmions with any kind of disorder in the underlying cristaline lattice therefore needs to be studied. A central question one needs to ask is whether or to which extent disorder prevents us from controlling skyrmions or how we could maybe even use it for our purposes. As skyrmions are topological objects build from magnetic spin structures, disorder may arise as magnetic and non-magnetic impurities. Magnetic impurities are identified with atoms in the crystaline lattice where at a given site the spin coupling is changed such that the spin points in a particular direction. Completely unoccupied lattice sites, so-called vacancies, are non-magnetic impurities and will certainly also influence a skyrmion closeby as they put a constraint on the local spin structure. Whereas magnetic impurities have already been studied by various research groups [16, 19] qualitatively, the influence of vacancies on skyrmions is not known. Furthermore vacancies shall be considered as they are the more natural type of disorder within a lattice.

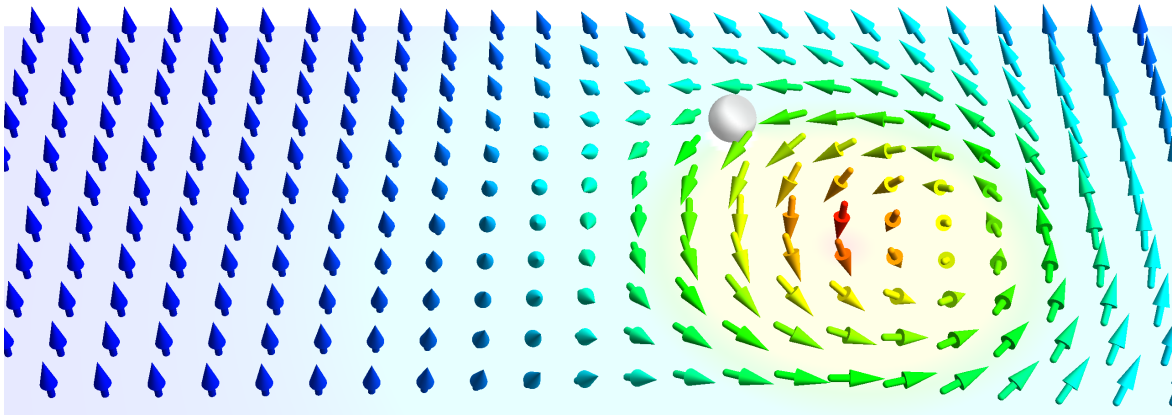

Figure 2.4: Skyrmion pinned by a vacancy (site marked with the white sphere). Result obtained from simulating the full micromagnetic system, see chapter 2.1.

2.1. Simulating the Full Micromagnetic System

As a first step towards the answer to the question how a skyrmion interacts with a vacancy we simulate the whole micromagnetic system in a way proposed by C. Schütte. For the simulation, we discretize the continuous function for the magnetization $\mathbf{M}(\mathbf{r})$. On each site of the lattice the magnetic moment is given by a three dimensional Heisenberg spin $\mathbf{M}(\mathbf{r})$, meaning all spins have equal length. Demagnatization effects may be neglected as all calculations are assumed at zero temperature. By convention we set the absolute value of the local magnetization to one, $\|\mathbf{M}(\mathbf{r})\| = 1$. The equation which describes the time evolution of the system by the precession of each magnetic moment is the Landau-Lifshitz-Gilbert (LLG) equation 1.3. It also conserves the absolute value of each magnetic moment and hence fits the assumption of Heisenberg spins. To calculate the solution of the LLG by iteration it is useful to rewrite the equation such that the linear derivative with respect to time is isolated on the left hand side. A priori, this condition is violated as the dependence on the derivative is more complicated but it can be resolved easily. One can check that for any pair of perpendicular vectors $\mathbf{a}$ and $\mathbf{b}$ the following

relation holds true:

$$\mathbf{a} \times \mathbf{a} \times \mathbf{b} = -\|\mathbf{a}\|^2 \mathbf{b} \tag{2.16}$$

Using that the LLG conserves the absolute value of each magnetic moment $\mathbf{M}$, any change $\mathbf{dM}$ can only be perpendicular to the initial direction of $\mathbf{M}$. Thus equation 2.16 also holds for $\mathbf{a} = \mathbf{M}$ and $\mathbf{b} = \mathbf{dM}$. After isolating the derivative with respect to time in the LLG 1.3 and iteratively plug it back into the equation, one can bring the gradient dependent part from the left hand side of the LLG equation 1.3 to the right and iteratively insert it into the derivative with respect to time on the right hand side again. Using equation 2.16 with our conventionally chosen $\|\mathbf{M}\| = 1$ yields:

$$\begin{aligned}
\partial_\mathrm{t}\mathbf{M} &= -\mathbf{M} \times \mathbf{B}_\mathrm{eff} - (\mathbf{j} \cdot \nabla)\,\mathbf{M} + \alpha \mathbf{M} \times \left[\partial_\mathrm{t}\mathbf{M} + \frac{\beta}{\alpha}(\mathbf{j} \cdot \nabla)\,\mathbf{M}\right] \\
&= -\mathbf{M} \times \mathbf{B}_\mathrm{eff} - (\mathbf{j} \cdot \nabla)\,\mathbf{M} + \beta \mathbf{M} \times [(\mathbf{j} \cdot \nabla)\,\mathbf{M}] \\
&\quad + \alpha \mathbf{M} \times (-\mathbf{M} \times \mathbf{B}_\mathrm{eff} - (\mathbf{j} \cdot \nabla)\,\mathbf{M} + \beta \mathbf{M} \times [(\mathbf{j} \cdot \nabla)\,\mathbf{M}]) \\
&\quad + \alpha^2 \mathbf{M} \times \mathbf{M} \times \partial_\mathrm{t}\mathbf{M} \\
&= -[\mathbf{M} \times + \alpha \mathbf{M} \times \mathbf{M} \times]\,\mathbf{B}_\mathrm{eff} \\
&\quad + [-1 + (\beta - \alpha)\,\mathbf{M} \times + \alpha\beta \mathbf{M} \times \mathbf{M} \times]\,(\mathbf{j} \cdot \nabla)\,\mathbf{M} \\
&\quad - \alpha^2 \partial_\mathrm{t}\mathbf{M}
\end{aligned} \tag{2.17}$$

from which we recover an equation linear in the time dependent derivative:

$$\partial_\mathrm{t}\mathbf{M} = \frac{1}{1+\alpha^2}\left(-[\mathbf{M} \times + \alpha \mathbf{M} \times \mathbf{M} \times]\,\mathbf{B}_\mathrm{eff} + [-1 + (\beta - \alpha)\,\mathbf{M} \times + \alpha\beta \mathbf{M} \times \mathbf{M} \times]\,(\mathbf{j} \cdot \nabla)\,\mathbf{M}\right) \tag{2.18}$$

Here $\mathbf{B}_\mathrm{eff}$ plays the role of an effective magnetic field and is defined as in equation 1.5. Concerning the discretization for the numerics we choose to discretize the continuous magnetization onto a two-dimensional square lattice. The derivatives in the following are replaced by the symmetric differential ratios:

$$\begin{aligned}
\partial_\mathrm{x}\mathbf{M}(\mathbf{r}) &\to \frac{1}{2a}(\mathbf{M}_{\mathrm{i+1,j}} - \mathbf{M}_{\mathrm{i\text{-}1,j}}) \\
\partial_\mathrm{y}\mathbf{M}(\mathbf{r}) &\to \frac{1}{2a}(\mathbf{M}_{\mathrm{i,j+1}} - \mathbf{M}_{\mathrm{i,j\text{-}1}}) \\
\Delta\mathbf{M}(\mathbf{r}) &\to \frac{1}{a^2}(\mathbf{M}_{\mathrm{i+1,j+1}} + \mathbf{M}_{\mathrm{i+1,j\text{-}1}} + \mathbf{M}_{\mathrm{i\text{-}1,j+1}} + \mathbf{M}_{\mathrm{i\text{-}1,j\text{-}1}} - 4\mathbf{M}_{\mathrm{i,j}})
\end{aligned} \tag{2.19}$$

With these replacements the initial configuration can now be iterated. The algorithm chosen for iterating the differential equation is the Runge-Kutta integration method of third order in the case of a finite current density and fourth order for zero current density.
We want to use this algorithm to iteratively solve the time evolution of the full micromagnetic system consisting of a skyrmion in a ferromagnetic background. Hence the initial setup is constructed by taking a whole ferromagnetic configuration and placing a skyrmion inside. Note that the exact size and winding shape of the skyrmion is not important. What is important is the correct winding number. We then run the iteration of the LLG equation without any current and with a sufficiently large damping at zero temperature. The system will then equilibrate to

the optimal configuration for the chosen set of parameters. If we choose the range of parameters which is of our interest the winding number is conserved. Next, the vacancy is created. The vacancy is supposed to model a hole in the layer, hence we remove the spin at this particular site setting it to zero. Finally, the differential LLG equation is iterated at a finite current density j. By plotting the magnetic configurations after fixed time intervals we recover a movie of the driven skyrmion. Parts of the resulting movement are shown in figure 2.5. From these results one can see that first there is a repulsive interaction between skyrmion and vacancy as the skyrmion drifts down, away from the vacancy. Afterwards, the skyrmion changes its way being attracted by the vacancy, then is again driven by the current density to the right and finally stays pinned at the bottom-right side of the vacancy.

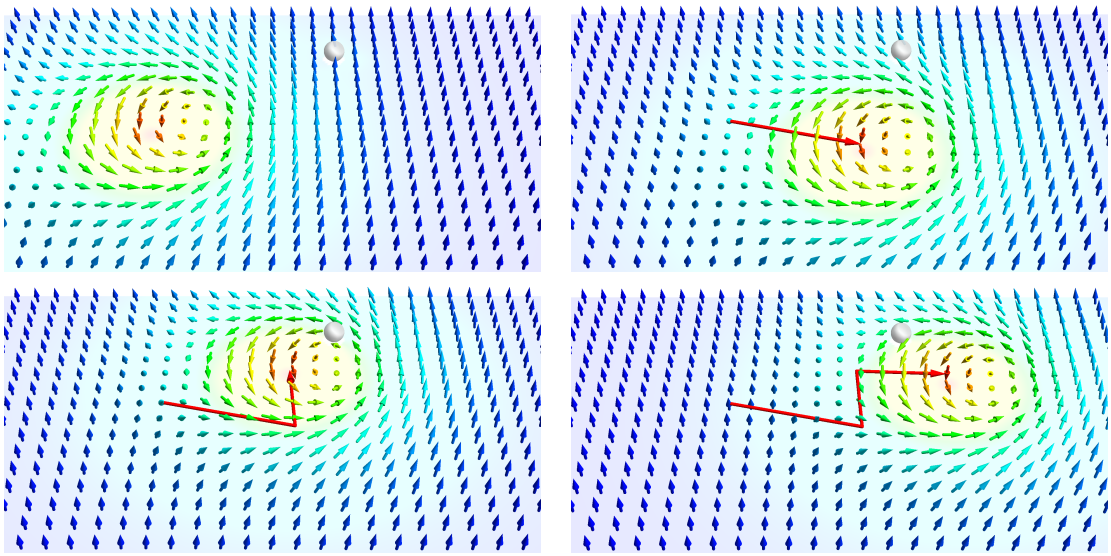

Figure 2.5: Single skyrmion moving (follow arrows) driven by a current density j to the right under the influence of a vacancy (sphere). Results obtained from simulating the full micromagnetic system as described in sec. 2.1 with $D = 0.3J$, $B = 0.09J$, $\alpha = \beta = 0.4$, $j = 0.001J$. The shown configurations are at times $t = 7500/J$, $t = 10500/J$ and $t = \infty$ relative to the initial configuration.

This is only one single trajectory starting from one particular point in the two-dimensional plane. To be able to compare more trajectories and in a more quantitative way we use a tracking algorithm. It calculates the center of the skyrmion from the spins that point opposite to the ferromagnetic background and returns the skyrmion's path. A comparison of resulting trajectories is shown in figure 2.6.
Analyzing the trajectories we find that all of them either flow to infinity or end in the fixed point as does the skyrmion in figure 2.5. Up to here, there seems to be only one stable fixed point in the potential of the vacancy. However, simulating the whole micromagnetic system takes a long time. In the following, an analytic approach will be applied offering a more detailed look into the system.

2.2. The Thiele Ansatz - Qualitative Considerations

The LLG equation describes the movement of every magnetic moment in the system. As we do not want to describe every spin but the movement of the skyrmion, which is a collective

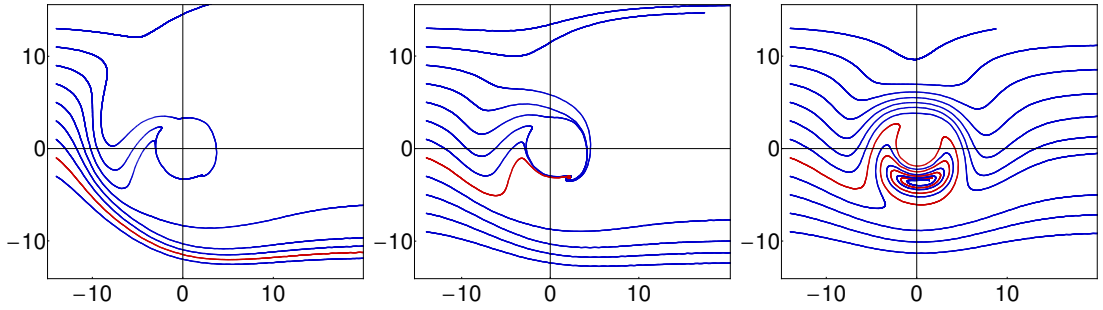

Figure 2.6: Trajectories of a single skyrmion driven by a current density j influenced by a single-site vacancy in the center. Results obtained from simulating the full micromagnetic system as described in sec. 2.1 with $D = 0.3J$, $B = 0.09J$ and $\alpha = \beta = 0.4$, $j = 0.0005J$ (left), $\alpha = \beta = 0.4$, $j = 0.001J$ (center) and $\alpha = \beta = 0.04$, $j = 0.001J$ (right). The trajectories start on the left and end in the fixed point or at infinity. The red trajectory in each figure corresponds to the starting point of the skyrmion shown in figure 2.5.

movement of spins, we apply the Thiele method, see section 1.3. Certainly, Thiele's request to have a solid and rigid skyrmion will be violated but can be included in the potential function of the vacancy. Further, the interaction with the vacancy might also excite internal modes. Later we will see in the direct comparison to the LLG solution how accurate of this ansatz is though. According to section 1.3 the Thiele equation reads

$$\mathbf{F}(\mathbf{r}) = \mathbf{G} \times (\dot{\mathbf{r}} - \mathbf{j}) + \mathcal{D}\,(\dot{\mathbf{r}} - \mathbf{j}) \tag{2.20}$$

with $\mathbf{j}$ the driving current density and the damping constants $\alpha = \beta$ which are linear included in $\mathcal{D}$. The vector $\mathbf{G}$, called gyrocoupling vector, is given by

$$\mathbf{G}_\mathrm{i} = \epsilon_\mathrm{ijk} \int_\mathrm{UC} \mathrm{d}^2 r\ \frac{1}{2}\mathbf{M} \cdot (\partial_\mathrm{j}\mathbf{M} \times \partial_\mathrm{k}\mathbf{M}) \tag{2.21}$$

already included that we have decided for $\|\mathbf{M}\| = 1$. As this expression up to a prefactor is the one which defines the topological winding number, in the case of a single skyrmion one can immediately write down the resulting expression for the gyrocoupling vector $\mathbf{G}$:

$$\mathbf{G} = \mathcal{G}\mathbf{n}, \quad \text{with } \mathcal{G} = 4\pi\mathcal{W}. \tag{2.22}$$

Here $\mathbf{n}$ is the unit vector parallel to the magnetic field and hence perpendicular to the plane. The topological winding number is $\mathcal{W} = -1$ as we use a positive Dzyaloshinskii-Moriya coupling constant and skyrmions which are only winded once. The prefactor for the dissipative force term $\mathcal{D}$ was calculated numerically for a rigid skyrmion. However, we assume the deformation in our setup to be sufficiently small and for $\alpha = \beta = 0.4$, which is a rather large damping, one recovers $\mathcal{D} \approx 6$ [31]. Additionally, in most numerical calculations also the small damping $\alpha = \beta = 0.04$ is shown for comparison.
Now Thiele's method has produced an explicit differential equation of first order which can be simplified when combining $\mathbf{G}$ and $\mathcal{D}$ into a single matrix $\mathcal{A}$:

$$\mathbf{F}(\mathbf{r}) = \mathcal{A}\,(\dot{\mathbf{r}} - \mathbf{j}) \tag{2.23}$$

with

$$\mathcal{A} = \begin{pmatrix} \mathcal{D} & -\mathcal{G} \\ \mathcal{G} & \mathcal{D} \end{pmatrix}. \tag{2.24}$$

This matrix $\mathcal{A}$ is orthogonal up to a prefactor $\gamma = |\det(\mathcal{A})|^{\frac{1}{2}} = \left(D^2 + \mathcal{G}^2\right)^{\frac{1}{2}} > 0$.
Note that the undisturbed skyrmion obeys a rotation symmetry with respect to the center. Hence the potential energy caused by the vacancy should only depend on the distance and we recover

$$\mathbf{F}(\mathbf{r}) = -\nabla V(\mathbf{r}) = -V'(r)\,\mathbf{e}_\mathrm{r}. \tag{2.25}$$

The potential function is not known and cannot be calculated analytically but numerical approaches are discussed in section 2.4. When knowing the function it is useful to rewrite the simplified Thiele equation 2.23 in the following form:

$$\begin{aligned}\dot{\mathbf{r}} &= \mathcal{A}^{-1}\mathbf{F}(\mathbf{r}) + \mathbf{j} \\ &= -V'(r)\mathcal{A}^{-1}\mathbf{e}_\mathrm{r} + \mathbf{j} \\ &= -\frac{1}{\gamma^2}V'(r)(\mathcal{D}\mathbf{e}_\mathrm{r} - \mathcal{G}\mathbf{e}_\phi) + \mathbf{j}.\end{aligned} \tag{2.26}$$

Without knowing the exact form of the potential we can now extract some information from this simplified Thiele equation: when there is no force from the vacancy influencing the skyrmion, $V'(r) = 0$, it moves straight into the direction of the current. This is what we wanted to achieve with our overall choice of equal damping parameters $\alpha = \beta$.
Concerning the force generated by the vacancy $\mathbf{F}(\mathbf{r})$ it points either away or towards the vacancy, dependent on the sign. To get the velocity resulting from this force we need to multiply it with the almost orthogonal matrix $\mathcal{A}^{-1}$. The orthogonal part of $\mathcal{A}^{-1}$ just rotates the vectorfield slightly which gives the direction of the force. The angle by which the force field is turned depends on the ratio of $\mathcal{G}/\mathcal{D}$ as becomes obvious when rewriting the product in cylindrical unit vectors. The prefactor γ only rescales the derivative of the potential.
With this decomposition of the force into the radial and the angular part we can already understand qualitatively the movement of the skyrmion: In those regions where the potential is repulsive the radial part of the force needs to have a positive prefactor, thus $V'(r) < 0$. On the other hand this means for the angular part of the force that the total prefactor is also positive as $\mathcal{G} < 0$. Repulsion therefore always comes with a rotation around the vacancy in the mathematical positive sense. The opposite is true for attractive regions of the force where the angular movement is against the mathematical positive sense. These considerations fit to the trajectories shown in figure 2.6.

2.3. Analysis of Thiele's Fixed Points

The simplified Thiele equation 2.26 still is not solvable, especially as the force is not known. We will in section gain some more insight into the dynamics of the equation by analyzing the fixed points of the equation.
So far the force part generated by the vacancy is invariant under rotation. This symmetry needs to be broken by the current density. In general it can be chosen into an arbitrary direction and also can be assumed to be constant [33]. In the simulation of the full micromagnetic system the current density was chosen to point in the positive x-direction. Hence this is also the choice for the further analysis.

$$\mathbf{j} = j\mathbf{e}_\mathrm{x} \tag{2.27}$$

with $j > 0$.

Now we want to study the fixed points of the Thiele equation. The condition to have a fixed point is to have a place where the skyrmion is at rest

$$\dot{\mathbf{r}}_{\mathrm{FP}} = 0. \tag{2.28}$$

With the use of this condition and the assumption for the current density 2.27 one recovers from the simpified Thiele equation 2.26:

$$V'(r_{\mathrm{FP}})\,\mathbf{e}_{\mathrm{r}} = j\mathcal{A}\,\mathbf{e}_{\mathrm{x}}. \tag{2.29}$$

This equation can only have solutions on the axis given by the direction of the unit vector $\mathbf{e}_{\mathrm{x}}$ turned by the matrix $\mathcal{A}$ on the right hand side:

$$\tan(\varphi_{\mathrm{FP}}) = \frac{\mathcal{G}}{\mathcal{D}} \tag{2.30}$$

with in our case $\mathcal{G} < 0$ and $\mathcal{D} > 0$. For these choices of parameters we find that for $V'(r) < 0$ the solutions have to be in the interval $\varphi_{\mathrm{FP}} \in \left(\frac{1}{2}\pi, \pi\right)$. On the contrary, for $V'(r) > 0$ the solutions have to be in the quarter $\varphi_{\mathrm{FP}} \in \left(\frac{3}{2}\pi, 2\pi\right)$. Due to the rotation invariance of the vacancy force this angle is the same for all possible directions of $\mathbf{j}$.
The second constraint on solutions is that the absolute value of both sides of the equation 2.29 have to be identical:

$$|V'(r_{\mathrm{FP}})| = j\gamma. \tag{2.31}$$

where we use $\gamma = \left(D^2 + \mathcal{G}^2\right)^{\frac{1}{2}}$ as in the previous section. One could try to solve this equation for the distance r_{FP} if the potential $V(r)$ was known. A numerical approach to the determination of $V(r)$ is presented in section 2.4.
Now we know in principle the position of the fixed points as we know the angular and radial coordinate.
The next question is which of the fixed points are stable, unstable or saddle points with one stable and one unstable direction. In analogy to the discussion of renormalization flows this is done by linearizing the differential equation 2.26 around an arbitrary but given fixed point. In this equation the only non-linear part is the vacancy force on the right hand side which can be linearized by calculating the Taylor series around the fixed point up to including the first order:

$$\begin{aligned} \mathbf{F}(\mathbf{r}) &\approx -V'(r)\,\mathbf{e}_{\mathrm{r}}|_{r=r_{\mathrm{FP}}} + \mathcal{B}\,(\mathbf{r} - \mathbf{r}_{\mathrm{FP}}) \\ &\overset{2.29}{=} -\mathcal{A}\,\mathbf{j} + \mathcal{B}\,(\mathbf{r} - \mathbf{r}_{\mathrm{FP}}) \end{aligned} \tag{2.32}$$

After shifting the position $\mathbf{r} \to \mathbf{r} + \mathbf{r}_{\mathrm{FP}}$ one recovers the linearized differential equation around a given fixed point:

$$\dot{\mathbf{r}} = \mathcal{C}\mathbf{r} \tag{2.33}$$

with $\mathcal{C} = \mathcal{A}^{-1}\mathcal{B}$ and $\mathcal{B}$ a matrix from the linearization of the force. A more detailed derivation is given in the appendix A.1.
However, the finally recovered matrix $\mathcal{C}$ determines the stability of fixed points. Dependent on the sign of its eigenvalues λ_i, $i = 1, 2$, the fixed point is

$$\begin{aligned} \text{stable, definite} &\Leftrightarrow \lambda_{1,2} < 0 \\ \text{unstable, definite} &\Leftrightarrow \lambda_{1,2} > 0 \\ \text{semidefinite} &\Leftrightarrow \lambda_1 < 0 < \lambda_2\ . \end{aligned} \tag{2.34}$$

This can easily be understood in the one-dimensional case: The differential equation $\dot{x} = \lambda x$ obviously converges for $\lambda < 0$ and diverges for the opposite case. The connection to the higher dimensional differential equation can be made by diagonalizing the matrix $\mathcal{C}$. Then the equations in the eigenvector basis are decoupled to one dimensional equations for which the relation above holds. Calculation of the eigenvalues and usage of the statements 2.34 yields the following results:

$$\begin{aligned} \operatorname{sgn}(V'(r_{\mathrm{FP}}))\operatorname{sgn}(V''(r_{\mathrm{FP}})) \gtrless 0 \quad & {}^{\text{definite}}/_{\text{semidefinite}} \\ \operatorname{sgn}(V'(r_{\mathrm{FP}})) \gtrless 0 \quad & {}^{\text{stable}}/_{\text{unstable}}. \end{aligned} \tag{2.35}$$

Again, the derivation of these statements can be found in the appendix A.1.
Now that the stability of possible fixed points is known, consider e.g. a stable fixed point. Consequently, the sign of $V'(r_{\mathrm{FP}})$ has to be positive. This would correspond to the fixed point where the captured skyrmions in the simulations 2.6 end. Combining this result with what we found after equation 2.30 we conclude that every stable fixed point has to be on the half-axis in the lower-right quadrant or, as denoted above, in the range $\varphi_{\mathrm{FP}} \in \left(\frac{3}{2}\pi, 2\pi\right)$. This result holds for any value of the current density j. Consequently stable fixed points do not turn into other types of fixed points when tuning the current. Using what we have found in equation 2.31 we can now deduce that the maximal current for having a stable fixed point, meaning for having a pinned skyrmion, is

$$j_{\max} = \frac{1}{\gamma} \max_r \{V'(r)\}. \tag{2.36}$$

Repeating the argument for unstable definite fixed points yields the opposite result: A completely unstable fixed point can only exist in the upper-left quadrant meaning in the range $\varphi_{\mathrm{FP}} \in \left(\frac{1}{2}\pi, \pi\right)$. The point then exists until a maximal current is reached, in analogy to equation 2.36 with $V'(r) \to -V'(r)$.
Also the eigenvectors of $\mathcal{C}$ can be calculated. The exact expression can be found in the appendix A.1, equation A.102.

2.4. The Effective Vacancy Potential

The aim of this section is to determine the potential of a single vacancy acting on a single skyrmion. In continuum, this potential could be obtained from considering the Ginzburg-Landau free energy functional, see equation 1.4:

$$F[\mathbf{M}] = \int \mathrm{d}^2 r \left[\frac{J}{2} \left[\nabla \mathbf{M}(\mathbf{r})\right]^2 + D\mathbf{M}(\mathbf{r}) \cdot \left[\nabla \times \mathbf{M}(\mathbf{r})\right] - \mathbf{B} \cdot \mathbf{M}(\mathbf{r}) \right] \tag{2.37}$$

for Heisenberg spins $\|\mathbf{M}(\mathbf{r})\| = 1$ and certain constraints. The presence of a single skyrmion implies the constraint that the winding number of the whole system has to be $\mathcal{W} = \pm 1$. The location $\mathbf{R}$ of the skyrmion we define as the position of the magnetic moment pointing opposite to the otherwise ferromagnetic background. As the constraint for having a vacant site or region we need to set the magnetization $\mathbf{M}$ at this site or region to zero.
If we were able to find the minimum configuration for $\mathbf{M}(\mathbf{r})$ under these constraints for any distance $\mathbf{R}$ between skyrmion and vacant site, we had solved the problem. Unfortunately, even the problem of the single skyrmion in a ferromagnetic background was not yet solved exactly. Thus it seems reasonable to assume that also this problem, imposing a further constraint, can only be solved approximately or numerically.

2.4.1. The Lowest Order Approximation

The lowest order approximation to the potential of a vacancy we recover when assuming that the vacancy has no influence on the neighboring sites. Hence what determines the potential is the energy contribution of the single magnetic moment or the region where the vacancy is located.
Let $\mathcal{A}(\mathbf{r})$ be the vacant region around $\mathbf{r}$ or the vacant moment at $\mathbf{r}$. Then the energy contribution by this region or site and hence the potential $V(\mathbf{r})$ is given by

$$V(\mathbf{r}) = \int_{\mathcal{A}(\mathbf{r})} \mathrm{d}^2 r' \left[\frac{J}{2} \left[\nabla \mathbf{M}_0(\mathbf{r}')\right]^2 + D\mathbf{M}_0(\mathbf{r}') \cdot \left[\nabla \times \mathbf{M}_0(\mathbf{r}')\right] - \mathbf{B} \cdot \mathbf{M}_0(\mathbf{r}') \right] \tag{2.38}$$

where $\mathbf{M}_0(\mathbf{r}')$ is the solution of the single skyrmion in a ferromagnetic background.
As the single skyrmion solution is not known analytically it has to be derived numerically. For this purpose, as in section 2.1, we construct a square lattice with Heisenberg spins and discretize the differential operators as in equation 2.19. Afterwards we prepare a single skyrmion configuration in a polarized background and let the system relax by iterating the Landau-Lifshitz-Gilbert (LLG) equations of motion 1.3. When the system has equilibrated we calculate at every site of the lattice the energy contribution and the distance of the site to the center of the skyrmion. This procedure yields a list of data points which connect the distance of the skyrmion to the energy contribution of the site. As the skyrmion usually is created on a highly symmetric point this only leads to a couple of data points. By driving the skyrmion off this point with a current, using the LLG iteration, and tracking the center, we have access to many more data points. This trick can be used as the energy difference of a high-symmetry skyrmion to a displaced skyrmion is very small compared to the energy contribution of the site. According to what we stated in equation 2.38 this function is a first estimate to the potential of a vacancy.
We repeat this procedure for constant ferromagnetic couplings J and Dzyaloshinskii-Moriya couplings D and vary the magnetic field $\mathbf{B}$. This is how we determine the dependence of the potential on the ratio $\frac{D}{B}$, see also section 2.4.4. The results are shown in figure 2.7.
The results of this approach show that the potential has a unique local minimum for magnetic fields $\mathbf{B} > 0.06J$ which also is the global minimum. This minimum approaches the center of the skyrmion as the magnetic field increases. Additionally it gets deeper and, even more important, the gradient increases. This means the higher the magnetic field, the stronger is the pinning. For lower magnetic fields there also is a local minimum of the potential but the global minimum is at infinity. For all magnetic fields the potential saturates for larger distances. This is what should be expected as for large distances the vacancy is placed in an almost completely polarized region. Consequently in this region the potential depends linear on the magnetic field.
The position of the local minimum is not, as one might expect, in the center of the skyrmion. This would be the place for a vacancy favoured by the ferromagnetic coupling as well as for the Zeeman coupling. The Dzyaloshinskii-Moriya coupling, however, favours the vacancy to be at infinity. The resulting minimum hence is off the center and its exact position is determined by the competition between the different iteractions.
This lowest order approximation we considered up to now does not take into account that close to the vacant site the spins are free to reorder. In fact they prefer to twist around the vacancy which leads to significant corrections.

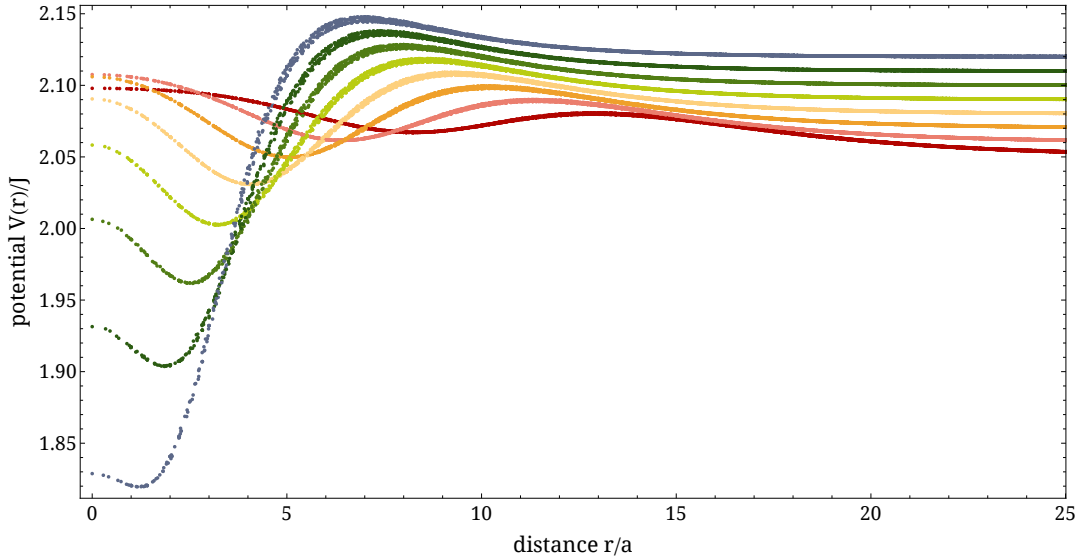

Figure 2.7: Potential $V(r)$ of a single vacancy acting on a single skyrmion as a function of distance r between the vacancy and the center of the skyrmion. Potential evaluated for parameters $D = 0.3J$ and $B = 0.05J$ (red) to $B = 0.12J$ (blue) in steps of $\Delta B = 0.01J$.

2.4.2. The Local Update Algorithm

In section 2.4.1 we found a way to calculate the potential of a single site vacancy acting on a single skyrmion to lowest order. In this approach we assumed that the vacancy does not influence the neighboring sites. This assumption is a very crude one as we will see in this section. Indeed the spins near the vacancy are strongly influenced by it. The idea of the local update algorithm is that we allow spins within a certain radius around the vacancy to reorder. Only after the reordering we calculate the energy contribution. This way the spin are able to react to the vacancy and reorder in the energetically most favourable configuration. We decide to only equilibrate a small part of the system near the vacancy because otherwise the whole system would go to the local minimum in the energy configuration. This would then result in a movement of the whole skyrmion, either to the fixed point or to infinity. But if we only let a small fraction of the spins reorder, the center of the skyrmion will not be moved as it is fixed by the surrounding spins. However, a priori it is neither clear for how many reordered spins the result converges nor whether there is convergence at all.

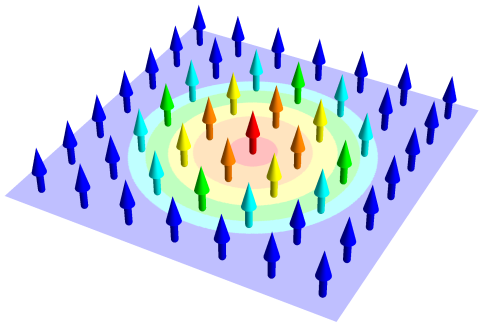

Figure 2.8: Square lattice of spins (blue arrows) with the different orders of the local update radius shown, centered around the vacancy (red arrow).

The area in which the spins are allowed to reorder we define by radia of certain orders. The order of the local update radius is equal to the order of neighboring as it is shown in figure 2.8. Order zero radius of equilibration corresponds to the radius coloured blue in the figure. In this case the only spin that is allowed to move is the one which is vacant, meaning there is no equilibration. The order zero case thus is equivalent to the lowest order approach, section 2.4.1.

Going one order higher to the first order radius, the first order neighbors (nearest neighbors) of the vacancy are allowed to reorder. For the order two radius all spins that according to the figure are included in the yellow circle, which are the next nearest neighbors, may reorder.
To check whether there is convergence, we choose a reasonable runtime for the local equilibration, $T = 100\,{}^{1}/_{J}$, and run the algorithm for orders up to order twelve and different ratios $\frac{D}{B}$. The resulting vacancy potentials are shown in figure 2.9. From the comparison in figure 2.9

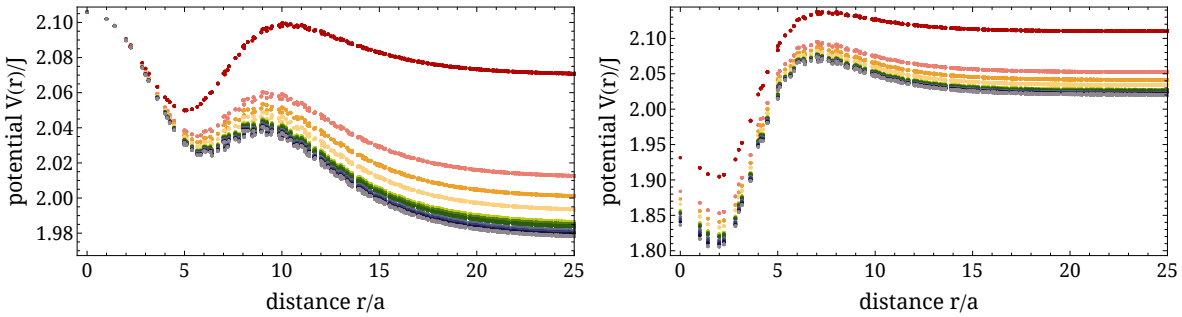

Figure 2.9: Results of the local update algorithm. Orders are chosen from zero (red) to eight (blue) and additionally ten (dark blue) and twelve (gray). Parameters: $D = 0.3J$, and $B = 0.07J$ (left), $B = 0.11J$ (right). Time for reordering is $T = 100\,{}^{1}/_{J}$.

one can see that already for the first order radius the change of the potential is massive. For the case of a smaller magnetic field $B = 0.07J$ the global minimum becomes local. For higher magnetic field, $B = 0.11J$, the whole potential only seems to be shifted by an offset. However, for all magnetic fields we see that the potential does not change significant anymore as soon as we have a large enough order of radius. As one can hardly distinguish any of the last curves although the last ones are plotted in steps of two orders of radius we can say that the algorithm has converged. The resulting potentials for the converged order twelve local update algorithm are shown in figure 2.10. In general, comparing these results to the ones from the previous lowest order approach, section 2.4.1, we find that the minimum at finite distance becomes more unstable. For magnetic fields $B < 0.07J$ the local minimum even disappears completely.
We already argued that for an infinte order of equilibration the method breaks down as the skyrmion moves. Therefore the question arises whether this convergent result does make sense at all. To confirm the validity of our results and the success of the local update algorithm we compare these results with the global update ansatz, see section 2.4.3.

2.4.3. The Global Update Algorithm

The local update algorithm, section 2.4.2, includes equilibration around the vacancy into the determination of the potential. In this section we show the stability of this ansatz and introduce a second method.
As we want to consider the reordering of the system due to the vacancy in the calculation of the potential, we need to find a way to let the system equilibrate in the presence of the vacancy while keeping the position of the skyrmion fixed. The global update algorithm, in contrast to the local update algorithm, does not allow only a subset of spins to reorder but all spins are free to equilibrate. With no further constraints the skyrmion would move to a local minimum. Thus we could not measure the distant dependent energy function anymore. To avoid the skyrmion from moving we keep one single spin fixed which is the spin in the

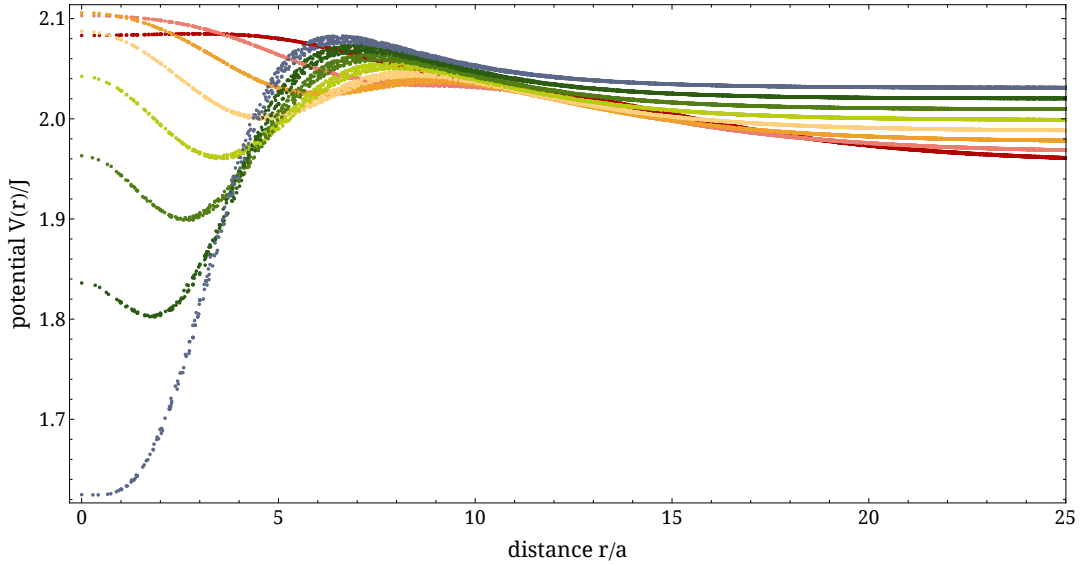

Figure 2.10: Potential of a single vacancy on a single skyrmion $V(r)$ as a function of distance r between the vacancy and the center of the skyrmion. Potential evaluated for parameters $D = 0.3J$ and $B = 0.05J$ (red) to $B = 0.12J$ (blue) in steps of $\Delta B = 0.01J$ using the order twelve local update algorithm.

center of the skyrmion. This choice makes sense as this is the relevant spin for measuring the distance between skyrmion and vacancy. Further this choice comes in handy as by construction the skyrmion is centered on a lattice site. It is also possible that in the local update algorithm the skyrmion gets destroyed by the vacancy as it looses its topological protection. By fixing the spin in the center of the skyrmion this problem also is excluded by construction.

The greatest advantage of this method is also its greatest disadvantage: all the spins except for the one in the middle of the skyrmion are being reordered. This does not only mean a higher accuracy compared to the local update method but also a much longer runtime in realtime for constant T. To calculate the energy difference with a vacancy compared to the case without the vacancy, in the global update method the whole system needs to be iterated which is an effort of the order L^2, where L is the system size. The local update algorithm, however, for any system size needs the same effort as the size of the subsystem is constant, given by the order of radius of convergence.

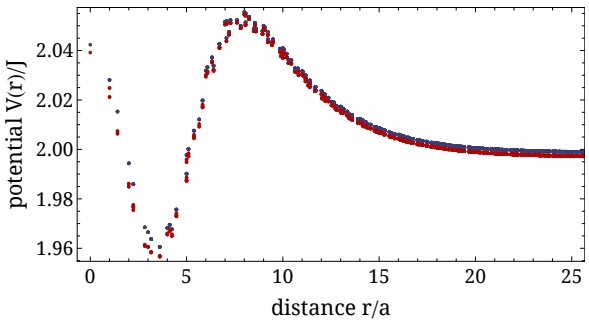

Figure 2.11: Comparison of the order twelve local update algorithm (blue) and the global update algorithm (red). Potential evaluated for parameters $D = 0.3J$ and $B = 0.09J$.

However, once we run this algorithm for a sufficiently long time, $T = 100\,{}^{1}/_{J}$, we recover the result shown in figure 2.11. Comparing the result to the one of the order twelve local update algorithm it returns almost the same function for the potential, shifted by a constant. For further analysis we will therefore use the results of the level twelve local update algorithm.

2.4.4. Scaling Properties

Going back to the free energy Ginzburg-Landau functional for Heisenberg spins, we can easily apply a scaling transformation $\mathbf{r} \to \mathbf{r}' = b^{-1}\mathbf{r}$ and recover the scaling relations $J' = J$, $D' = bD$ and $\mathbf{B}' = b^2\mathbf{B}$. Now we try the same for the potential of the vacancy. For this purpose we use that for a vacancy at distance $\mathbf{R}$ to the center of the skyrmion and size a^2 which should be small compared to the skyrmion we can write

$$V_a(\mathbf{R}) = \int \mathrm{d}^2 r \left[a^2\delta^2(\mathbf{r}-\mathbf{R})v(\mathbf{r})\right] \tag{2.39}$$

where we also introduce the potential density $v(\mathbf{r})$. If we now apply the scaling transformation $\mathbf{r} \to \mathbf{r}' = b^{-1}\mathbf{r}$ on this potential it also has to stay unchanged when rescaling the parameters.

$$\begin{aligned} V_a(\mathbf{R}) &= \int \mathrm{d}^2 r \left[a^2\delta^2(\mathbf{r}-\mathbf{R})v(\mathbf{r})\right] \\ &\overset{r=br'}{=} \int b^2\mathrm{d}^2 r' \left[a^2\delta^2(b(\mathbf{r}'-\mathbf{R}'))v(b\mathbf{r}')\right] \\ &= \int \mathrm{d}^2 r' \left[\left(\frac{a}{b}\right)^2 \delta^2(\mathbf{r}'-\mathbf{R}')b^2 v(b\mathbf{r}')\right] \\ &\overset{a=ba'}{=} \int \mathrm{d}^2 r' \left[\left(a'\right)^2 \delta^2(\mathbf{r}'-\mathbf{R}')v'(\mathbf{r}')\right] \\ &\overset{!}{=} V'_{a'}(\mathbf{R}') \end{aligned} \tag{2.40}$$

Here we used that $a' = b^{-1}a$ and $v'(\mathbf{r}') = b^2 v(\mathbf{r})$ but more important we found $V_a(\mathbf{R}) = b^{-2}V'_a(\mathbf{R}')$ which relates the potentials leaving the vacancy size unchanged or, alternatively, resizing the vacancy. Also numerically we obtain this scaling behaviour by rescaling the skyrmion, tuning the parameters D and B, but leaving the vacancy a single site. The results for several sets of parameters are shown in figure 2.12. As can be obtained from the plots the scaling law

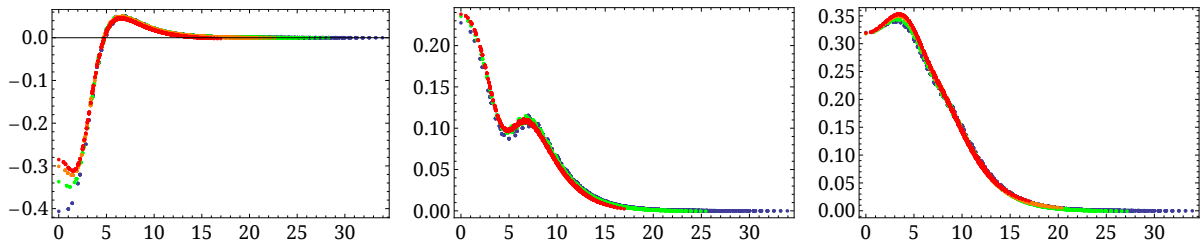

Figure 2.12: Comparison of scaling of vacancy potentials with $D = 0.5bJ$ (left), $D = 0.4bJ$ (center) and $D = 0.3bJ$ (right) all at $B = 0.12b^2J$. Left: $b = 1$ (blue), $b = 4/5$ (green), $b = 3/5$ (orange), $b = 1/2$ (red). Center: $b = 1$ (blue), $b = 3/4$ (green), $b = 1/2$ (red). Right: $b = 1$ (blue), $b = 5/6$ (green), $b = 2/3$ (orange), $b = 1/2$ (red).

is fulfilled for almost all sizes of skyrmions. Only in the parameter regime where the pressure from the magnetic field on the skyrmions is very big the scaling shows deviations, see right figure. This incorrectness might be caused by the local update algorithm as the radius of equilibration is of the order of the radius of the skyrmion for the strongest Dzyaloshinskii-Moriya interactions (blue). The twice as big skyrmion in the rescaled case (red) has less freedom to move in this algorithm and hence might generate more accurate results for the potential. We therefore see the scaling relation stated above to be fulfilled and therefore use rescaled units in the following, see section 1.4.

2.4.5. Asymptotic Behaviour

For analytic purposes it makes sense to describe the single skyrmion in a ferromagnetic background in spherical coordinates (θ, ϕ)

$$\begin{aligned} \mathbf{M} &= (\,\sin(\theta)\cos(\phi),\, \sin(\theta)\sin(\phi),\, \cos(\theta)\,) \\ \mathbf{r} &= (\,\rho\cos(\varphi),\, \rho\sin(\varphi)\,)\,. \end{aligned} \tag{2.41}$$

These coordinates are to depend on the distance ρ to the center of the skyrmion themselves. It has been shown [2, 32] that in the case of the skyrmions discussed here, socalled *Bloch type* skyrmions, the one angle is given by $\phi = \frac{\pi}{2} + \varphi$ for radial symmetric solutions. This corresponds to the combing of the hedgehog configuration and is determined by the type of Dzyaloshinskii-Moriya interaction. Further the differential equation which determines the dependency $\theta(\rho)$ has been found to be

$$\frac{\mathrm{d}^2\theta}{\mathrm{d}\rho^2} + \frac{1}{\rho}\frac{\mathrm{d}\theta}{\mathrm{d}\rho} - \frac{1}{\rho^2}\sin(\theta)\cos(\theta) + \frac{\sin^2(\theta)}{\rho} - \frac{B}{J}\sin\theta = 0 \tag{2.42}$$

and was solved only numerically or in the limiting cases. The only parameter which enters here is the ratio B/J, the absolute value of the magnetic field in units of the ferromagnetic coupling. However, the asymptotic behaviour has been determined to be

$$\theta(\rho \to \infty) \sim \exp\left[-\sqrt{\frac{B}{J}}\,\rho\right]. \tag{2.43}$$

It therefore seems reasonable to assume that for large distances the potential of the vacancy shows a similar exponential decay. Fitting an exponential function with the estimated exponent to the potential shows that indeed this assumption yields good results, see figures 2.13. The potential decays exponentially with the same exponent as the angle $\theta(\rho)$. To fit the potential in the regions close to the vacancy we use a polynomial fit. As we have a lot of data points due to the possibility of deplacing the skyrmion and using the local update algorithm, section 2.4.2, we can perform the polynomial fit to a very large order. We use an even polynomial series to order $\mathcal{O}(x^{100})$ as it describes well the potential and does not create phantom peaks anywhere, see figures 2.13.
From the figures we see that the potential is well described by the polynomial fit for small distances and the exponential fit for larger distances. The exponential fit is chosen such that the combined function is continuously differentiable.

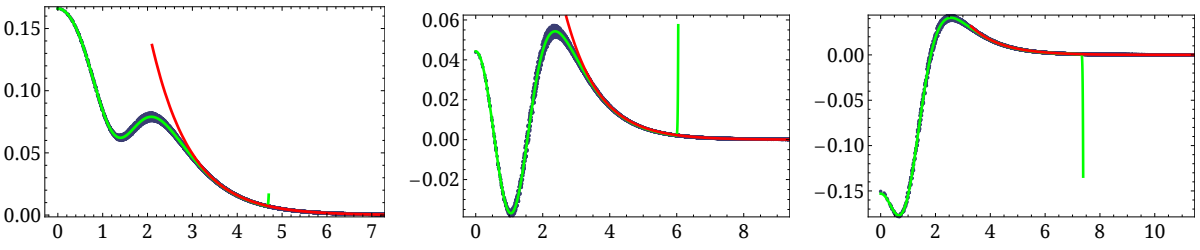

Figure 2.13: Comparison of rescaled potentials $V/V_0(r/R)$, see section 1.4, from the local update algorithm (blue), polynomial fit (green) and exponential fit according to 2.43 (red) of the potential. Parameters are $\zeta = 7/9$ (left), $\zeta = 1$ (center) and $\zeta = 11/9$ (right).

2.5. Comparing Thiele to the Full Micromagnetic Simulation

In section 2.2 we use the Thiele method, where the skyrmion is assumed to be a solid object, to gain insight into the interaction of a skyrmion with a vacancy analytically. The assumption to have a solid skyrmion does not seem reasonable, taking into account that it is an extended object where locally the forces acting on the spins may differ a lot. Additionally the vacancy itself is a hole in the two-dimensional lattice of spins which intrinsically is a deformation of the skyrmion. Hence what makes more sense is that the skyrmion deforms. Further there might be internal modes of the skyrmion which play a role when overcoming an energy barrier. Nevertheless, in this section we show that the Thiele method gives good results when including the numerically determined potential of the vacancy.
The equation of motion in the Thiele approximation, see equation 2.26, directly returns a velocity vector for every point in the two-dimensional plane. If we plot the resulting vector field and interpolate between the velocity vectors, we recover the trajectories of a skyrmion from the Thiele method. As we recover immediately a velocity from the position, we have no mass term playing a role and can immediately plot *all* possible trajectories. For the plotting and interpolating we use the function *StreamPlot* in the program *Mathematica* which has this feature build-in.
The comparison of the trajectories of the full micromagnetic simulation, which partially are also shown in figure 2.6, to the trajectories obtained from the Thiele ansatz combined with the potential of the vacancy obtained from the local update algorithm of order twelve is shown in figure 2.14. As can be seen in the figures, the trajectories resulting from the Thiele method and the full micromagnetic simulation match well. Therefore the Thiele method gives a very good approximation to the simulation of the full micromagnetic LLG equation 2.18.

2.6. The Separatrix: Dividing Capturing and Non-Capturing Trajectories

In the previous chapters we have already seen as a side product that a skyrmion can be captured by a vacancy. Examples for those trajectories are shown in figure 2.14 where both the results from the full micromagnetic simulation and from Thiele match. By definition, the trajectories which lead to a pinning by the vacancy must end in the stable fixed point of the system. This fixed point is unique as the potential has only one local minimum for finite distance, see section 2.4, and the rotation symmetry is broken due to the direction of the current density and the magnus force. Further this stable fixed point can be calculated from the potential using the fixed point analysis of Thiele's equation, see section 2.3, as can be also all the other unstable fixed points and their eigenvectors.
To analyse which trajectories lead to a pinning of the skyrmion we define the so-called *separatrix*. The separatrix is the curve which envelops all starting points for capturing trajectories. As the Thiele equation does not contain any mass but directly returns a velocity vector for a given point in space, all points of a trajectory are possible starting positions. Therefore all capturing trajectories have to be completely within the capturing area enclosed by the separatrix. As this also implies that two trajectories can not cross except in fixed points, the boundary of the capturing area is given by a set of critical trajectories. In our setup this set of trajectories consists of at least two critical solutions: one that is the boundary to the upper non-capturing trajectories and one that separates the lower non-capturing trajectories. In the following we intruduce a stable and fast algorithm to find the separatrices numerically as we are not able to find them analytically.

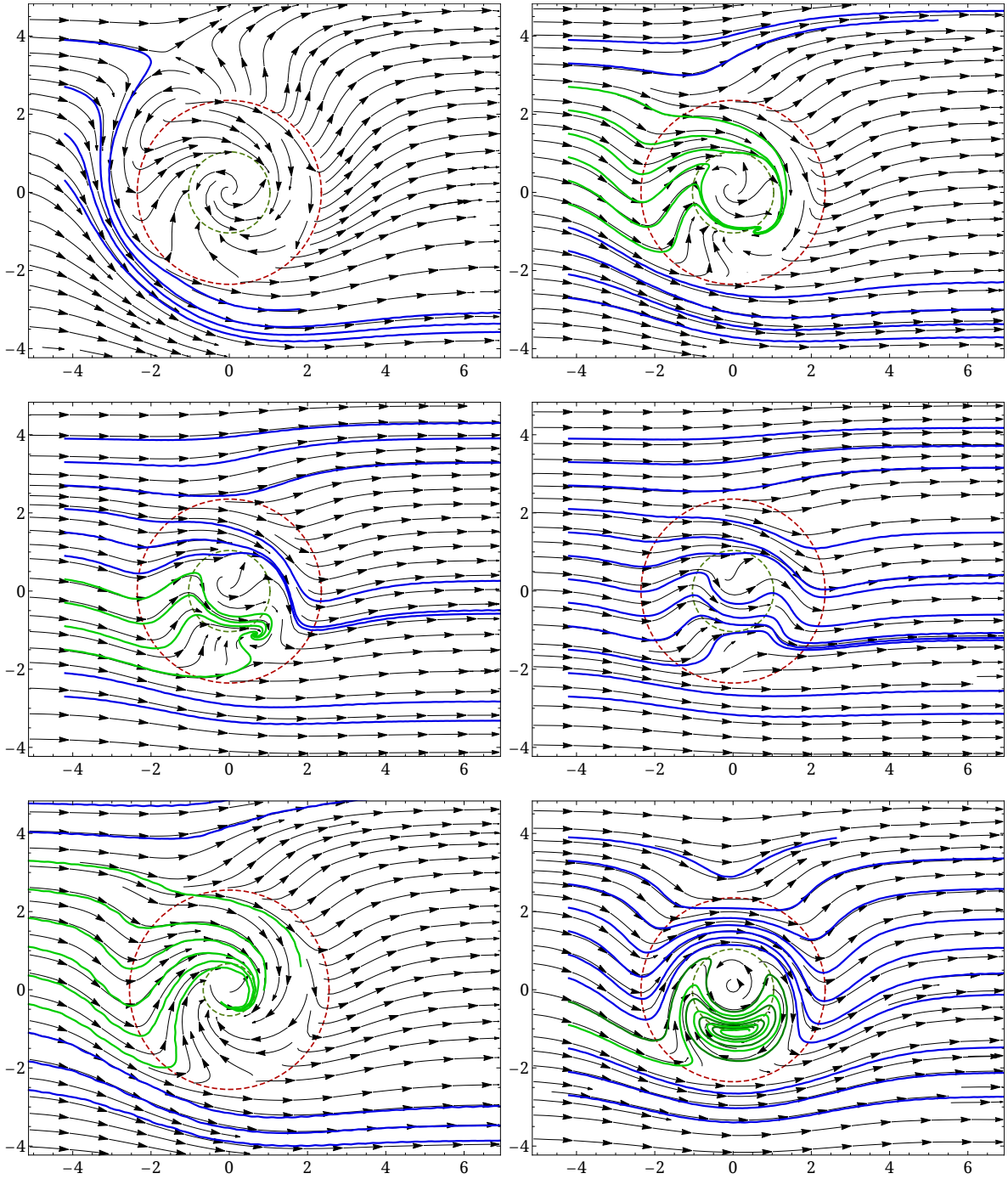

Figure 2.14: Comparison of trajectories of the single skyrmion obtained from the micromagnetic simulation (blue/green) and the Thiele method with the local update algorithm of order twelve. Parameters are $\zeta = 1$, $\alpha = 0.4$ with current densities $j = 0.015 j_0$ (top left), $j = 0.037 j_0$ (top right), $j = 0.074 j_0$ (center left), $j = 0.11 j_0$ (center right). Bottom left: $\zeta = 11/9$, $\alpha = 0.4$, $j = 0.020 j_0$. Bottom right: $\zeta = 1$, $\alpha = 0.04$, $j = 0.037 j_0$. The green trajectories are ones capturing a skyrmion, the blue trajectories pass by. For better orientation, the green circle indicates the potential minimum, the red circle the maximum.

To find the separatrix we start with a very general consideration: the separatrix, by definition, separates capturing from evading trajectories. As all trajectories which start far on the right of the vacancy (assuming a current to the right as in all figures showed before) cannot be pinned, the separatrix, and therefore the critical trajectories, must be limited to the right. If we now assume that the critical trajectory $\mathbf{r}_{\text{crit}}$ starts at a finite distance to the vacancy at a finite time t_0 it needs to have a finite length L

$$L = \int_{t_0}^{\infty} \|\dot{\mathbf{r}}_{\text{crit}}(t)\| \text{dt} \overset{!}{<} \infty \tag{2.44}$$

and hence

$$\dot{\mathbf{r}}_{\text{crit}}(t \to \infty) = 0. \tag{2.45}$$

This equation is already known as the condition for a fixed point, see equation 2.28. Therefore the critical trajectories have to end in a fixed point. However, we can already argue that this can not be the *stable* fixed point as it is attractive in all directions. To be part of the boundary of the capturing area at least one repulsive direction out of the area would be the condition.
Using the same argument as in equation 2.44 also for the starting time $t_0 \to -\infty$ we find that the length of each critical trajectory is finite only if it also *starts* in a fixed point. Therefore the separatrix encircles a finite area if and only if all critical trajectories also start in fixed points. On the contrary, for having an infinite area of capturing starting points, exactly two of the critical trajectories have to fulfill $x(t = -\infty) = -\infty$, meaning they start at infinite distance to the vacancy.
Figure 2.15 shows the trajectories obtained from the Thiele method and the fixed points including their eigenvectors. From these figures we can already see that the separatrix, which is also shown in the figures, always includes the lowest fixed point. Indeed, this always has to be the case. The idea is the following: due to the magnus force the attractive part of the potential gains a clockwise rotating contribution. The trajectories going into the stable fixed point from the right therefore originally have to come from above the fixed point. Additionally there are the trajectories which enter from the left, driven by the current density. Both these trajectories, pointing in opposite direction, come together below the stable fixed point. The topological defect resulting at the meeting point must be a semidefinite fixed point as in this point there is no direction defined but it has incoming eigenvectors. It is obvious that this fixed point has to be the already mentioned lowest fixed point as it is the only one below the stable fixed point. Therefore the lowest fixed point is always included in the separatrix.
The knowledge about the role of fixed points in the separatrix, especially the lowest one, provides a very efficient way of finding the critical trajectories numerically. Instead of starting the iteration on the far left from the vacancy and iterating the Thiele equation hoping to find a critical trajectory we can directly start from the lowest fixed point. This one is always included in the separatrix and its two unstable eigenvectors must be the ending points of two critical trajectories. Now it comes in handy that the critical trajectories become unstable close to the semidefinite fixed point: being closer to the fixed point they become more sensitive to deviations from the critical trajectory and might escape in the direction of the outgoing flow. If we now do the reversed iteration, $\partial_t \to -\partial_t$, of the Thiele equation 2.26 starting at the semidefinite fixed point this instability even turns into a stability of the iteration. This stability then solves also another problem which intrinsically arises: the initial velocity in the fixed point is zero. Hence the iteration does not only have no initial step width but also no step direction. Here the reversed instability around the fixed point helps. We make a small

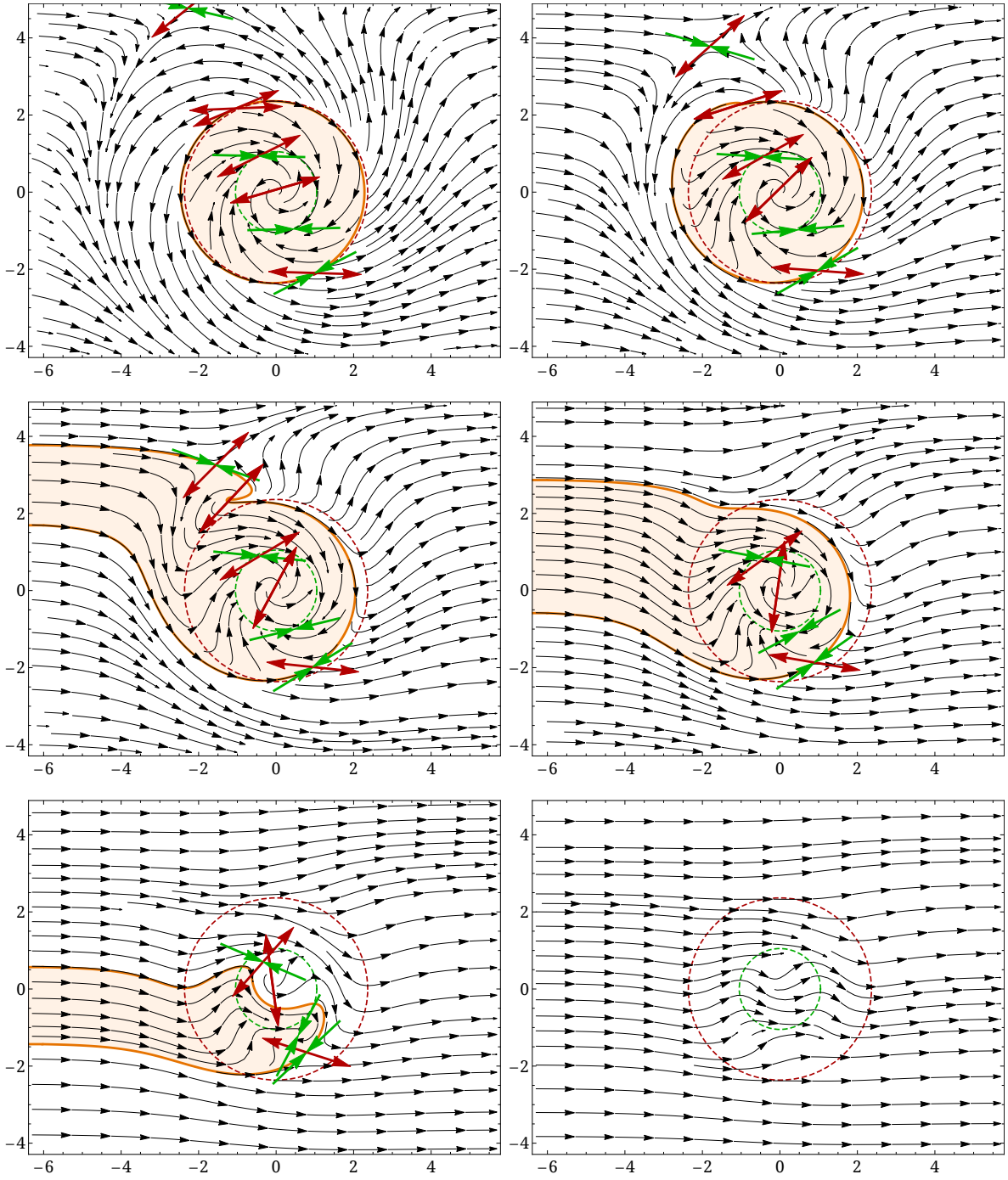

Figure 2.15: Trajectories (black) of the single skyrmion obtained from the Thiele method with the local update algorithm of order twelve. Parameters are $\zeta = 1$, $\alpha = 0.4$ and current densities $j = 0.0037 j_0$ (top left), $j = 0.011 j_0$ (top right), $j = 0.0185 j_0$ (center left), $j = 0.037 j_0$ (center right), $j = 0.074 j_0$ (bottom left), $j = 0.15 j_0$ (bottom right). The orange curve is the separatrix; the orange area is the capturing area. Red arrows mark outgoing flow and green arrows mark ingoing flow at a fixed point. Eigenvectors are obtained according to section 2.3. For better orientation, the green circle indicates the potential minimum, the red circle the maximum.

first step into the reversed direction of one of the unstable eigenvectors. As the iteration is stable with respect to the critical trajectory which we are looking for the error we make with this step will then be minimized when running the iteration. The iteration starting from the lowest fixed point continues until it has reached another fixed point or is sufficiently far on the left side away from the vacancy. If the end of a critical trajectory is another fixed point this typically is an unstable fixed point and therefore can not have attractive eigenvectors. As the upper fixed point of an open separatrix must be a semidefinite fixed point, just as the lowest one, to allow for an incoming critical trajectory, we restart the iteration from the next upper semidefinite fixed point. Everytime the iteration beginning from one fixed point is finished we look for the end points of the critical trajectories: if two trajectories end at infinity and all others are connected we have an open separatrix, if all trajectories together form a closed loop we have a closed separatrix and if there is only one trajectory going to infinity or if the loop is not closed then there are either to many or too less fixed points included. With this code we can calculate the separatrices in a very efficient way. The results are shown in figures 2.16.

We find that for all magnetic field strengths we have closed separatrices at low current densities. This means that a skyrmion which approaches the vacancy from far can not be captured but gets repelled. Hence we refer to this as the *repulsive phase*. On the other hand, a skyrmion which is already in the area defined by the separatrix around to the vacancy stays pinned. The closed separatrix in this phase consists of two critical trajectories, both starting in the upper unstable fixed point close to the maximum of the vacancy and ending in the semidefinite lower fixed point. When turning up the current density we see that the separatrix deforms especially in the upper left region towards the semidefinite upper fixed point. From a critical current on the separatrix then spontaneously breaks open at the upper fixed point. The current is given as the one for which the trajectory leaving the upper semidefinite fixed point downwards exactly enters the lower semidefinite fixed point. This first critical current we only determine numerically as we are not able to find an analytic expression for it.

After the separatrix has opened, it defines an infinite capturing area. First it opens on the upper side of the vacancy directly at the upper fixed point. After broadening up it decays again. In the case of a lower magnetic field the decay happens very rapidly. For other field strengths the decay takes longer but still is guided by rapid jumps of the separatrix shape. The exact shape of the separatrix always is strongly influenced by the fixed points as they ofter twist whirls into the separatrix which is an effect of the magnus force. As the opened separatrix allows for capturing a skyrmion which approaches the vacancy in the channel given by the capturing area we refer to this as the *capturing phase*. A skyrmion which is outside the capturing channel evades the vacancy. Just as in the repulsive phase, previously pinned skyrmions also stay pinned. For current densities close to the second critical current the separatrix smoothly shrinks until it disappears without closing again. While the capturing area get smaller it also happens that for a certain current density the initial stable fixed point for ultra low current densities is part of the separatrix. For even higher current densities the intial stable fixed point is not included in the capturing area anymore. This means that dependent on the speed for turning up the current density the initially pinned skyrmion can either stay pinned as for a slow increase of the current density it can follow the fixed point whereas for a fast turning up of the current it gets depinned.

Finally, for current densities larger than the second critical current density, the stable fixed point has annihilated with the lower semidefinite fixed point and there is no pinning of skyrmions anymore. All skyrmions now move freely. This last regime of parameters we call the *free phase*.

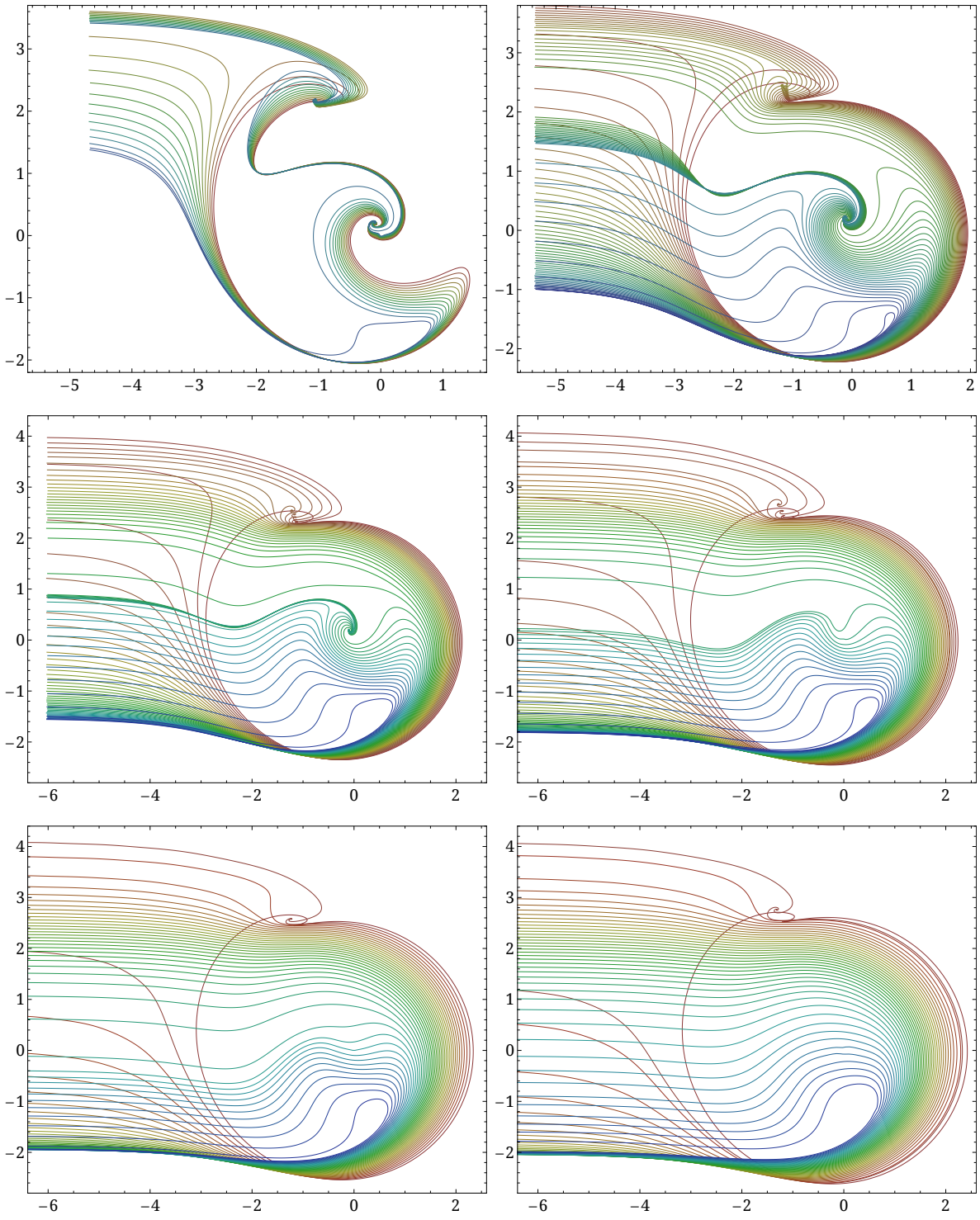

Figure 2.16: Qualitative comparison of separatrices for the trajectories of the single skyrmion in units of R. Parameters are $\alpha = 0.4$ and $\zeta = 7/9$ (top left) to $\zeta = 12/9$ (bottom right) in steps $\Delta\zeta = 1/9$ from left to right, top to bottom. The plots show a set of separatrices from the lower critical current density (red) and to the upper critical current density (blue). In each plot the difference between two separatrices Δj is constant but different in each plot. The difference Δj increases with ζ. Values for the current density j can be obtained from figure 2.21. Note that the first two figures have a different plot range.

2.7. The Capturing Cross Section

In the previous section an efficient way to numerically compute the separatrices for capturing and non-capturing trajectories has been derived and applied. However, the results from this method are very detailed and should better be described with less effort. Therefore we define a new order parameter for the different phases of the interplay of a skyrmion with a vacancy which is the *capturing cross section*. This quantity is the width of the capturing channel and therefore a measure for the efficiency of capturing. According to this definition, in the repulsive and the free phase the capturing cross section is zero as in these cases the skyrmion can not be captured. Differently, in the capturing phase the skyrmion can be captured and therefore the cross section in this phase is finite.
As the separatrices were already determined numerically in the previous chapter, 2.6, we obtain the capturing cross sections from this data immediately. Figure 2.17 shows the resulting capturing cross sections for different skyrmion shapes ζ. We find that the behaviour of the capturing cross section is highly non-trivial. In fact it is strongly influenced by the fixed points of the Thiele equation 2.26. Every kink in the graph of the capturing cross section results from an interaction effect of the separatrix with a fixed point. However, the kinks corresponding to the same events can be found again in the capturing cross sections for other magnetic fields.

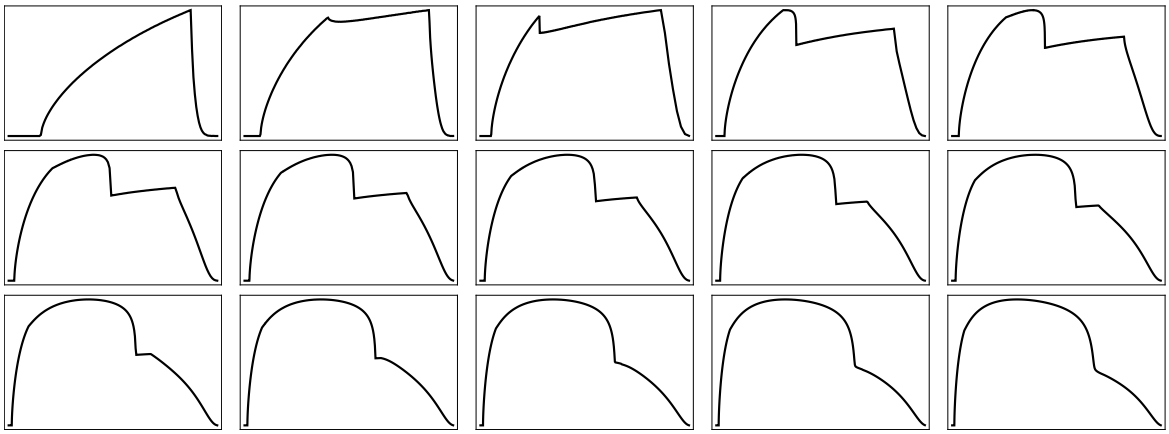

Figure 2.17: Capturing cross sections σ/R for $\alpha = 0.4$ and different values for the skyrmion shapes from $\zeta = 7/9$ (top left) in steps of $\Delta\zeta = 1/36$ to $\zeta = 21/18$ (bottom right) as a function of the current density j/j_0, chosen in a suitable range.

As an example, figure 2.18 shows the capturing cross section for $B = 0.09J$ with the different current densities at which the separatrix interacts with the fixed points. The first current that is marked in the plot is the first critical current at which the separatrix opens. This current is characterized by the trajectory from the upper semidefinite fixed point passing the vacancy on the left and ending in the lower semidefinite fixed point. Below, we will describe analytically the shape of the capturing cross section above this first critical current. In this regime the separatrix always includes the upper semidefinite fixed point. At the current density marked by the second line the separatrix gets depinned from this fixed point and the unstable fixed point below as well. Then only for slightly higher current densities these two fixed points annihilate with each other. After the depinning of the separatrix from these fixed points there is only the lower semidefinite fixed point involved into the separatrix. The separatrix starts moving downwards until it gets attracted by the remaining upper semidefinite fixed point close

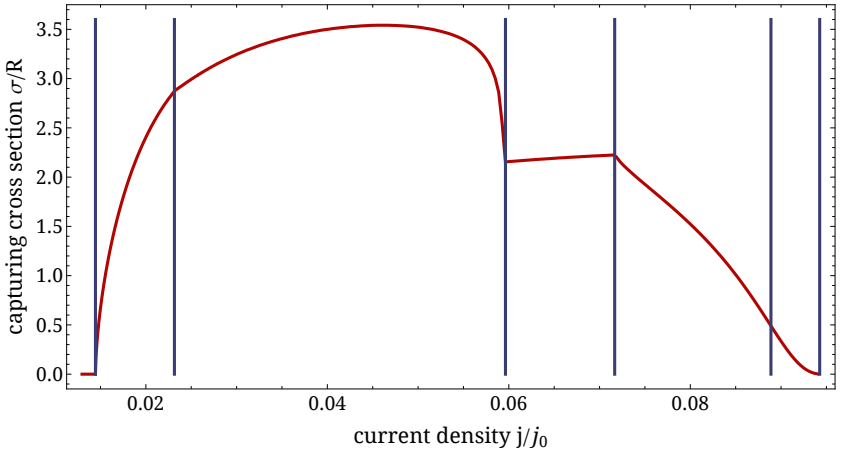

Figure 2.18: Capturing cross section σ/R (red) for $\zeta = 1$, $\alpha = 0.4$ plotted as a function of the rescaled current density. Vertical lines (blue) mark the current densities where the capturing cross section markably changes.

to the minimum of the potential. The third line marks the current density where the separatrix includes this upper semidefinite fixed point and the unstable fixed point next to it. This can be seen well e.g. in the center left plot of figure 2.16 where the green curves have the waves-like whirl in the middle. While the separatrix is pinned to these points the capturing cross section builds up a linear plateau until at higher currents, marked by the fourth line, the separatrix again leaves the fixed points. The only fixed point included then is again the one below the stable fixed point. From then on the capturing cross section steadily shrinks until it smoothly goes to zero at the last marker. The second critical current at this point can be determined analytically from the potential, see equation 2.36. One further line is added which does not mark a kink nor a direct interaction of the separatrix with a fixed point: at the current density marked by the fifth line, the stable fixed point for ultra low current, $j \to 0$, is not included in the capturing area anymore. As a consequence, for a sudden switching on of the current density the skyrmion would be released, whereas for a slow increase of the current density it would stay pinned and follow the stable fixed point.

As already mentioned, the capturing cross section in some regions very much looks like simple analytic functions: for currents just above the first critical current it reminds of a square root, in the middle it looks linear, close to the second critical current it looks polynomial. For the case of the opening of the separatrix the behaviour can be described as follows: at the first critical current density the separatrix breaks open at the upper semidefinite fixed point. In the proximity of this fixed point the trajectory follows the linearized Thiele equation 2.33. As this fixed point is semidefinite, meaning is has a positive and a negative eigenvalue, we can diagonalize the linearized Thiele equation. We denote the eigenvectors as $\{\mathbf{b}_+, \mathbf{b}_-\}$ with the eigenvalues $\{\lambda_+, \lambda_-\}$. The index is chosen such that the eigenvector which belongs to the inwards flow is given by $\mathbf{b}_-$ with $\lambda_- < 0$ and the outwards pointing eigenvector is $\mathbf{b}_+$ with $\lambda_+ > 0$. The initially coupled differential equations for both components in the euclidean basis then become decoupled differential equations in the eigenvector basis and hence can be solved easily. The solutions in the eigenvector basis then are given by

$$\mathbf{x}_\pm(t) = x_\pm(0) e^{\lambda_\pm t} \mathbf{b}_\pm. \tag{2.46}$$

These two solutions we can relate to each other by solving for the time dependency and inserting it in the other equation. The result can be expressed as

$$x_+(0) = x_+(t) \left(\frac{x_-(t)}{x_-(0)} \right)^{-\frac{\lambda_+}{\lambda_-}} \tag{2.47}$$

which will come in handy soon. As the eigenvalues depend on the distance of the fixed point to the vacancy, they indirectly also depend on the current density. This dependency we neglect in the following as the fixed point for small deviations Δj does not move a lot. To determine from these solutions around the upper fixed point the behaviour of the capturing cross section, we use that the upper critical trajectory does not move much when turning up the current density. Basically it is given by the incoming eigenvector of the fixed point. This can clearly be seen in figure 2.16. The lower critical trajectory behaves differently and determines the opening of the capturing area as being exactly the distance to the other critical trajectory. The capturing cross section, which is given by the opening width of the capturing area, therefore mainly is the initial offset of the lower critical trajectory from the incoming eigenvector of the fixed point. In terms of the solution 2.47 this initial offset and therefore the capturing cross section is direct proportional to $x_+(0)$. Assuming now that the offset from the outgoing eigenvector of the fixed point after passing the fixed point only depends linear on the current we recover the equation:

$$x_+(0) \propto (x_-(t))^{-\frac{\lambda_+}{\lambda_-}} \propto (j - j_c)^{-\nu} . \tag{2.48}$$

An exact expression for the eigenvalues is derived in the appendix, see equation A.95. Defining the exponent $\nu = \frac{\lambda_+}{\lambda_-}$ which is given by the previous analysis we can make a fit to the data to show that these assumptions indeed yield good results, see figure 2.19. As the eigenvalues themselves only slightly depend on the current, we calculate them for the critical current density and keep them constant. The plots show that indeed close to the critical current these assumptions are good as the analytic results are very close to the numerical data. Further it is shown in figure 2.20 that the first critical current density depends linear on the magnetic field when using numerical units. This is shown by plotting the first critical current density as a function of the magnetic field strength as well as a linear fit to the data, see the inset. The differences between numerical data and linear fit are of the order of the scanning resolution. Also the dependence of the second critical current density on the magnetic field strength can be determined by a fit. In figure 2.20 it is shown that in numerical units an exponential fit describes the behaviour perfectly, see the inset. When going over

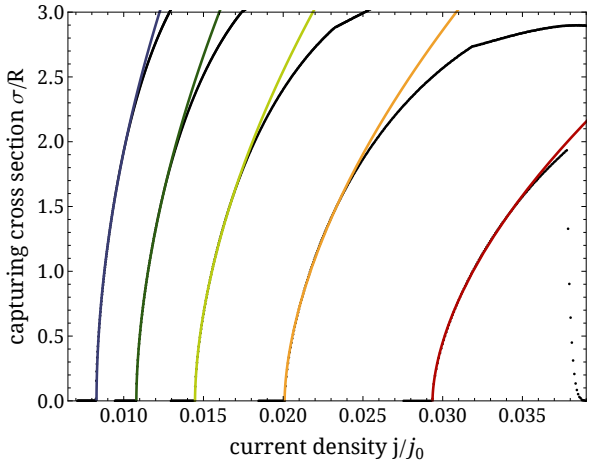

Figure 2.19: Capturing cross sections for $\alpha = 0.4$ and shapes from $\zeta = 7/9$ (red) to $\zeta = 11/9$ (blue) in steps of $\Delta\zeta = 1/9$ plotted as a function of the current density. The colored solid lines are fit funtions $f_{\text{fit}}(j) = a(j-b)^{-\nu}$, the black points are the numerical data.

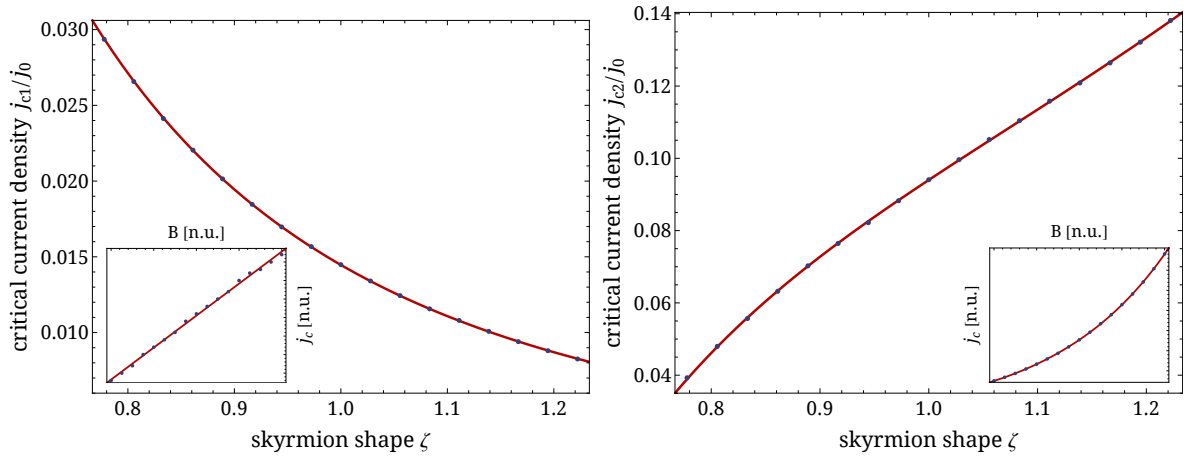

Figure 2.20: First (left) and second (right) critical current densities as a function of magnetic field strength. Comparison of numerical data (dots) and fit function (solid line). The optimal fit functions are determined to be $j_{c1}^{\text{fit}}(\zeta)/j_0 = 0.0029\zeta^{-2} + 0.0116\zeta^{-3}$ and $j_{c2}^{\text{fit}}(\zeta)/j_0 = [-0.051 + 0.005\exp(3.3\zeta)]\zeta^{-3}$. The insets show the linear and exponential fit gained in numerical units where they are much more obvious.

to the system of units of the contiuous theory the fitting functions become more complicated to describe the numerical data correctly.

2.8. Summary: Pinning a Skyrmion at a Vacancy

In this chapter it has been shown numerically and analytically that a single skyrmion can be pinned at a vacancy.
We first simulated the full micromagnetic system given by the LLG equation, see section 2.1. Then we introduced an algorithm, the *local update algorithm*, to determine the potential of a vacancy acting on a skyrmion numerically, see section 2.4.2. Concerning the potential we showed that it obeys an analytically expected scaling law, section 2.4.4, and that the asymptotic behaviour for large distances can approximately be given analytically. Using the potential and analytic results from the Thiele method, section 2.2, we found in a comparison to the full micromagnetic simulation that they are in a very good agreement. Further the analytic results allowed for calculating the *separatrix* of the system in a very efficient way. From this data we obtained the *capturing cross section* as a new order parameter of the system and were also able to analytically predict its behaviour. The separatrices and capturing cross sections showed the existence of three different phases in the model:

- the *repulsive phase*, in which a skyrmion that is pinned to a vacancy stays pinned but any other initially not pinned skyrmion moves around the vacancy freely,
- the *capturing phase*, defined by an opened separatrix and therefore finite capturing cross section, where a skyrmion that moves freely can get captured by a vacancy and stays pinned,
- the *free phase*, in which a skyrmion never is pinned.

The regimes for the different phases, given by the first and second critical current density, can

nicely be displayed in a phase diagram using the capturing cross section as a suitable order parameter. The resulting rescaled phase diagram is shown in figure 2.21.

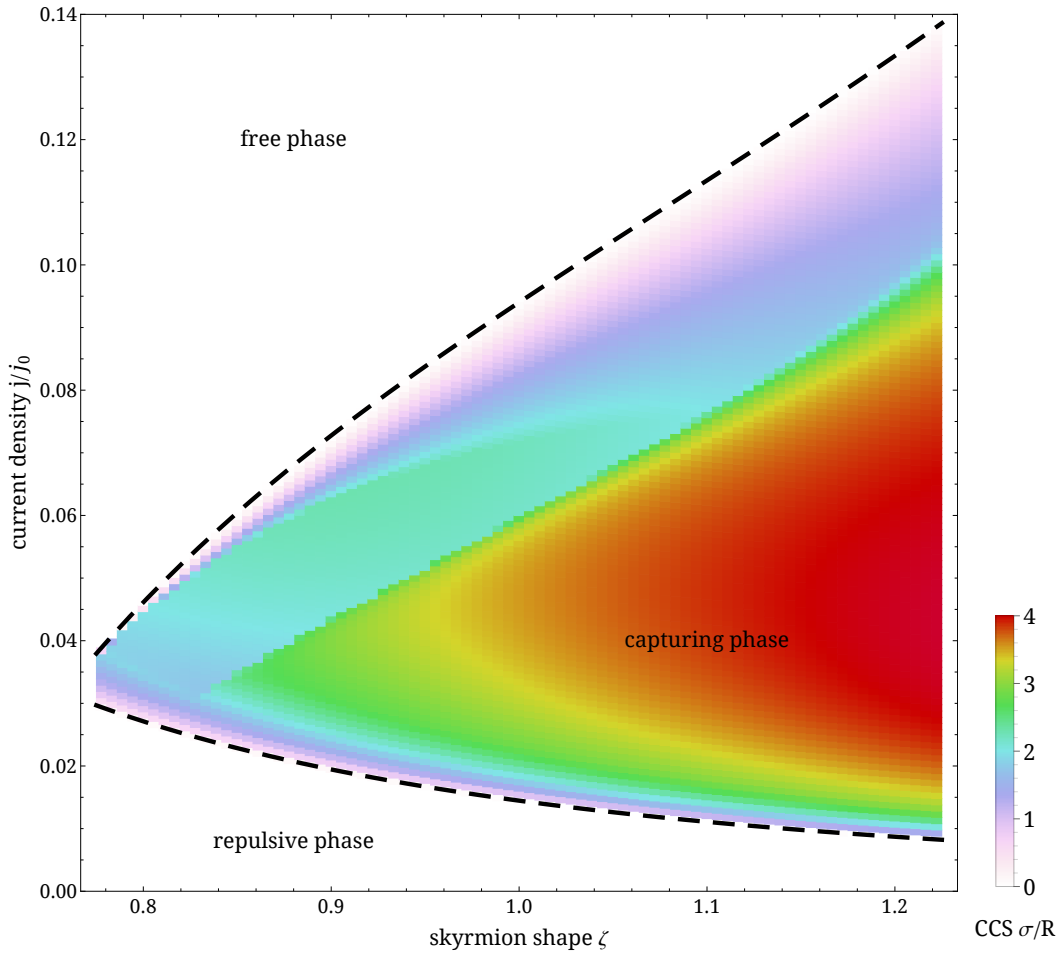

Figure 2.21: Phase diagram for the repulsive, capturing and free phase shown in dependence of the magnetic field and current density at zero temperature. The parameters $\alpha = \beta = 0.4$ are chosen constant.

3. The Skyrmion Hall Effect, Speed-Up and Effective Damping

3.1. The Skyrmion Hall Effect

In this chapter the Hall effect, which is an additional contribution perpendicular to the applied current, generated by a vacancy shall be analyzed. As an introductory appetizer once again we refer to a figure which we have already seen in the previous chapter and which is shown here again, see figure 3.22. The figure shows an effect which the magnus related part in the force acting on the skyrmion has on the trajectories. For a negative gyrocoupling constant $\mathcal{G} < 0$ the magnus term in the repulsive regime creates a circular motion in the mathematical positive sense, compare equation 2.26. Therefore for the trajectories, here in the repulsive phase, we find that a skyrmion approaching the vacancy from the left obeys not only the separatrix but also one further critical trajectory: either it arrives above the upper semidefinite fixed point and passes the vacancy *above* or it arrives below this fixed point which is the end of the above mentioned critical trajectory and passes the vacancy *below*. As this fixed point itself is placed above the vacancy and the repulsion for the upper trajectories therefore is comparably weak one may assume that there is a net flux of skyrmions passing the vacancy below.

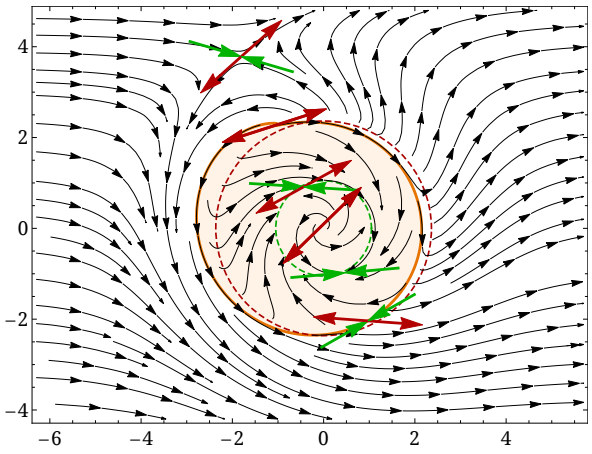

Figure 3.22: Trajectories of the single skyrmion with fixed points and separatrix, compare figure 2.15.

In the following we will only discuss the system in either the repulsive or the free phase but not the capturing phase. In the last case for large systems the capturing phase would always lead to pinning of skyrmions. Therefore in this case the interaction of pinned and free skyrmions becomes important or due to collective pinning there would just be no Hall effect.

3.1.1. The Skyrmion Hall Effect in the Repulsive Phase

We start with assuming a skyrmion in a two-dimensional plane which moves driven by a current density j in the repulsive phase. In the plane there are placed vacancies of equal size which interact with the skyrmion. Further we will assume the average distance between two vacancies, ξ, to be very large compared to the radius of the skyrmion, $\xi \gg R$. In this limit we can treat each interaction of a skyrmion with a vacancy as a two particle interaction where basically everything that we have found in chapter 2 still holds.
Starting from this setup we can define the total displacement ΔY caused by N vacancies:

$$\Delta Y = \sum_{i=1}^{N} \Delta y(y_0^i) \tag{3.49}$$

which is the sum over the independent local displacements $\Delta y(y_0^i)$, defined as the difference in the coordinate y before and after having passed the vacancy $\Delta y(y_0) = y(t \to \infty) - y(t = 0)$.

Note that here the coordinate y is chosen as the direction perpendicular to the current density. The independent summation of displacements is motivated by the large distance between the vacancies. Any displacement therefore should be treatable independently.
Now we can use that the vacancies are assumed to be randomly distributed. Therefore we can replace the summation over all positions of vacancies by an average over the impurity positions. For systems of a large extension L and a small density of vacancies n this is a good approximation. Hence in this limit the *total displacement* is given by the average total displacement which can be written as

$$\langle \Delta Y \rangle = \langle \sum_{i=1}^{N} \Delta y(y_0^i) \rangle = N \, \frac{1}{L^2} \int_{L^2} \Delta y(y_0) \, \mathrm{d}(x_0, y_0) \approx nL \langle \Delta y \rangle_\infty . \tag{3.50}$$

Here we further introduced the *offset integral* $\langle \Delta y \rangle_\infty$. It contains the integration over the y-axis only and as the system size is assumed to be very large and the effect of a vacancy decays exponentially, it is a good approximation to extend the integration to infinity. The offset integral is defined as:

$$\langle \Delta y \rangle_\infty = \int_{-\infty}^{\infty} \Delta y(y_0) \, \mathrm{d}y_0 \tag{3.51}$$

and can be calculated as a function of the current density. Further it is independent of the system size and the density of vacancies as long as they are sufficiently dilute. We can thus already conclude that the total displacement in the dilute limit depends linear on the density of vacancies.
Before calculating the offset integral we make a first assumption on the solution: So far we have seen in figures 2.15 and 3.22 that the upper semidefinite fixed point acts as a separator of trajectories passing above or below the vacancy. Trajectories passing above this fixed point are only pushed slightly away from the vacancy, hence there is no big contribution to the offset integral coming from these trajectories. Another observation is that trajectories which are guided below the vacancy almost arrive at the same finite point whereas trajectories passing below the vacancy anyways are repelled only slightly, just as the ones passing above. Hence we estimate that the main part contributing to the offset integral comes from the trajectories which really are pushed down from the fixed point. As this fixed point for low current densities is far away from the maximum of the potential, which can also be seen in the figures, we can approximate the potential in this region with an exponential decay, compare section 2.4.5:

$$V(r) = V_0 \exp\left[-\sqrt{\frac{B}{J}} r \right] . \tag{3.52}$$

In contrast to the previous sections we can now use this potential to solve the fixed point equation 2.29 for the radial distance of the fixed point from the center of the vacancy:

$$j\gamma = |V'(r_{\mathrm{FP}})| = \sqrt{\frac{B}{J}} V_0 \exp\left[-\sqrt{\frac{B}{J}} r_{\mathrm{FP}} \right] \tag{3.53}$$

so that finally we recover for the distance of the fixed point to the center of the vacancy:

$$r_{\mathrm{FP}} = -\sqrt{\frac{J}{B}} \ln\left[\sqrt{\frac{J}{B}} \frac{j\gamma}{V_0} \right] \tag{3.54}$$

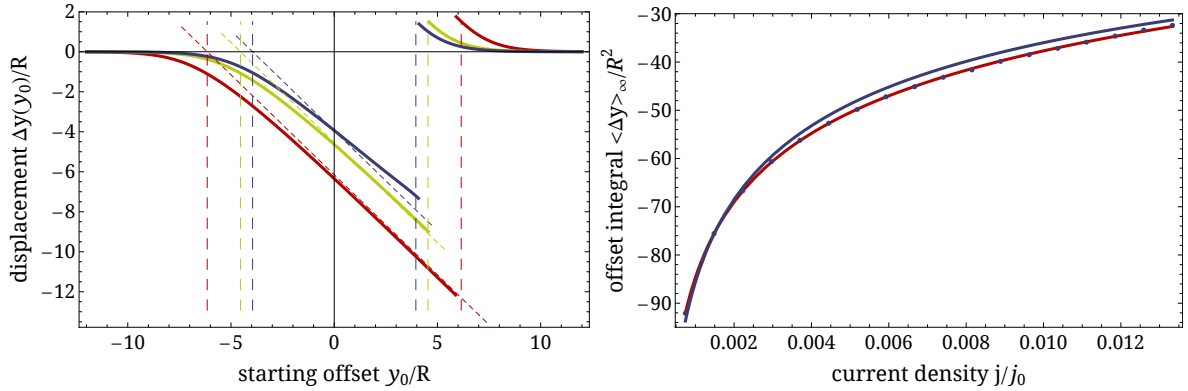

Figure 3.23: Left: displacements $\Delta y(y_0)$ plotted as a function of initial offsets y_0. Comparison of numerical data (solid lines) to the analytic linear assumption $\Delta y_{\text{fit}}(y_0) = -(r_{\text{FP}} + y_0)$ (dashed line). Vertical dashed lines mark the assumed region of validity for the analytic solution $y_0 \in [-r_{\text{FP}}, r_{\text{FP}}]$. Parameters are $\zeta = 1$, $\alpha = \beta = 0.4$ and $j = 0.0015 j_0$ (red), $j = 0.0075 j_0$ (green) and $j = 0.0133 j_0$ (blue). Right: offset integrals calculated numerically (blue dots), analytically (blue) and a logarithmic plus polynomial fit (red).

which also fulfilles $r_{\text{FP}} > 0$ as the current density is sufficiently small.
From our previous considerations about the upper semidefinite fixed point and the offset integral we assume that this distance r_{FP} exactly gives us the region above and below the vacancy in which all trajectories are guided down below the vacancy to a joint final trajectory. We thus assume that we can write:

$$\langle \Delta y \rangle_\infty = \int_{-\infty}^{\infty} \Delta y(y_0)\, \mathrm{d}y_0 \approx \int_{-r_{\text{FP}}}^{r_{\text{FP}}} \Delta y(y_0)\, \mathrm{d}y_0 \approx \int_{0}^{2r_{\text{FP}}} -y_0\, \mathrm{d}y_0 = 2r_{\text{FP}}^2 \tag{3.55}$$

with r_{FP} being logarithmic dependent on the current density as it is given in equation 3.54.
So far we used the crude assumptions that only the trajectories starting in the interval $y_0 \in [-r_{\text{FP}}, r_{\text{FP}}]$ contribute to the offset integral and that they all are guided to the same final trajectory at the lower end of the interval. If we compare these assumption to the data gained numerically, compare figure 3.23, we find that even for larger current densities the assumptions are good ones. The numerical data was evaluated by iterating the Thiele equation starting from different positions. The starting positions were chosen in sufficient distance to the vacancy, here 40 lattice units, and the iteration was performed until the same distance was reached at the other side of the vacancy. The initial offsets were chosen in the same regime, $y_0 \in [-40a, 40a]$, in steps of $\Delta y_0 = 0.1a$, $a = 0.3R$, to guarantee a sufficient resolution. For the comparison to the analytic solution the prefactor of the exponential potential approximation V_0 was determined by fitting it to the numerical data, compare section 2.4.5.
With the numerical data for many different current densities below the first critical current density we can now also numerically calculate the offset integral. The results are shown in figure 3.23. Here we also see that the analytic solution again fits very well the numerical data. Further improvement can be done by adding a polynomial fit function to the logarithmic fit. However, the number of fitting parameters then does not allow to interpret the result in a physically reasonable sense and therefore here is not discussed any further.
Summarizing, with this result for the offset integral and the previous analysis we can predict the average total displacement $\langle \Delta Y \rangle$ of a skyrmion when passing through a system of given

macroscopic extension L, see equation 3.50. This already is sufficient to calculate an estimate for the resulting Hall angle, which is the angle between the direction of the applied current density and the resulting direction of the skyrmion flow. The Hall angle therefore is given by

$$\phi_{\text{Hall}} = \tan\left(\frac{\langle \Delta Y \rangle}{L}\right) = \tan\left(n\langle \Delta y \rangle_\infty\right) \approx n\langle \Delta y \rangle_\infty \tag{3.56}$$

which results from simple geometric arguments comparing the direction of the average skyrmion flow with and without the vacancy.

3.1.2. The Skyrmion Hall Effect in the Free Phase

Up to this point we have only considered current densities in the repulsive phase. Except for the analytic approach to the offset integral all the definitions and formulas are also valid in the free phase. In this phase the skyrmion can freely move and never gets pinned but nevertheless is influenced by the vacancy.
Repeating the numerical evaluation from the repulsive phase we obtain the displacement function also for the free phase, see figure 3.24. What we find is that the displacement function has

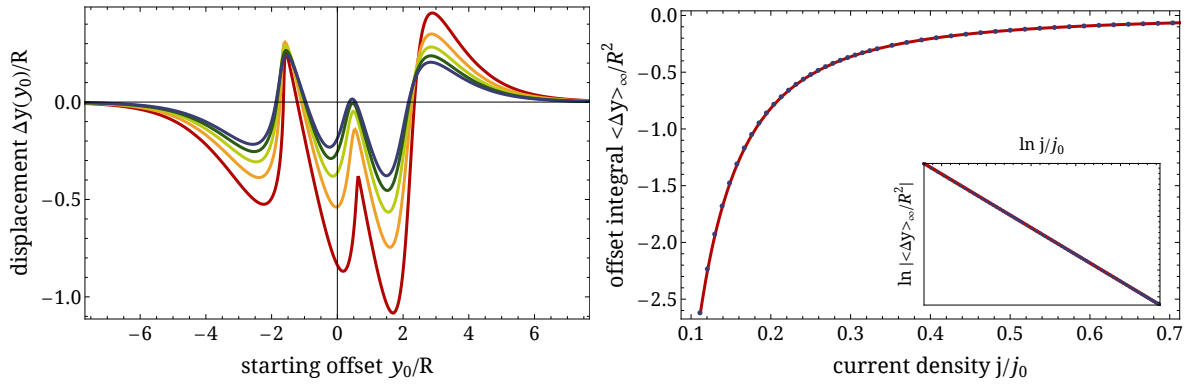

Figure 3.24: Left: displacements $\Delta y(y_0)$ (numerical data) plotted as a function of initial offsets y_0. Parameters are $\zeta = 1$, $\alpha = \beta = 0.4$ and $j = 0.11 j_0$ (red) to $j = 0.26 j_0$ (blue) in equidistant steps. Right: offset integrals as a function of the current density. Comparison of numerical data (blue dots) and perturbative solution $\langle \Delta y \rangle_\infty^{\text{PT}\ 2}(j) = -0.0327\,(j/j_0)^{-2}\,R^2$ (red line). The inset shows the same graph on a log-log-scale.

three peaks of maximal displacement from the initial offset. These three peaks result from the scattering of the skyrmion with the three effective potential maxima in this phase which can be understood as coming from the projection of the potential onto the axis perpendicular to the current density. However, in this phase the displacement is about one order of magnitude smaller than in the repulsive phase, compare figure 3.23. The resulting Hall effect therefore will be much smaller compared to repulsive phase.
Nevertheless we can calculate the offset integral in the free phase numerically by iterating the trajectories as in the previous section. We find that in the free phase also is a net flux below the vacancy, just as in the repulsive phase but much weaker. The resulting offset integral in the free phase is shown in figure 3.24.
To find an analytic approximation to this problem we perform a perturbative ansatz to the offset integral. We assume to have a current density much larger than the potential contribution to

the force which is a reasonable assumption being in the free phase. The exact calculation is long and therefore is presented in the appendix, see A.2. However, the final result for the offset integral using second order perturbation theory for small influences of the potential force is

$$\langle \Delta y \rangle_{\infty}^{\mathrm{PT}\,2} = \frac{2\pi \mathcal{G}\mathcal{D}}{j^2\gamma^4} \int_0^{\infty} \mathrm{d}r\, r V'^{\,2}(r) \tag{3.57}$$

with $\mathcal{D}$ the dissipative force constant linear in the damping parameter α, $\mathcal{G} = -4\pi$ the gyrocoupling constant, $\gamma^2 = \mathcal{D}^2 + \mathcal{G}^2$, $V(r)$ the potential of the vacancy and the current density j. The integral in this expression has to be calculated numerically which yields $\int_0^{\infty} rV'^2(r)\mathrm{d}r \approx -0.234V_0$ for $\zeta = 1$. This perturbative result of second order is also shown in figure 3.24. As it matches the numerical data perfectly another polynomial fit can be seen redundant.

As the Hall effect here, in the free phase, is very small, the approximation for the Hall angle from equation 3.56 certainly holds here:

$$\phi_{\mathrm{Hall}} \approx n \langle \Delta y \rangle_{\infty} \tag{3.58}$$

with n the density of vacancies and the offset integral $\langle \Delta y \rangle_{\infty}$ as shown in figure 3.24. Note that in contrast to the Hall effect in the repulsive phase the offset integral and therefore the Hall effect in the free phase to second order depends almost linear on the dissipation constant $\mathcal{D}$. In the repulsive phase the only dependence is implicitly included in the factor γ which depends on both $\mathcal{D}$ and $\mathcal{G}$ with $\mathcal{D} \ll |\mathcal{G}|$. Hence the Hall effect in the free phase for small damping depends linear on the dissipation constant $\mathcal{D}$ and thus also on the damping parameter α.

Finally it is shown a comparison of offset integrals and therefore the strength of the Hall effects in the free and repulsive phase, see figure 3.25. As in the capturing phase after a certain runtime either all skyrmions are pinned or the interaction between pinned and free skyrmions plays a role there is no Hall effect shown in this case.

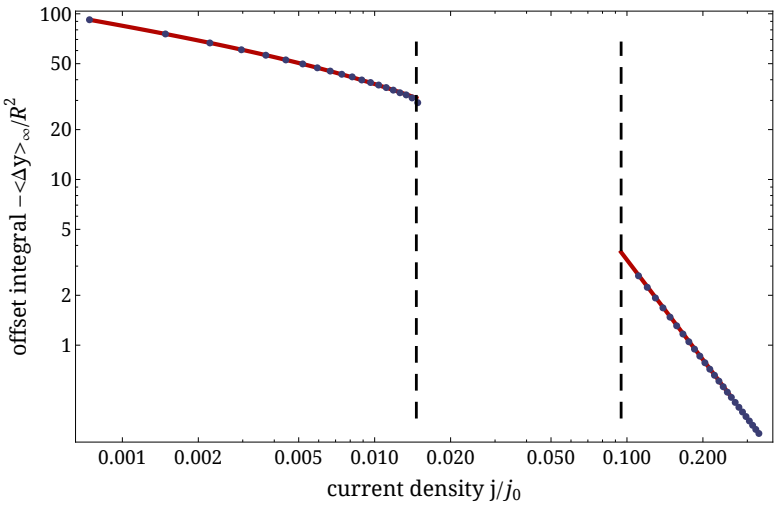

Figure 3.25: Log-log-plot of offset integrals in all phases (numerical data as blue dots, fit functions and perturbative solution red) as a function of the current density. The capturing phase is marked by vertical dashed lines.

3.2. The Speed-Up at a Vacancy

In this section the speed-up generated by a vacancy is analyzed. To motivate this effect we refer to the previous chapter on the Hall effect. In chapter 3 it has been shown that the Hall effect which results from the presence of a vacancy always creates a net current pushing the skyrmions on trajectories below the vacancy, providing that the current density points to the right. If we go back to the simplified Thiele equation, equation 2.26, and look for the version where the force is separated into radial and angular components we find two contributions: the dissipative part pushes the skyrmion on radial trajectories either towards the vacancy or away from it and the magnus related term lets the skyrmion move on circular trajectories around the vacancy. The direction of circular motion in the second part is dependent on both the sign of the derivative of the potential $V'(r)$ and the sign of the gyrocoupling constant $\mathcal{G}$ which in all cases discussed in this thesis is negative. This circular component in not only the origin of the Hall effect guiding the skyrmion below the vacancy, it also changes the absolute value of the velocity locally. Whether the addition of both components increases or decreases the total velocity depends on the precise position. Due to the negative gyrocoupling $\mathcal{G} < 0$ the velocity contributions from the current density and the magnus force add up below the vacancy, whereas above the vacancy it is the opposite case. Additionally the same arguments apply also for the dissipative force part. The resulting total velocity is shown in figure 3.26. As the dissipative term is smaller than the magnus term, $\mathcal{D} < \mathcal{G}$, but still comparable, the highest velocity is not reached below the vacancy. It is rather that due to this term the whole symmetric velocity field is turned such that the new symmetry axis is not the one perpendicular to the current density but the axis on which are the fixed points of the Thiele equation, see equation 2.30.

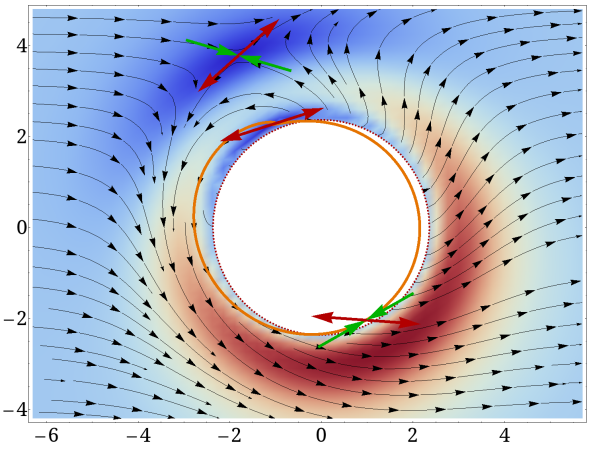

Figure 3.26: Trajectories of the single skyrmion with fixed points, separatrix and color-coded velocity from blue (slow) to red (fast), compare figure 2.15. With $\zeta = 1$, $\alpha = 0.4$, $j = 0.011 j_0$.

Summarizing, due to the magnus force the skyrmions that are influenced by the Hall effect are accelerated. At least in the repulsive phase one expects the skyrmions to be accelerated also in total. This effect we refer to as the *speed-up* at a vacancy.

To get a first impression of this effect we use the numerical data from the Hall effect calculation. There we iteratively solved the Thiele equation of motion for a set of starting points on the line perpendicular to the current density. The iteration started at a sufficiently large distance to the vacancy in the direction of the current density and ended at a sufficiently large distance in this direction. In total, the skyrmion then has moved the fixed distance L along the axis which is defined by the current density in the time $t(L)$. The time it would have needed to overcome this distance in the clean system is given by $t_0(L) = {}^{L}/_{j}$. Further we define the difference of these two times $\Delta t = t - t_0$. Here we omit the dependence on L because for large $L \gg R$ the skyrmion is far away from the vacancy and not influenced by it anymore. Hence any further

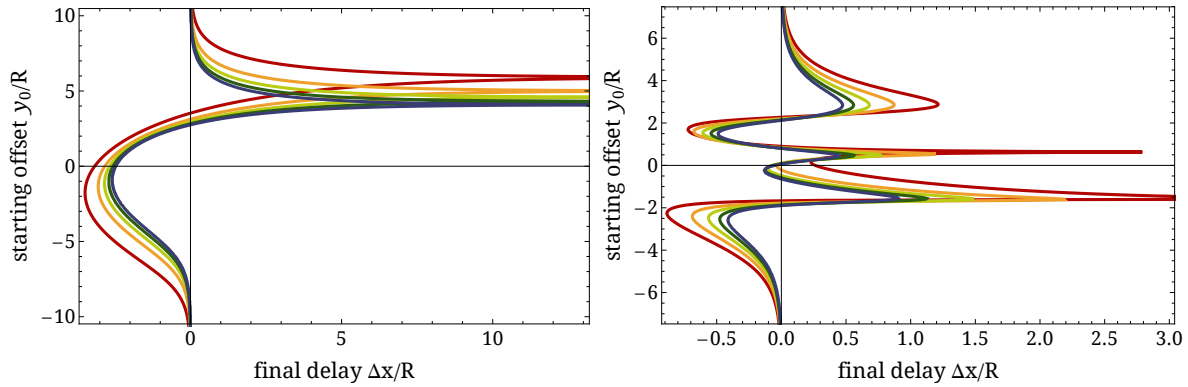

Figure 3.27: Both: delays $\Delta x(y_0)$ (numerical data) plotted as a function of initial offsets y_0. Parameters are $\zeta = 1$, $\alpha = 0.4$. Left: $j = 0.00148 j_0$ (red) to $j = 0.0133 j_0$ (blue). Right: $j = 0.11 j_0$ (red) to $j = 0.26 j_0$ (blue). All in equidistant steps. Note the axes are switched to match their real-space analogon.

contribution to the time $t(L)$ is the same as to the time $t_0(L)$ in the clean system. If only one vacancy has been passed, the time difference Δt therefore is the *time delay* at a vacancy. For the pronounced speed-up in the repulsive phase this quantity should turn out to be negative. Further, if we compared the distance in this direction at equal times, then for long enough timescales the final delay in distance is exactly given by

$$\Delta x = j\Delta t = j(t - t_0) \tag{3.59}$$

along the direction of the current density. This means that if the skyrmion in the clean case needed Δt less time to pass the distance, then it can move at velocity j for the remaining time Δt, which the skyrmion with the vacancy can not. Note that due to the Hall effect the skyrmion with the vacancy has passed an even longer effective distance, which is neglected here. However, the final offset defined this way is shown in figure 3.27.
From the figures we see that dependent on the starting offset the delay can be positive or negative. In both phases, the repulsive and the free phase, both cases are possible. This means that in both phases, dependent on the starting point relative to the vacancy, the skyrmion in total was slowed down (positive delay) or was speeded up (negative delay). Again, as for the Hall effect, the speed-up in the repulsive phase is much stronger as in the free phase. Also in analogy to the Hall effect, in the repulsive phase we have only one peak appearing in our result, whereas in the free phase we have three peaks. Again these result from the three effective maxima of the potential.
However, to describe the *average* speed-up which is important for the macroscopics, we repeat the primary analysis of the Hall effect, see section 3.1.1. In analogy to this discussion we also define the *delay integral* $\langle \Delta x \rangle_\infty$ which relates the total delay ΔX to the system size L and the density of vacancies n

$$\langle \Delta X \rangle = N \langle \Delta x \rangle_\xi = L\xi^{-2} \int_{-\infty}^{\infty} \Delta x(y_0) \mathrm{d}y_0 = Ln \langle \Delta x \rangle_\infty. \tag{3.60}$$

The delay integral we can calculate numerically. The resulting functions are shown in figure 3.28 for both phases below and above the capturing phase. Additionally, in the repulsive

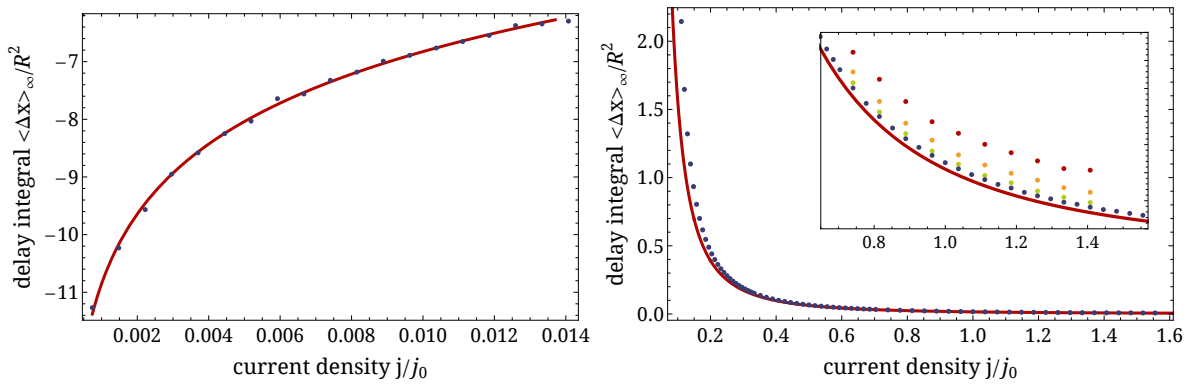

Figure 3.28: Delay integrals $\langle \Delta x \rangle_\infty$ (blue dots) in the repulsive phase (left) and the free phase (right) determined numerically. Parameters are $\zeta = 1$ and $\alpha = 0.4$. Left: with fit function $\langle \Delta x \rangle_\infty^{\text{fit}}(j) = -1.81R^2 - 1.46 \ln[j/j_0]\, R^2$ (red line). Right: with second order perturbative solution $\langle \Delta x \rangle_\infty^{\text{PT }2}(j) \approx \frac{\mathcal{D}}{\mathcal{G}} \langle \Delta y \rangle_\infty^{\text{PT }2}(j)$ (red line). Inset additionally shows numerical results for 2 (green), 4 (yellow) and 8 (red) times the chosen time step-width (blue) of $dt = 5 \cdot 10^{-4} j^{-1}$.

phase, the figure shows a fit function. According to the logarithmic result from the Hall effect, a logarithmic fit function was chosen. The matching of the fit and the data is almost perfect. The result in the free phase can be treated in more detail: we can apply a perturbative ansatz in this phase as we did for the Hall effect, see appendix A.3. By the same arguments as in the Hall effect the first order contribution vanishes and only terms of at least second order in $\mathcal{O}(j^{-2})$ contribute. As shown in the appendix A.3, the leading order contribution is related to the offset integral, see equation 3.57, in the Hall effect as

$$\langle \Delta x \rangle_\infty^{\text{PT }2} = \frac{\mathcal{D}}{\mathcal{G}} \langle \Delta y \rangle_\infty^{\text{PT }2} = \frac{2\pi \mathcal{D}^2}{j^2 \gamma^4} \int_0^\infty \mathrm{d}r\, r V'^{\,2}(r). \tag{3.61}$$

This perturbative approximation is assumed to describe well the behaviour of the delay integral for large current densities. The comparison to the numerical data shown in figure 3.28 shows that the approximation does not describe the delay integral close to the phase transition but becomes better for larger current densities. However, even though the perturbative approximation becomes better for larger current densities, it seems that it can only describe the numerical data up to a constant offset. To better show this offset, we included an inset in figure 3.28 that shows the behaviour for large current densities on a more useful scale to really be able to compare the data. Here also the results for lower step-widths in the iteration algorithm were included. These show that when lowering the step-width in the iteration the delay intergral converges towards the analytically predicted perturbative solution. Unfortunately, the iteration takes too much time that one could use even smaller step-widths for better results than already shown in the figure. Although the offset between the results for the smallest step-width and the approximation seems very small, it will lead to problems in the following section.
Summarizing, is remarkable that in the repulsive phase there is a speed-up due to the vacancy. The qualitative considerations according to figure 3.26 therefore seem to make sense. This result is in contrast to the behaviour in the free phase. Here, on average, the skyrmion is slowed down by the vacancy as we are used to in the classical picture of friction. Nevertheless, even stronger than in the Hall effect, this effect is supposed to vanish in leading order quadratic in the damping α.

3.3. The Effective Damping Parameters

So far, in this section we have considered skyrmions that are driven by a current density j/j_0 with equal damping parameters $\alpha = \beta = 0.4$. Due to the equal damping parameters the velocity of the skyrmions without a vacancy is equal to the current density. By the presence of vacancies this relation changes as the skyrmions obey a Hall effect, i.e. a velocity perpendicular to the current density. Furthermore the skyrmion is speeded up in the repulsive phase and slowed down in the free phase. Consequently, in a large system with a finite density of vacancies, the effective damping parameters α' and β' are different from the original damping parameters.

$$\alpha = \beta \neq \alpha' \neq \beta' \tag{3.62}$$

First we assume a system of size L and a current density j. Then the time a skyrmion needs to pass the system is $T = {}^{L}/_{j}$. The delay generates an average total displacement $\langle \Delta X \rangle$ opposite to the direction of the current density, see equation 3.60. Consequently the total distance L is shortened to $L - \langle \Delta X \rangle$ and the velocity in the direction of the current density is reduced to

$$v_{\parallel} = \frac{L - \langle \Delta X \rangle}{T} = j \left(1 - \frac{\langle \Delta X \rangle}{L} \right) = j \left(1 - n \langle \Delta x \rangle_{\infty} \right). \tag{3.63}$$

Further the Hall effect generates a net velocity of the skyrmions in the direction perpendicular to the current density

$$v_{\perp} = \frac{\langle \Delta Y \rangle}{T} = j \frac{\langle \Delta Y \rangle}{L} = jn \langle \Delta y \rangle_{\infty} \tag{3.64}$$

compare equation 3.50. Note that both total displacements $\langle \Delta X \rangle$ and $\langle \Delta Y \rangle$ depend on the damping α at which they were determined.
Now we determine an expression for the effective damping parameters. We use that the velocities $v_{\parallel}$ and $v_{\perp}$ depend on the damping parameters as given in equations 1.8 and 1.9. To simplify expressions we define the rescaled velocities in units of the current density, $u_{\parallel} = {}^{v_{\parallel}}/_{j}$ and $u_{\perp} = {}^{v_{\perp}}/_{j}$. The equations for the velocity then according to 1.8 and 1.9 become

$$u_{\parallel} = \frac{\beta}{\alpha} + \frac{\alpha - \beta}{\alpha^3 \left(\frac{D}{\mathcal{G}} \right)^2 + \alpha} \tag{3.65}$$

$$u_{\perp} = \frac{(\alpha - \beta) \left(\frac{D}{\mathcal{G}} \right)}{\alpha^2 \left(\frac{D}{\mathcal{G}} \right)^2 + 1} \tag{3.66}$$

where $\mathcal{G} = -4\pi$ is the gyrocoupling constant and $D = {}^{\mathcal{D}}/_{\alpha}$ is the dampingless dissipative constant. Note that in contrast to $\mathcal{D}$ in the Thiele equation 2.20 the dissipative constant D here does not have the damping constant included. From these equations we see indeed that for equal damping parameters $\alpha = \beta$ the velocity in value and direction is precisely given by the current density.
However, for the presence of vacancies we have finite $u_{\parallel}$ and $u_{\perp}$. Therefore we can use these equations to determine the effective damping parameters $\alpha \to \alpha'$ and $\beta \to \beta'$. It is an easy exercise to solve the equations 3.65 and 3.66 for α' and β' and so we recover

$$\alpha' = \frac{\mathcal{G}}{D} \frac{1 - u_{\parallel}}{u_{\perp}} \tag{3.67}$$

$$\beta' = \alpha' \left(u_{\parallel} - \frac{u_{\perp}^2}{1 - u_{\parallel}} \right). \tag{3.68}$$

To simplify these expressions we can use the previous considerations in equations 3.63 and 3.64. What we recover are the effective damping parameters in dependence of the delay integral $\langle \Delta x \rangle_\infty$, the offset integral $\langle \Delta y \rangle_\infty$ and the density of vacancies n:

$$\alpha' = \frac{\mathcal{G}}{D} \frac{\langle \Delta x \rangle_\infty}{\langle \Delta y \rangle_\infty} \tag{3.69}$$

$$\beta' = \alpha' \left(1 - n \frac{\langle \Delta x \rangle_\infty^2 + \langle \Delta y \rangle_\infty^2}{\langle \Delta x \rangle_\infty} \right) = \alpha' \left(1 - n\kappa \right). \tag{3.70}$$

Concerning this result, two properties are espacially remarkable: one is that the effective damping α' does not depend on the density of vacancies, at least not in the considered limit of a very low density. Secondly one might conclude that the effective damping parameters do not depend on the initial damping α. This behaviour would not be physical and in fact the dependence on α is implicitly given in the delay and offset integrals which depend on the damping α. These two properties result from the special initial choice $\alpha = \beta$. This choice can always be achieved by a propper rescaling and reorientating of the current density, see section 1.3.
If we however assume different damping parameters $\alpha \neq \beta$ then in the clean system the relative velocities are given by $u_\parallel$ and $u_\perp$ as in equations 3.65 and 3.66. The effective relative velocities $u'_\parallel$ and $u'_\perp$ then are given as

$$u'_\parallel = u_\parallel - n \langle \Delta x \rangle_\infty \tag{3.71}$$

$$u'_\perp = u_\perp + n \langle \Delta y \rangle_\infty. \tag{3.72}$$

We can thus obtain the final expression for the effective damping parameters in the case $\alpha \neq \beta$ by the replacement

$$\langle \Delta x \rangle_\infty \to \frac{1}{n}(1 - u_\parallel) + \langle \Delta x \rangle_\infty \tag{3.73}$$

$$\langle \Delta y \rangle_\infty \to \frac{1}{n} u_\perp + \langle \Delta y \rangle_\infty. \tag{3.74}$$

To test whether this replacement indeed yields the correct results we examplary consider the effective damping α' in the limit for small densities $n \to 0$. With the formula for equal damping parameters, equation 3.69, this limit is ill defined. However, with the replacements 3.73 and 3.73 we recover

$$\begin{aligned}
\alpha' &= \frac{\mathcal{G}}{D} \frac{\langle \Delta x \rangle_\infty}{\langle \Delta y \rangle_\infty} \\
&\xrightarrow{\alpha \neq \beta} \frac{\mathcal{G}}{D} \frac{1 - u_\parallel + n \langle \Delta x \rangle_\infty}{u_\perp + n \langle \Delta y \rangle_\infty} \\
&= \frac{\mathcal{G}}{D} \frac{1 - u_\parallel}{u_\perp} + n \frac{u_\perp \langle \Delta x \rangle_\infty - (1 - u_\parallel) \langle \Delta y \rangle_\infty}{u_\perp^2} + \mathcal{O}(n^2) \\
&\xrightarrow{n \to 0} \frac{\mathcal{G}}{D} \frac{1 - u_\parallel}{u_\perp} \\
&\overset{3.67}{=} \alpha
\end{aligned} \tag{3.75}$$

which is exactly the result that is expected. Here made use of the definition of the delay integral and the offset integral, which are defined relative to the current density and not to the velocity in the pure system. Hence the result is also applicable for systems with $\alpha \neq \beta$.

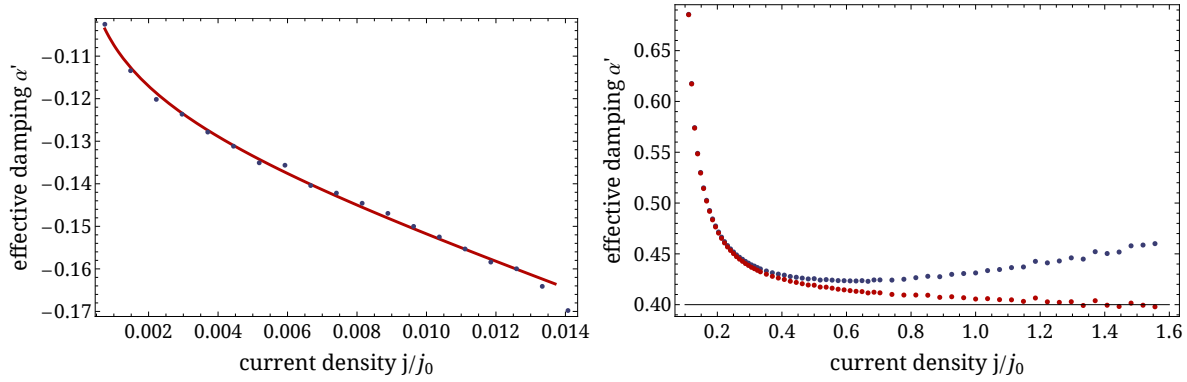

Figure 3.29: Effective damping parameter α' (blue dots) in the repulsive phase (left) and the free phase (right) determined numerically. Left: red line is the result from the fit functions obtained from figures 3.23 and 3.28. Right: red dots show α' after subtracting numerical offset from $\langle \Delta x \rangle_\infty$. The solid black line at $\alpha' = 0.4$ marks the expected large-current limit. Both: parameters are $\zeta = 1$ and $\alpha = 0.4$.

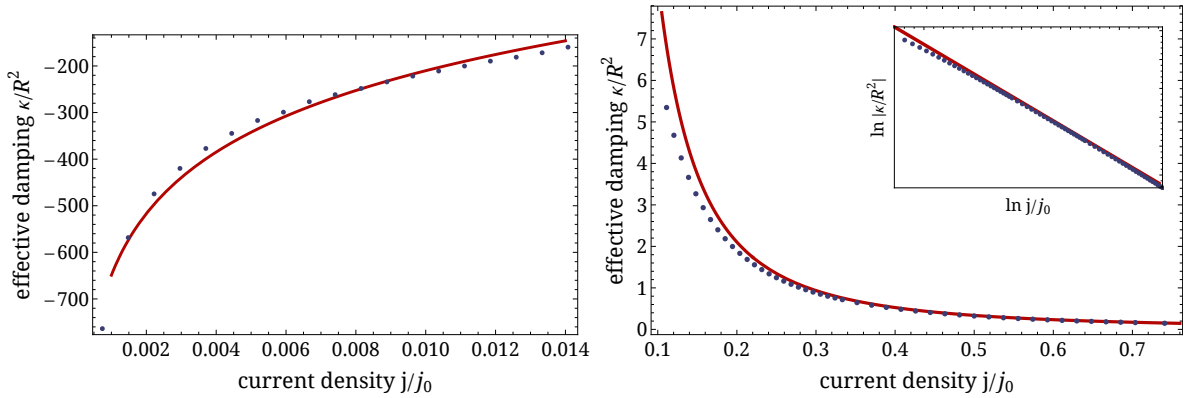

Figure 3.30: Effective parameter κ (blue dots) determined numerically in the repulsive phase (left) and the free phase (right). Left: red line is a logarithmic fit function. Right: red line is κ calculated from the second order perturbation theory results for the offset and delay integrals, $\kappa = \left({}^{\mathcal{G}}/_{\mathcal{D}} + {}^{\mathcal{D}}/_{\mathcal{G}}\right) \langle \Delta y \rangle_\infty \approx$ with $\langle \Delta y \rangle_\infty \approx$ as in equation 3.57. The inset shows a log-log-plot on a larger region of the current density. Both: parameters are $\zeta = 1$ and $\alpha = 0.4$.

Another interesting limiting case that can be discussed analytically is that for large current density. In this case the leading order contributions of the perturbative ansatz, see appendix A.3, become the only relevant ones. For the regarded case $\alpha = \beta$ then the limiting case for α' becomes

$$\begin{aligned} \alpha' &= \frac{\mathcal{G}}{D} \frac{\langle \Delta x \rangle_\infty}{\langle \Delta y \rangle_\infty} \\ &\xrightarrow{j \gg j_c} \frac{\mathcal{G}}{D} \frac{\langle \Delta x \rangle_\infty^{\mathrm{PT}\ 2}}{\langle \Delta y \rangle_\infty^{\mathrm{PT}\ 2}} \\ &= \frac{\mathcal{G}}{D} \frac{\mathcal{D}}{\mathcal{G}} = \alpha. \end{aligned} \tag{3.76}$$

This result is also what one would expect physically as for large current densities the force by the vacancy as a perturbation becomes very small, until in the limit of very large current

densities it asymptotically has no impact on the motion anymore.
In the previous sections on the Hall effect and the speed-up we have already produced all the data required such that the coefficient α' and κ for $\alpha = \beta = 0.4$ can immediately be calculated. The results are shown in figures 3.29 and 3.30. What we obtain is an almost linear behaviour in the repulsive phase, that is for very low current densities, with a negative damping α'. The negative effective damping is a result of the speed-up at the vacancy in this phase, see section 3.2. In the repulsive phase, that is for large current densities, the situation is different. Here the effective damping α' close to the capturing phase starts at a very large value. If we expect a collective pinning in the capturing phase then α' really is supposed to diverge at the phase transition. For much larger current densities then the critical current density, the effects of the vacancy on the motion should become redundant and hence the for large current densities $\alpha' \to \alpha$. This results we also showed within the perturbative ansatz. However, the numerical data does not fit to this expected result. After the effective damping seems to converge at current densities $j \approx 0.5 j_0$, it grows up again for even larger current densities. This late revival can be shown to occur as a consequence of the problem with the convergence when calculating the delay integral, see section 3.2. There it turned out that the numerical data describes the perturbative approximation up to an approximately constant offset which disappears with increasing step-width. It we in a lowest order approximation take the offset to be really constant and subtract it, we recover the red data points in figure 3.29. The difference between these two data sets gives an impression for the error estimate for this method. Though this shows that the regime of large current density can not be described by the numerics, the damping α' can be well described close to the capturing phase.
Also the coefficient κ, which relates the damping β' to the damping α' and the density of vacancies n, can be calculated from the previous data. The results are shown in figure 3.30. Here it turns out that in the repulsive phase the effective damping β' is a multiple of α'. The behaviour can only very approximate be described by a logarithmic function. In the repulsive phase it comes in handy that for large current densities the delay integral is by a factor $\frac{\mathcal{D}}{|\mathcal{G}|} \ll 1$ smaller than the offset integral. The last one thus contributes much stronger to the coefficient κ and as the offset integral is almost free from corrections of higher order than the second order perturbative contribution, we can describe κ very well by the perturbative approximations.

4. The Vacancy Wall in Two Dimensions

In this thesis, so far, only point-like vacancies in chapters 2 and 3 have been considered. These point-like vacancies gained the most attention as they can be described in an almost perfect approximation by the Thiele equation, see section 2.5. The basic idea, to measure a potential and apply it to the Thiele equation could in principle also be transfered to other types of vacancies.

In this chapter the Thiele equation is shown to also work well for one-dimensional defects. The example discussed here is the straight vacant wall, see figure 4.31. As we only consider nearest neighbor interaction in the lattice model of the full micromagnetic system, this setup is completely analogous to a skyrmion at the end of a wire or domain. It therefore has already been discussed [33] but not with respect to the Thiele equation.

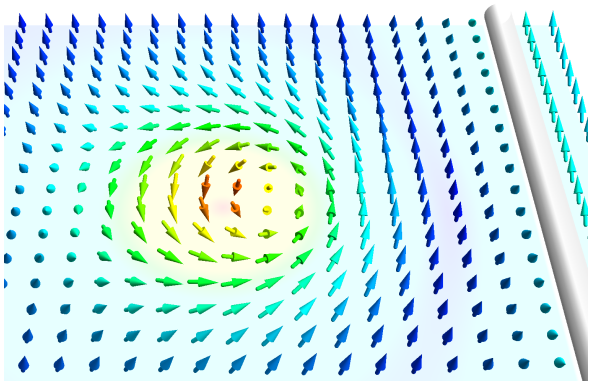

Figure 4.31: Skyrmion at a vacancy wall. Result of micromagnetic LLG simulation for $D = 0.3J$, $B = 0.09J$, $\mathbf{j} = 0.01J\mathbf{e}_x$, $a = 1$.

To really gain quantitative results from the Thiele equation 1.11 an expression for the force term is needed. In section 2.4 we introduced the local and global update algorithms to determine the potential of the point-vacancy. These methods are not restricted to point-like vacancies, therefore we can use them to determine the potential of the vacancy wall numerically. However, it turns out that these methods in this case do *not* yield good results. To show this we compare the potential calculated with the global update algorithm, which is the slower but more precise algorithm, to the energy of the system while running the full micromagnetic LLG simulation, compare section 2.1. For the second method we simulate the single skyrmion approaching the vacancy wall at a constant current density and meanwhile track both the distance of the skyrmion to the wall and the energy of the system, defined as the value of the free energy functional for the specific configuration of magnetic moments. What we recover thus is the energy difference as a function of the spatial distance, neglecting the contribution of the current density itself. This approach includes possible influences of the current density on the shape of the skyrmion and has the disadvantage that it can not be used on all distances but only where the skyrmion gets driven by the current. A comparison of the results

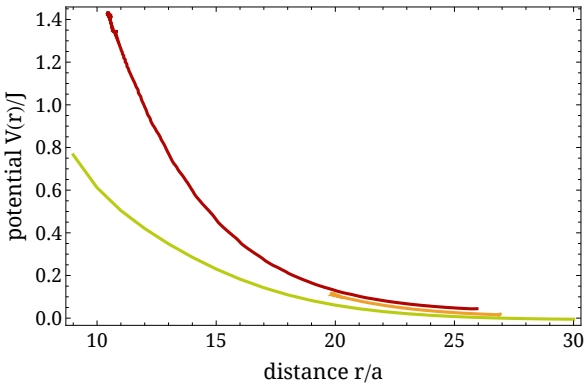

Figure 4.32: Potentials of the vacancy wall for $D = 0.3J$, $B = 0.09J$, $a = 1$ in global update algorithm (green) and tracking approach at $j = 0.001J$ (yellow) and $j = 0.01J$ (red).

from the global update algorithm and the tracking results for two different current densities is shown in figure 4.32. There also the disadvantage of the tracking method can be seen: its potential curves are accessible only on large distances to the wall. The minimal distance achievable is the equilibrium distance to which the skyrmion is pushed by the current density. As an example figure 4.31 shows the magnetization after a sufficiently long time. The therefore distance to the wall which is approximately 10.5 sites and matches to the minimal distance given in the potential graph figure 4.32.
The comparison of the methods with and without an applied current density in particular shows that the potential is *not* independent of the current density. For larger distances this might not cause any problems but on the more interesting scales, which are small distances to the wall and therefore larger current densities, the difference in the potential is approximately a factor of two. Hence in this section we use a potential which is dependent on both the distance to the wall and the applied current density. By convention we further assume, as shown in the figure 4.31, that the vacancy wall is orientated along the y-axis. A rotation of the system such that this assumption holds is always possible if we do not assume a specific direction for the current. Further we note that the current density is assumed to be constant such that we drop its explicit dependency. Thus the force $\mathbf{F}(\mathbf{r})$ only acts in x-direction and we can write it as

$$\mathbf{F}(\mathbf{r}) = F(x)\mathbf{e}_\mathrm{x} = -V'(x)\mathbf{e}_\mathrm{x}. \tag{4.77}$$

For the potential $V(r)$ of the point-like vacancy we could show in section 2.4.5 an asymptotic exponential behaviour. In the setup considered here the skyrmion does not approach the vacancy wall closer than approximately $10.5a = 10.5\frac{B}{D}R \approx 3R$. This we can assume to be large enough to apply the same arguments as in section 2.4.5 again such that we can assume the potential to decay exponentially as a function of distance x to the wall:

$$V(x) = a\,\mathrm{e}^{-\frac{|x|}{\xi}} \tag{4.78}$$

where ξ is a length and a an energy scale. Both still are to be determined. With these assumptions the Thiele equation 1.11 is exact solvable for any direction of the current density $\mathbf{j} = (j_\mathrm{x}, j_\mathrm{y})^\mathrm{T}$:

$$\mathbf{r}(t) = \mathbf{r}_0 + (t-t_0)\mathbf{j} - \frac{\xi}{\mathcal{D}}\ln\left[1 + \frac{a\mathcal{D}}{j_\mathrm{x}\gamma^2\xi}\mathrm{e}^{\frac{x_0}{\xi}}\left(\mathrm{e}^{\frac{j_\mathrm{x}}{\xi}(t-t_0)} - 1\right)\right]\begin{pmatrix}\mathcal{D}\\ -\mathcal{G}\end{pmatrix} \tag{4.79}$$

for $x, x_0 < 0$ with the starting point $\mathbf{r}_0 = \mathbf{r}(t_0) = (x_0, y_0)^\mathrm{T}$, $\mathcal{G} = -4\pi$ the gyrocoupling constant and $\mathcal{D} \approx 15\alpha$ the dissipation constant, α the damping. The derivation of this result is given in the appendix A.4.
Concerning the long time limit $t \gg t_0$, see appendix A.4, we furthermore obtain for the final distance of the skyrmion to the vacancy wall x_∞ and also the final position parallel to the wall y_∞ as well as the final velocity $\dot{\mathbf{r}}_\infty$:

$$x_\infty = x(t \gg t_0) = -\xi\ln\left[\frac{a\mathcal{D}}{j_\mathrm{x}\gamma^2\xi}\right] \tag{4.80}$$

$$y_\infty = y(t \gg t_0) = y_0 + \frac{\mathcal{G}}{\mathcal{D}}(x_0 - x_\infty) + (t-t_0)\left(j_y + \frac{\mathcal{G}}{\mathcal{D}}j_x\right) \tag{4.81}$$

$$\dot{\mathbf{r}}_\infty = \dot{\mathbf{r}}(t \gg t_0) = \left(j_y + \frac{\mathcal{G}}{\mathcal{D}}j_x\right)\mathbf{e}_y. \tag{4.82}$$

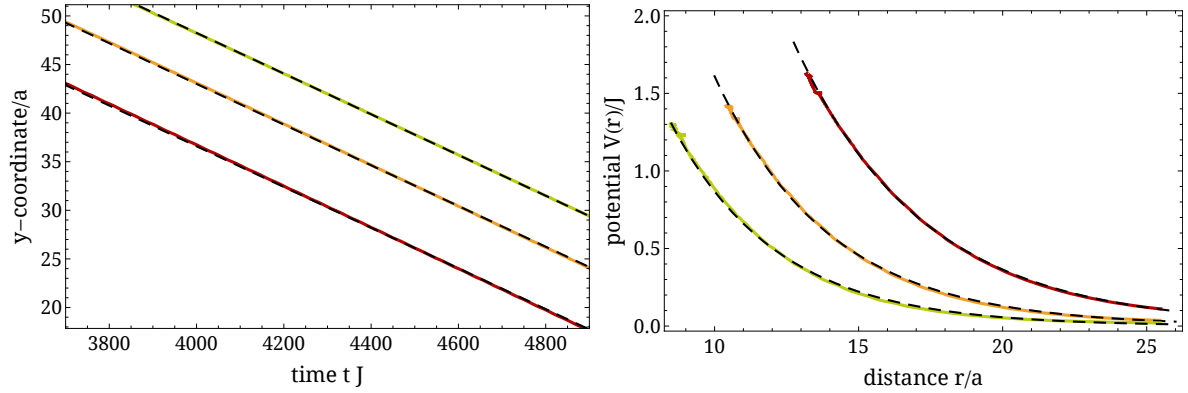

Figure 4.33: Left: skyrmion positions parallel to the wall as a function of time. Right: potential of the vacancy wall as a function of distance. In both plots the coloured lines are obtained from the full micromagnetic LLG simulation for $D = 0.3J$, $B = 0.07J$ (red), $B = 0.09J$ (yellow), $B = 0.11J$ (green), $\alpha = \beta = 0.4$, $j = 0.01J$, $a = 1$. The dashed lines are fits using the analytic results of the exponential ansatz, eq. 4.78.

From these limiting cases we can extract the dependence of the final distance to the wall on the parameters of the potential and the current density as well as the final total velocity which is parallel to the wall only. These two conclusions from the limiting cases are shown to be consistent with the results of the full micromagnetic simulation of the LLG equation. Using the tracking algorithm we obtain the time dependent position of the skyrmion parallel to the wall and can compare it to the prediction of the Thiele equation with the exponential ansatz for the velocity, see equation 4.82. Further we can use the final distance to the wall to eliminate one of the fitting parameters of the potential and we can show that indeed the potential can be perfectly approximated by the exponential ansatz 4.78. Both results are shown in figure 4.33 for various shapes of skyrmions at a current density of $j = 0.01J$. For lower current densities the exponential approximation also works perfectly but the results are not shown here.

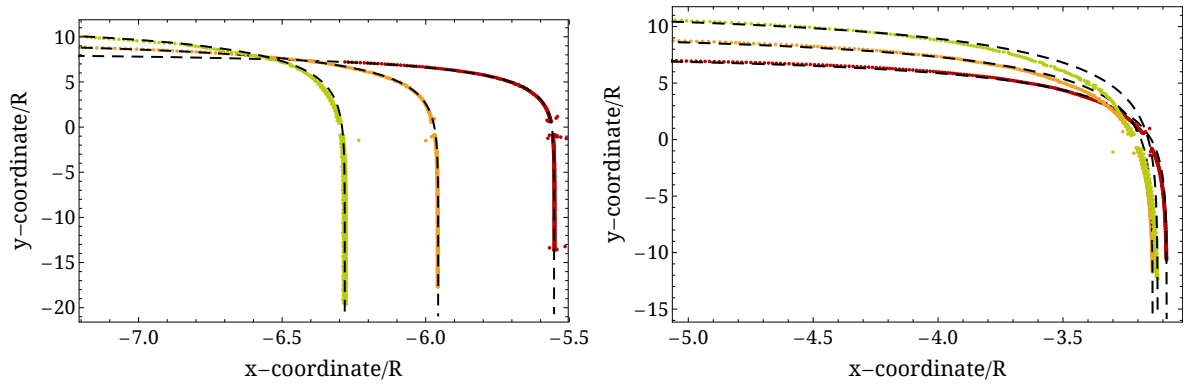

Figure 4.34: Trajectories of a skyrmion near a straight vacancy wall at $x = 0$. In both plots the coloured lines are obtained from the full micromagnetic LLG simulation for $D = 0.3J$, $B = 0.07J$ (red), $B = 0.09J$ (yellow), $B = 0.11J$ (green), $\alpha = \beta = 0.4$, $j = 0.001J$ (left plot), $j = 0.01J$ (right plot), $a = 1$. The dashed lines are obtained using the analytic solution of the exponential ansatz, eq. 4.79, with the parameters of the ansatz gained from the potential fit. The holes in the numerical data result from problems of the tracking algorithm close to the periodic boundary of the simulated grid.

However, using the perfect fit to the potential and the hereby gained parameters a and ξ we can also compare the full trajectories of the skyrmion near the vacancy wall. The comparison of the trajectories gained from the Thiele equation solution with the trajectories of the full micromagnetic LLG simulation are shown in figure 4.34. For smaller current densities, here as an example $j = 0.001J$, the trajectories can be very well described by the Thiele result of the exponential ansatz. On the contrary, for the larger current densities concerned, here $j = 0.01J$, the Thiele ansatz turns out to be unsufficient. Although from a qualitative point of view the trajectories from the full simulation are well reproduced by the exponential ansatz, the exact behaviour can only hardly be described by the Thiele solution. Furthermore small deviations in the parameters of the exponential ansatz already cause large deviations in the trajectory such that a reasonable fitting also is very hard to produce.
For even larger current densities than the ones shown here as examples, it happens that the skyrmion unwinds into the wall. This effect has already been observed previously by other groups [33].
To conclude with this excursion to higher dimensional vacancies, we find that the movement of a skyrmion close to the vacancy can also be well described by the Thiele equation. In contrast to previous cases where we assumed point-like vacancies, this system can be even solved analytically if the assumption of an exponential potential is made. A nicely visible result is that the skyrmion, as soon as it has arrived at its equilibrium distance to the wall, by a factor $\frac{\mathcal{G}}{\mathcal{D}}$ moves faster along the wall if the current points into the wall than if the current is parallel to the wall. A misleading conclusion from this expression might be that for an infinitisemal damping, $\mathcal{D} \to 0$, the skyrmion moves infinitely fast along the wall. This is certainly not true as then it would also move infinitisemally close to the wall, which due to the finite extension of the skyrmion would finally destroy it. However, although the assumption of an exponential potential which is leading to the analytic solution is reasonable and well proven numerically, the solution itself does not completely describe the trajectory of the full micromagnetic simulation at larger current densities. We believe that this results from other effects which occur at these larger current densities as there is as an example the slight squeezing of the skyrmion at the wall which certainly has an impact on the dissipation constant. Furthermore for even slightly larger current densities the skyrmion already gets destroyed, which can not be described by the exponential ansatz or the Thiele equation.

5. Nucleation and Annihilation at a Vacancy in Two Dimensions

As has been shown already by another group [33], it is possible to nucleate skyrmions at defects. According to the authors, the requirements needed to nucleate a skyrmion at a defect are a large enough current density and a sufficiently large defect. Also for the vacancies considered in the previous chapters this effect occurs. An advantage of considering a simple shaped, round vacancy as shown in figure 5.35, which essentially is an enlarged version of the vacancies discussed so far in this thesis, is that they are the more natural type. If one thinks about a possible realization of the setup, the round vacancy is the natural result when preparing a hole in the sample.

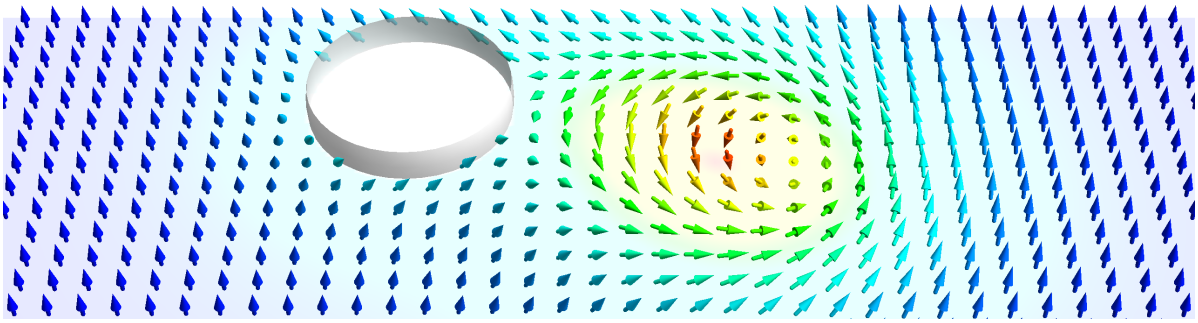

Figure 5.35: Skyrmion created a at vacancy. Result from micromagnetic LLG simulation, see chapter 5, with parameters $D = 0.3J$, $B = 0.09J$, $\alpha = \beta = 0.4$, $\mathbf{j} = 0.2J\mathbf{e}_x$, $a = 1$.

In section 2.1 the full micromagnetic simulation of the Landau-Lifshitz-Gilbert equation 1.3 is explained. This method we use again to show the creation of skyrmions at a vacancy.
First we prepare a ferromagnetic state as the starting point of the simulation. The vacancy, as being a missing atom and hence a missing magnetic moment, we model by setting the magnetization at one site to zero. This is how we constructed vacancies so far in this thesis. However, to create a skyrmion at a defect, the defect needs to provide an edge that has an extension of the order of the radius of the skyrmion. Therefore we extend the vacancy to an extended object by setting the magnetic moment at more than only one site to zero.
The skyrmion radius we defined in section 1.4 given by $R = \frac{D}{B}a$. Here D is the Dzyaloshinskii-Moriya-coupling in the lattice model, B is the magnetic field strength and a is the lattice spacing. In the simulation we use the parameters $D = 0.3J$ and $B = 0.09J$ such that we are in the field polarized phase. A skyrmion in this phase therefore only is a meta-stable groundstate. Due to the choice of parameters the skyrmion radius is approximately $R = 3.3a$. We decide to choose the vacancy radius to be equal to the skyrmion radius, for that we achieve the requirement to have a vacancy radius of the order of the skyrmion radius.
It turns out that the creation of skyrmions at the vacancy is highly sensitive to small disturbancies of the equilibrium order. For real systems that obey temperature or quantum fluctuations this means the possibility to create skyrmions at much lower current densities. Thus, for our numerical setup at zero temperature and no fluctuations it is not sufficient to create a vacancy by removing a region of sites in the simulated layer and then apply a current density. If one does so, due to the Dzyaloshinskii-Moriya interaction the magnetic moments around the vacancy start to twist as can be seen in figure 5.35 on the left of the vacancy. The twisting after the sudden creation of the vacancy however needs to relax to an equilibrium configuration. As this process occurs at finite damping, the domain radius of twisted magnetic moments oscil-

lates during the relaxation. The temporarily larger radius in this case can already cause the nucleation of a skyrmion. To really simulate a nucleation at zero temperature and without fluctuations we therefore need to increase the current density slowly enough to avoid these oscillations.
The final simulation we perform for the above given parameters on a square lattice of 60×60 sites with periodic boundary conditions. Further we find that the size of the time steps needs to be decreased from initially $dt = 0.5/J$ for the simulations of the pinning at a vacancy, section 2.5, to $dt = 0.001/J$ for the simulation of the nucleation. Otherwise again the skyrmions are created due to fluctuations instead of the intrinsic nucleation process that we want to observe. The by two orders of magnitude smaller time steps result from a required current density which is larger by approximately the same amount. To observe a nucleation process we at least needed a current density of approximately $j = 0.2J$. The resulting nucleation is shown in figure 5.36.

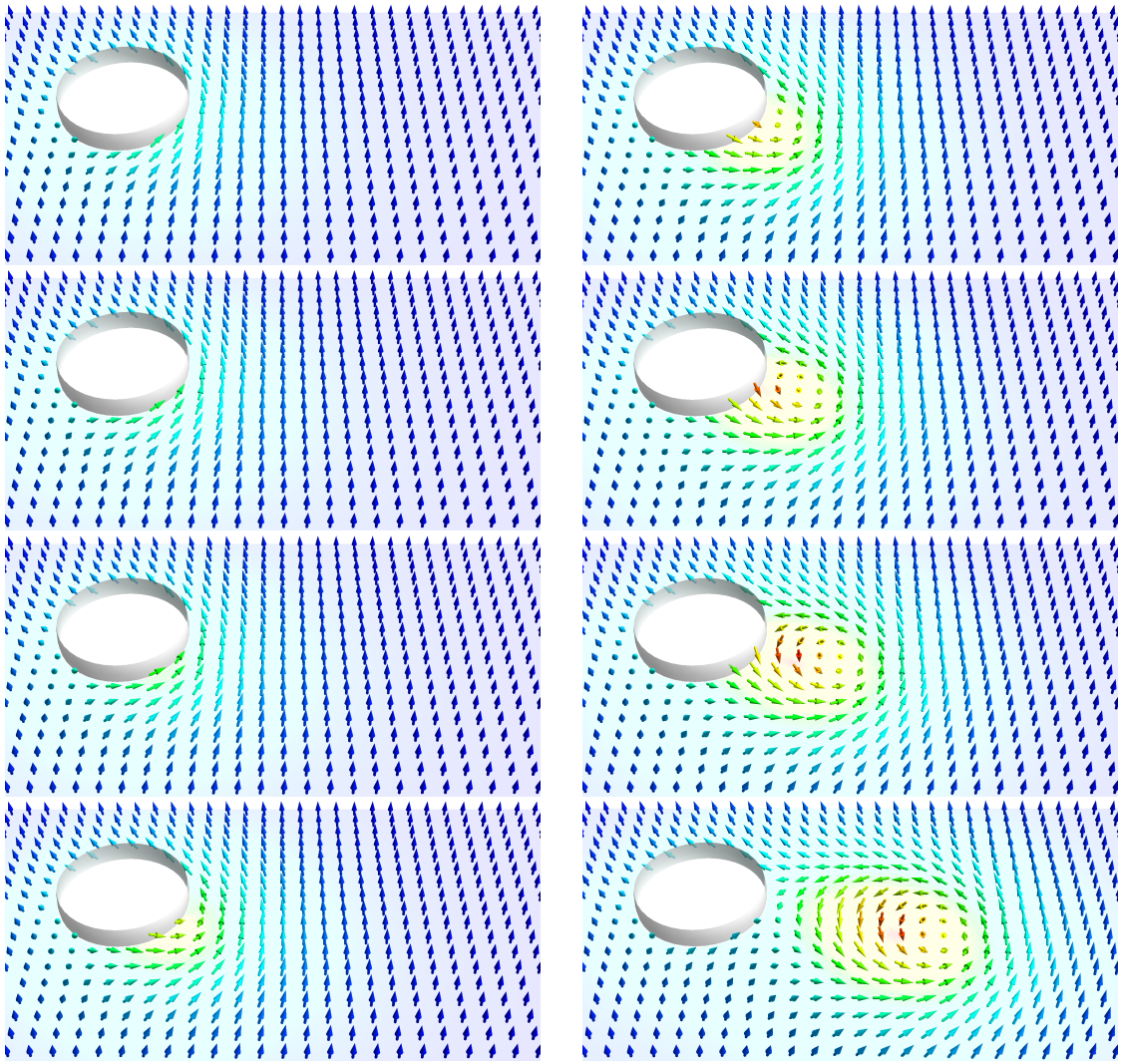

Figure 5.36: Nucleation of a skyrmion a at vacancy. Result from micromagnetic LLG simulation with parameters $D = 0.3J$, $B = 0.09J$, $\alpha = \beta = 0.4$, $j = 0.2J\mathbf{e}_\mathrm{x}$, $a = 1$. Skyrmion radius is equal to the vacancy radius. Figures show configuration at times $tJ = 0, 60, 90, 120, 130, 140, 150, 180$. The timeline is top to bottom, left to right.

One observes that due to the applied current density the twisting of the magnetic moments is not isotropic. The domain of twisted magnetic moments on the right of the vacancy is larger as the current pulls the magnetic configuration to the right. During the process of nucleation this twisted region expands slowly. As soon as the width of the region has become comparable to the radius of a skyrmion the process speeds up and the Dzyaloshinskii-Moriya interaction becomes stronger than the coupling to the current density. This causes the magnetic moments to automatically build a skyrmion center with an interger winding number. Now the winding on the left of the skyrmion center, which is still attached to the vacancy, has magnetic moments pointing opposite to the prefered twisting of the vacancy. This effect supports the detaching of the skyrmion by the strong current density. Finally the skyrmion is completely detached from the vacancy and gets freely driven through the system. At the same time the magnetic moments at the vacancy relax again by twisting back to the initial configuration, which will then again build up an extended region of twisted magnetic moments to finally release a new skyrmion. This process then continues periodically. It certainly is possible to determine a skyrmion creation rate dependent on the size of the vacancy, the current density or the magnetic field strength. However, the aim of this section is only to show that the nucleation of skyrmions at a vacancy in general is possible, which is the case for at least one presented set of parameters.

A further topic of this section is the *annihilation* of skyrmions at a vacancy.

In the setup which we consider, meaning single skyrmions in a ferromagnetic background, the skyrmion is only a metastable excitation of the system. The true groundstate of the system is the polarized phase, hence for the system it is energetically more favourable to destroy the skyrmion. Now one special property of skyrmions becomes important again, which is that skyrmions are topologically protected. The magnetic structure of a skyrmion provides an integer winding number which has to somehow be unwinded. However, this is not possible by a smooth transformation of the magnetic structure, assumed the magnetization is a smooth, continuus function. As an example we can consider the pressure acting on the skyrmion in the ferromagnetic background. Due to the pressure, which is a consequence of the magnetic field prefering the polarized phase, the skyrmion shrinks but can not be unwinded. This in particular becomes clear when regarding the magnetization in the center which points opposite to the background magnetization: at this point the skyrmion is rotation invariant in the plane, meaning the magnetization has no prefered direction to turn to. Except by flipping the central magnetic moment in a non-smooth transformation it cannot be unwinded. But also if we managed to turn this magnetic moment to any side, the magnetization still is a smooth function with a constant absolute value and hence the central magnetic moment only gets *moved* but not *removed*. The only way to really destroy the skyrmion therefore is by inverting the magnetization of the central magnetic moment.

If we consider the magnetization to be localized on a lattice, as we do when simulating the LLG equation, then the situation is different: here the magnetization is not a smooth function. Furthermore the before mentioned central spin does only exist if the skyrmion is centered on a site of the lattice. If this condition is not fulfilled, which in general should be the case, then the skyrmion can be smoothly unwinded: the pressure of the ferromagnetic background acts on the skyrmion but in contrast to the continuum case the central magnetic moment does not even exist. Therefore there is no need to invert it. The process of unwinding is also shown in figure 5.37. There a skyrmion centered exactly between four lattice sites was prepared at a lower magnetic field strength. Afterwards the magnetic field strength was turned up to an arbitrary strength at which the pressure from the polarized background destroys the skyrmion

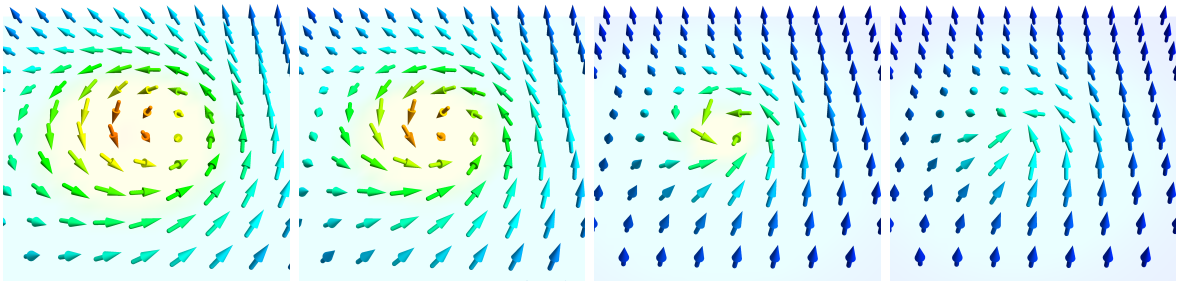

Figure 5.37: Destruction of a skyrmion on a lattice. Result of micromagnetic LLG simulation with parameters $D = 0.3J$, $B = 0.2J$, $\alpha = \beta = 0.4$, $a = 1$. Direction of time is left to right in arbitrary steps.

by shrinking it into the empty space between the lattice sites.

This example shows that by breaking the topology of the skyrmion it *can* be destroyed smoothly, but it does not get destroyed automatically. Otherwise the skyrmions at magnetic fields above the skyrmion phase would always decay on the lattice. Additionally to avoiding the problem of inverting the central spin smoothly, what also needs to be given to destroy a skyrmion is a large enough magnetic field pressure compared to the energy gain from leaving the core of the skyrmion at finite extension. Therefore to destroy a skyrmion by a vacancy, we in a way need to increase the relative pressure by the magnetic field or reduce the energy contribution from the center of the skyrmion.

The second condition is exactly fulfilled by a vacancy. In section 2.4 we calculated the energy difference for a single skyrmion in a ferromagnetic background with a vacancy numerically. This we used as the potential of a vacancy. For the numerical results see figure 2.10. This data

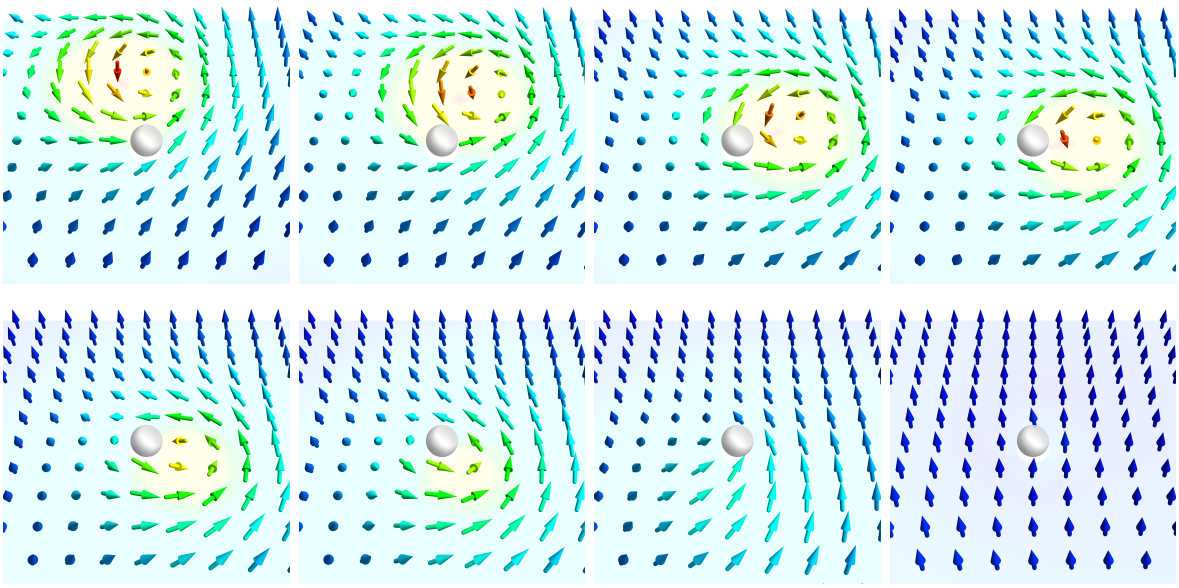

Figure 5.38: Destruction of a skyrmion by a vacancy (in the center). Result of micromagnetic LLG simulation with parameters $D = 0.3J$, $B = 0.12J$, $\alpha = \beta = 0.4$, $a = 1$. Direction of time is left to right, top to bottom. Figures show configurations at times $tJ = 0, 140, 280, 310, 340, 348, 350, 360$.

does not only give an estimate for the energy gain in the presence of a vacancy. It also yields the position of the vacancy inside the skyrmion for the equilibrium case.
Concerning the destruction of skyrmions, an interesting combination of parameters therefore is the skyrmion shape $\zeta = {}^{4}/_{3}$ and a hole radius $R_H = 0.4R$. The numerical units shown in the corresponding figure and section are $D = 0.3J$, $B = 0.12J$, square lattice spacing $a = 1$ and a vacancy as one empty site. From the figure 2.10 we obtain for these parameters that the potential has a minimum at zero distance, meaning that the skyrmion prefers to have the vacancy right in the center. According to our previous assumptions this intrinsic placement of a vacancy in the center and the hereby gain of energy might lead to a destruction of the skyrmion.
This indeed is what we observe when simulating the full micromagnetic LLG equation with a single-site vacancy and the above parameters in the absence of a current density, see figure 5.38. The skyrmion gets attracted and finally in a rotation collapses into the vacancy. This observation is remarkable as the skyrmion without the vacancy is stable.
For lower magnetic fields but otherwise constant parameters we do not observe a destruction but a pinning of the skyrmion as described in chapter 2. Only if we increase the size of the vacancy in these parameter regimes we can also observe the skyrmions getting destroyed the same way as in figure 5.38.
An interesting consequence for a possible application therefore is that a once pinned skyrmion can be much more easily destroyed than a free skyrmion. Although a vacancy could be used to pin a skyrmion, it also badly influences another important property of the skyrmion which is its stability.

6. Summary and Outlook

In this thesis the interaction of single skyrmions with vacancies in two dimensions has been studied analytically and numerically.

First we simulated the full micromagnetic LLG equation for a single skyrmion in the presence of an applied current density and got an impression of the interaction between the skyrmion and a vacancy of the size of one lattice site. The resulting trajectories we compared to results that we gained from the analysis of the Thiele equation. To really make quantitative use of the Thiele equation we introduced two different algorithms to calculate the potential which a skyrmion feels in the presence of a vacancy. Further we analyzed the scaling properties and the asymptotic behaviour of this potential. With these results we found that the Thiele equation can describe the movement of a single skyrmion with a vacancy in very good agreement with the full micromagnetic LLG equation. Using properties of the Thiele equation we could construct a very efficient algorithm to calculate the separatrices of the two-body interaction between skyrmion and vacancy. These separatrices, which are the critical trajectories deviding capturing from non-capturing trajectories, could be used to extract the capturing cross section (CCS). The CCS is an effective measure for the efficiency of the vacancy for capturing a skyrmion. Also the behaviour of the CCS could be described by the fixed point analysis of the Thiele equation close to the first critical current density. The result of these calculations is the phase diagram, figure 6.39. It shows the existance of three elementary phases of the skyrmion-vacancy-interaction: at low current densities there is repulsion of the skyrmions if they are outside the separatrix and hence these skyrmions can not get pinned. This phase we refer to as the repulsive phase. Further for larger current densities the separatrix opens up and skyrmions can be captured within the capturing cross section: the capturing phase. Finally for even larger current densities, the force by the current is stronger than the pinning by the vacancy and skyrmions get never get pinned but always move freely with small disturbance by the vacancy: the free phase.

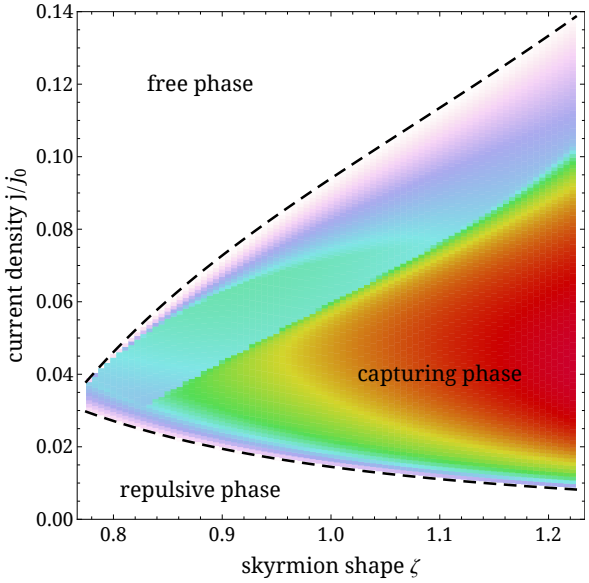

Figure 6.39: Phase diagram of single skyrmion-vacancy-interaction for $\alpha = \beta = 0.4$ in two dimensions and vacancy as one lattice site.

Further analysis of the repulsive and the free phase showed that in these phases the skyrmions obey a skyrmion flow Hall effect. On average, when they are guided past the vacancy they collect an offset relative to their starting position perpendicular to the direction of the current density. Also it turns out that the skyrmions in the repulsive phase are accelerated by the vacancy whereas in the free phase they are on average slowed down. These results we gained from numerical calculations and could confirm them by a perturbative treatment of the Thiele

equation in the free phase. The effects thereby both decay to leading order with $^1/_{j^2}$. Using the speed-up at the vacancy and the Hall effect we could calculate numerically the effective damping parameters. The behaviour of the effective damping β' could also be given by the perturbative approximations which for the effective damping α' only gave the limiting value. By an analytic treatment we could also show that for large current densities the effective damping parameters converge towards the initial parameters.
Furthermore we showed that the Thiele equation with a reasonable chosen potential can in a suitable range of the current density also describe the motion of a skyrmion close to an extended vacancy, here a straight vacancy wall. For this problem with an exponential potential the Thiele equation could also be solved analytically.
Finally, in the last chapter of this thesis, we showed by numerical simulations of the LLG equation that extended vacancies can also be used to both nucleate and annihilate skyrmions.

Concerning the pinning of a skyrmion at a vacancy there is one case left that has not been discussed yet in this thesis: what happens, if a vacancy which is already occupied by a skyrmion is approached by another skyrmion? Possible consequences that one could analyze in more detail are a repulsion between the skyrmions, a hitting after which the pinned skyrmion gets freed or even an accumulation of skyrmions at the vacancy and the formation of a local or extended skyrmion lattice.
Also in this thesis only purely two-dimensional systems have been considered. However, in reality two-dimensional materials are hard to build, so an interesting future project could be to investigate how all the effects discussed in this thesis behave when extending the two-dimensional system to a bulk system. Further in a bulk with one spatial dimension in addition, one more geometrical degree of freedom is present, meaning that as well new types of defects can be considered as also other motions of the one-dimensional skyrmion-tubes will occur.
Another already broadly discussed field in skyrmionics are the pinning forces for the lattice. Hence not only an extension of the present work into three dimensions but also or alternatively to the skyrmion lattice could be an option for further research. Alternatively, instead of increasing the number of skyrmions, one could also consider the single skyrmion in the presence of an increased number of vacancies, e.g. the interaction of a skyrmion with two vacancies.
Although the most natural type of disorder, vacancies are not the only type of disorder which plays a role in the interaction with skyrmions. Another natural type of disorder which might easily occur in two-dimensional systems are impurity atoms from the substrate. These would then not cause a zero-magnetization site as the vacancy does but in a first approximation a site with just a different absolute magnetization which could lead to pinning or local repulsion again.

7. Deutsche Zusammenfassung

In dieser Arbeit wird analytisch wie numerisch der Einfluss von Störstellen des Kristallgitters auf einzelne magnetische, chirale Skyrmionen im ferromagnetischen Hintergrund untersucht. Bei den betrachteten Störstellen handelt es sich ausschließlich um Fehlstellen im Sinne von freien, nicht besetzten Gitterplätzen.
Dazu werden Trajektorien einzelner Skyrmionen, die durch einen Strom getrieben werden, mittels einer numerischen Integration der Landau-Lifshitz-Gilbert Gleichung in Anwesenheit einer Fehlstelle im Gitter simuliert. Anschließend werden diese Trajektorien mit analytischen Ergebnissen der Thiele-Näherung vergleichen, wobei das Potential, welches in der Thiele-Gleichung benötigt wird, ebenfalls numerisch bestimmt wird. Zur Bestimmung der Potentiale werden zwei Algorithmen vorgestellt und deren Ergebnisse vergleich. Der Ergebnis des Vergleichs, dass die Trajektorien aus voller Simulation der LLG-Gleichung und der Thiele-Gleichung hinreichend übereinstimmen, wird genutzt, um ein Phasendiagramm der Interaktion von Skyrmion mit Fehlstellen unter Anwesenheit eines angelegten Stroms erstellen zu können. Eine auftretende Phase ist die *repulsive Phase*, in der bei geringen Strömen die Interaktion repulsiv ist und nur solche Skyrmionen an der Fehlstelle gehalten werden können, die sich bereits nahe genug an der Fehlstelle befinden. Weiterhin gibt es eine *einfangende Phase*, in der ein Skyrmion an einer Fehlstelle eingefangen und festgehalten werden kann. Als Parameter für die Effizienz des Einfangens wird der Einfangquerschnitt eingeführt, welcher auch in Grafik 6.39 genutzt wird. Durch Anwenden der Thiele-Gleichung lässt sich dieser extrem effizient berechnen. Die letzte auftretende Phase ist die *freie Phase*, in welcher keine Skyrmionen mehr an Fehlstellen festgehalten werden können, da die treibende Kraft durch den Strom zu stark ist.
Eine weitere Untersuchung der repulsive und freien Phase zeigen einen Hall-Effekt für Skyrmionen in beiden Phasen. In der einfangenden Phase ist dieser durch das Festhalten von Skyrmionen nicht definiert und wird daher nicht weiter untersucht. Weiterhin tritt in der repulsiven Phase ein Beschleunigungseffekt für Skyrmionen auf. In der freien Phase ist gegenteiliges der Fall: Die Skyrmionen werden, wie im klassischen Bild von Reibung gewohnt, abgebremst und nicht beschleunigt. Aus diesen beiden Effekten werden die effektiven Dämpfungsparameter des Systems durch den Fehlstelleneinfluss berechnet. Die numerischen Ergebnisse der repulsiven Phase können dabei durch logarithmische Funktionen beschrieben werden. In der freien Phase ist eine Beschreibung der numerischen Ergebnisse sogar analytisch mittels einer störungstheoretischen Rechnung zweiter Ordnung sehr gut möglich.
Abschließend wird in dieser Arbeit gezeigt, dass auch andere als punktförmige Fehlstellen durch die Thiele-Gleichung beschrieben werden können. Als Beispiel ist hier das Verhalten an einer Fehlstellenwand aufgeführt, welches durch die Annahme eines exponentiellen Potentials sogar analytisch exakt lösbar ist. Außerdem wird durch numerische Simulation der LLG-Gleichung gezeigt, dass Skyrmionen an Fehlstellen sowohl durch Strom erzeugt wie auch leicht vernichtet werden können.

A. Appendix

A.1. Fixed Point Analysis of the Thiele Equation

The two-dimensional equation of motion for a skyrmion in the Thiele approximation is given by:

$$\dot{\mathbf{r}} = \mathcal{A}^{-1}\mathbf{F}(\mathbf{r}) + \mathbf{j} \tag{A.83}$$

where the fixed point condition leads

$$-\mathcal{A}^{-1}\mathbf{F}(\mathbf{r}_{\mathrm{FP}}) = \mathbf{j}. \tag{A.84}$$

A linearization around the fixed point is done by a Taylor expansion of the position dependent force around this point up to first order, $\mathbf{F}(\mathbf{r}) \approx \mathbf{F}(\mathbf{r}_{\mathrm{FP}}) + \mathcal{B}(\mathbf{r} - \mathbf{r}_{\mathrm{FP}})$, where $\mathcal{B}$ is the linear flow matrix $\mathcal{B}_{\mathrm{i,j}} = \partial_{\mathrm{i}} F_{\mathrm{j}}$. The derivatives in direction $\mathbf{e}_{\mathrm{x}}$ can be calculated:

$$\begin{aligned}
\partial_{\mathrm{x}}\mathbf{F}(\mathbf{r}) &= -\partial_{\mathrm{x}} V'(r)\mathbf{e}_{\mathrm{r}} \\
&= -\partial_{\mathrm{x}} \frac{V'(r)}{r}(x\mathbf{e}_{\mathrm{x}} + y\mathbf{e}_{\mathrm{y}}) \\
&= -\frac{V'(r)}{r}\mathbf{e}_{\mathrm{x}} - (\partial_{\mathrm{x}} r)\left(\partial_{\mathrm{r}} \frac{V'(r)}{r}\right)\mathbf{r} \\
&= -\frac{V'(r)}{r}\mathbf{e}_{\mathrm{x}} - \left(\frac{x}{r}\right)\left(-\frac{V'(r)}{r^2} + \frac{V''(r)}{r}\right)\mathbf{r} \\
&= \left(-\frac{V'(r)}{r} + \frac{x^2}{r^2}\left(\frac{V'(r)}{r} - V''(r)\right)\right)\mathbf{e}_{\mathrm{x}} + \frac{xy}{r^2}\left(\frac{V'(r)}{r} - V''(r)\right)\mathbf{e}_{\mathrm{y}}
\end{aligned} \tag{A.85}$$

The derivatives in direction $\mathbf{e}_{\mathrm{y}}$ are the same with labels x and y inverted. Consequently, the linear flow matrix $\mathcal{B}$ reads:

$$\mathcal{B} = \begin{pmatrix} -\frac{V'(r)}{r} + \frac{x^2}{r^2}\left(\frac{V'(r)}{r} - V''(r)\right) & \frac{xy}{r^2}\left(\frac{V'(r)}{r} - V''(r)\right) \\ \frac{xy}{r^2}\left(\frac{V'(r)}{r} - V''(r)\right) & -\frac{V'(r)}{r} + \frac{y^2}{r^2}\left(\frac{V'(r)}{r} - V''(r)\right) \end{pmatrix}_{r=r_{\mathrm{FP}}} \tag{A.86}$$

Now we use what followed from equation 2.30 and recover:

$$\begin{aligned}
\mathcal{B} &\overset{2.30}{=} \frac{1}{\gamma^2}\left(-V''(r_{\mathrm{FP}}) + \frac{V'(r_{\mathrm{FP}})}{r_{\mathrm{FP}}}\right)\begin{pmatrix} D^2 & D\mathcal{G} \\ D\mathcal{G} & \mathcal{G}^2 \end{pmatrix} - \frac{V'(r_{\mathrm{FP}})}{r_{\mathrm{FP}}}\begin{pmatrix} 1 & 0 \\ 0 & 1 \end{pmatrix} \\
&=: \mathcal{B}_1 + \mathcal{B}_2
\end{aligned} \tag{A.87}$$

For later purposes we divide the matrix up into two parts, $\mathcal{B}_1$ and $\mathcal{B}_2$. Further, we calculate the determinant of this linear flow matrix as we will need it later on:

$$\begin{aligned}
\det(\mathcal{B}) &= \det\left[\frac{1}{\gamma^2}\left(-V''(r_{\mathrm{FP}}) + \frac{V'(r_{\mathrm{FP}})}{r_{\mathrm{FP}}}\right)\begin{pmatrix} D^2 & D\mathcal{G} \\ D\mathcal{G} & \mathcal{G}^2 \end{pmatrix} - \frac{V'(r_{\mathrm{FP}})}{r_{\mathrm{FP}}}\begin{pmatrix} 1 & 0 \\ 0 & 1 \end{pmatrix}\right] \\
&= \left[\frac{D^2}{\gamma^2}\left(-V''(r_{\mathrm{FP}}) + \frac{V'(r_{\mathrm{FP}})}{r_{\mathrm{FP}}}\right) - \frac{V'(r_{\mathrm{FP}})}{r_{\mathrm{FP}}}\right] \cdot \left[\frac{\mathcal{G}^2}{\gamma^2}\left(-V''(r_{\mathrm{FP}}) + \frac{V'(r_{\mathrm{FP}})}{r_{\mathrm{FP}}}\right) - \frac{V'(r_{\mathrm{FP}})}{r_{\mathrm{FP}}}\right] \\
&\quad - \frac{\mathcal{G}^2 D^2}{\gamma^4}\left(-V''(r_{\mathrm{FP}}) + \frac{V'(r_{\mathrm{FP}})}{r_{\mathrm{FP}}}\right)^2 \\
&= \frac{V'(r_{\mathrm{FP}})V''(r_{\mathrm{FP}})}{r_{\mathrm{FP}}}
\end{aligned} \tag{A.88}$$

Finally, using the result of equation 2.31, the determinant becomes:

$$\det(\mathcal{B}) = \operatorname{sgn}(V'(r_{\mathrm{FP}}))V''(r_{\mathrm{FP}})\frac{j\gamma}{r_{\mathrm{FP}}} \tag{A.89}$$

As with this linear flow matrix $\mathcal{B}$ the linearized form of the equation of motion around a fixed point becomes after shifting $\mathbf{r} \to \mathbf{r} + \mathbf{r}_{\mathrm{FP}}$

$$\dot{\mathbf{r}} = \mathcal{A}^{-1}\mathcal{B}\mathbf{r} = \mathcal{C}\mathbf{r} \tag{A.90}$$

the eigenvalues determine the stability of the given fixed point $\mathbf{r}_{\mathrm{FP}}$. As the eigenvalues $\lambda_\pm$ of any 2×2 matrix M are given by the general formula

$$\lambda_\pm(M) = \frac{\operatorname{tr}(M)}{2} \pm \sqrt{\frac{\operatorname{tr}(M)^2}{4} - \det(M)} \tag{A.91}$$

where $\operatorname{tr}(M)$ denotes the trace and $\det(M)$ the determinant of M, the eigenvalues of $\mathcal{C}$ now can easily be calculated. The matrix $\mathcal{A}^{-1}$ can also be written down immediately as for 2×2 matrices a general formula for the inverse is known:

$$\mathcal{A}^{-1} = \frac{1}{\det(\mathcal{A})}\begin{pmatrix} D & \mathcal{G} \\ -\mathcal{G} & D \end{pmatrix}. \tag{A.92}$$

where the determinant is given by $\det(\mathcal{A}) = \gamma^2$ and thus $\det(\mathcal{A}^{-1}) = \gamma^{-2}$. Using this result and that we already calculated the determinant of $\mathcal{B}$, see A.89, the determinant of $\mathcal{C}$ is

$$\det(\mathcal{C}) = \det(\mathcal{A}^{-1})\,\det(\mathcal{B}) = \operatorname{sgn}(V'(r_{\mathrm{FP}}))V''(r_{\mathrm{FP}})\frac{j}{r_{\mathrm{FP}}\gamma} \tag{A.93}$$

For the trace of $\mathcal{C}$ we can use that we devided $\mathcal{B}$ into two parts where one is given by the unity matrix only:

$$\begin{aligned}
\operatorname{tr}(\mathcal{C}) &= \operatorname{tr}(\mathcal{A}^{-1}\mathcal{B}) = \operatorname{tr}(\mathcal{A}^{-1}\mathcal{B}_1) + \operatorname{tr}(\mathcal{A}^{-1}\mathcal{B}_2) \\
&= \operatorname{tr}(\mathcal{A}^{-1}\mathcal{B}_1) - \frac{2D}{\gamma^2}\frac{V'(r_{\mathrm{FP}})}{r_{\mathrm{FP}}} \\
&= \frac{1}{\gamma^4}\left(-V''(r_{\mathrm{FP}}) + \frac{V'(r_{\mathrm{FP}})}{r_{\mathrm{FP}}}\right)\operatorname{tr}\left[\begin{pmatrix} D & \mathcal{G} \\ -\mathcal{G} & D \end{pmatrix}\begin{pmatrix} D^2 & D\mathcal{G} \\ D\mathcal{G} & \mathcal{G}^2 \end{pmatrix}\right] - 2V'(r_{\mathrm{FP}})\frac{D}{r_{\mathrm{FP}}\gamma^2} \\
&= \frac{D}{\gamma^2}\left(-V''(r_{\mathrm{FP}}) + \frac{V'(r_{\mathrm{FP}})}{r_{\mathrm{FP}}}\right) - 2V'(r_{\mathrm{FP}})\frac{D}{r_{\mathrm{FP}}\gamma^2} \\
&= -\frac{D}{\gamma^2}\left(V''(r_{\mathrm{FP}}) + \operatorname{sgn}(V'(r_{\mathrm{FP}}))\frac{j\gamma}{r_{\mathrm{FP}}}\right)
\end{aligned} \tag{A.94}$$

These expressions for the trace and the determinant of the linear flow matrix $\mathcal{C}$ we can use to plug them into the general expression for eigenvalues, A.91, and recover:

$$\begin{aligned}
\lambda_\pm(\mathcal{C}) &= \frac{\operatorname{tr}(\mathcal{C})}{2} \pm \sqrt{\frac{\operatorname{tr}(\mathcal{C})^2}{4} - \det(\mathcal{C})} \\
&= -\frac{D}{2\gamma^2}\left(V''(r_{\mathrm{FP}}) + \operatorname{sgn}(V'(r_{\mathrm{FP}}))\frac{j\gamma}{r_{\mathrm{FP}}}\right) \\
&\quad \pm \sqrt{\frac{D^2}{4\gamma^4}\left(V''(r_{\mathrm{FP}})^2 + \frac{j^2\gamma^2}{r_{\mathrm{FP}}^2}\right) - \operatorname{sgn}(V'(r_{\mathrm{FP}}))\frac{j}{2r_{\mathrm{FP}}\gamma^3}\left(D^2 + 2\mathcal{G}^2\right)V''(r_{\mathrm{FP}})}
\end{aligned} \tag{A.95}$$

To gain more insight into the stability of the fixed points, the eigenvalues have to be analyzed further according to the equations 2.34. The first distinction to make is whether a fixed point is definite or semidefinite. In the case of a definite fixed point the matrix $\mathcal{C}$ has to be definite, meaning all eigenvalues need to have the same sign. For this to happen, absolute value of the square root needs to be smaller than the absolute value of the expression in front of the square root. Apparently, this is the case if the determinant of $\mathcal{C}$ is larger than zero. Further using that the current density j, the distance r_{FP} and the normalization factor γ are all larger than zero, the condition for having a definite fixed point reads:

$$\mathrm{sgn}(V'(r_{\mathrm{FP}}))V''(r_{\mathrm{FP}}) > 0 \tag{A.96}$$

which can also be rewritten such that the exact value of $V''(r_{\mathrm{FP}})$ is not of interest anymore:

$$\mathrm{sgn}(V'(r_{\mathrm{FP}}))\,\mathrm{sgn}(V''(r_{\mathrm{FP}})) \gtrless 0 \quad {}^{\text{definite}}/_{\text{semidefinite}} \tag{A.97}$$

The other sort of fixed points that is to distinguish are definite fixed points that can either be stable oder unstable. In the case of a stable fixed point all eigenvalues have to be smaller than zero. From equation A.91 follows that this can only be the case, if the trace is also smaller than zero. The prefactors D and γ both are positive, hence the condition to have a stable fixed point reads:

$$\mathrm{sgn}(V'(r_{\mathrm{FP}}))\frac{j\gamma}{r_{\mathrm{FP}}} > -V''(r_{\mathrm{FP}}) \tag{A.98}$$

Now one can use that a necessary condition for a stable fixed point is that it has to be definite, therefore both $V'(r_{\mathrm{FP}})$ and $V''(r_{\mathrm{FP}})$ have to have the same sign. As all factors in the fraction are always positive, consequently both sides of the equation have opposite signs. The whole inequality can thus be reduced to a comparison of the signs: If the sign of $V'(r_{\mathrm{FP}})$ is positive, then the inequality will always be fulfilled. On the other hand, if the sign is negative, the right hand side will always be larger. Hence we can conclude:

$$\mathrm{sgn}(V'(r_{\mathrm{FP}})) \gtrless 0 \quad {}^{\text{stable}}/_{\text{unstable}} \tag{A.99}$$

Finally we can calculate the eigenvectors of $\mathcal{C}$ which is easy as there exists a general form for the eigenvectors of a 2×2 matrix M:

$$\mathbf{e}_{\pm}(M) = \begin{pmatrix} \lambda_{\pm} - M_{2,2} \\ M_{2,1} \end{pmatrix} \tag{A.100}$$

In the case $M = \mathcal{C}$ we need to calculate the matrix elements $\mathcal{C}_{2,1}$ and $\mathcal{C}_{2,2}$. Due to our previous choice of $\mathcal{B}_1$ and $\mathcal{B}_2$, we can easily see that the lower two entries of $\mathcal{C}$ are given only by $\mathcal{A}^{-1}\mathcal{B}_2$. As $\mathcal{B}_2$ basically is a unit matrix with a prefactor, the matrix elements can be read off:

$$\begin{aligned} \mathcal{C}_{2,1} &= \mathrm{sgn}(V'(r_{\mathrm{FP}}))\frac{j\mathcal{G}}{r_{\mathrm{FP}}\gamma} \\ \mathcal{C}_{2,2} &= -\mathrm{sgn}(V'(r_{\mathrm{FP}}))\frac{jD}{r_{\mathrm{FP}}\gamma} \end{aligned} \tag{A.101}$$

Hence the resulting eigenvectors are:

$$\begin{aligned} \mathbf{e}_{\pm}(\mathcal{C}) = &\begin{pmatrix} \frac{D}{2\gamma^2}\left(-V''(r_{\mathrm{FP}}) + \mathrm{sgn}(V'(r_{\mathrm{FP}}))\frac{j\gamma}{r_{\mathrm{FP}}}\right) \\ \mathrm{sgn}(V'(r_{\mathrm{FP}}))\frac{j\mathcal{G}}{r_{\mathrm{FP}}\gamma} \end{pmatrix} \\ \pm &\begin{pmatrix} \sqrt{\frac{D^2}{4\gamma^4}\left(V''(r_{\mathrm{FP}})^2 + \frac{j^2\gamma^2}{r_{\mathrm{FP}}^2}\right) - \mathrm{sgn}(V'(r_{\mathrm{FP}}))\frac{j}{2r_{\mathrm{FP}}\gamma^3}\left(D^2 + 2\mathcal{G}^2\right)V''(r_{\mathrm{FP}})} \\ 0 \end{pmatrix} \end{aligned} \tag{A.102}$$

A.2. Perturbation Theory Part 1: Hall Effect

The aim of this section is to calculate the Hall effect resulting from vacancies in the free phase, compare section 3.1.2. Thus we need to calculate the offset integral

$$\langle \Delta y \rangle_\infty = \int_{-\infty}^{\infty} \Delta y(y_0)\, \mathrm{d}y_0 = \int_{-\infty}^{\infty} y(t \to \infty, y_0) - y_0\, \mathrm{d}y_0 \tag{A.103}$$

since it directly is related to the Hall angle, see equations 3.56 and finally 3.58. The first contribution $y(t \to \infty, y_0)$ we want to approximate by perturbation theory to second order.
As basic ingredient to find a perturbative solution for the Hall effect caused by a vacancy, here in the free phase, we need the effective equation of motion for the single skyrmion in the presence of a vacancy which is the Thiele equation 2.26:

$$\dot{\mathbf{r}} = -V'(r)\mathcal{A}^{-1}\mathbf{e}_\mathrm{r} + \mathbf{j} \tag{A.104}$$

where we have the derivative of the potential $V'(r)$ dependent on the distance between skyrmion an vacancy r, $\mathbf{e}_\mathrm{r}$ the radial unit vector in cylindrical coordinates, and the inverse rotation matrix $\mathcal{A}^{-1}$. This matrix is given by

$$\mathcal{A}^{-1} = \frac{1}{\gamma^2}\begin{pmatrix} \mathcal{D} & \mathcal{G} \\ -\mathcal{G} & \mathcal{D} \end{pmatrix} \tag{A.105}$$

with $\gamma^2 = \mathcal{D}^2 + \mathcal{G}^2$. Further we assume, according to all simulations in this thesis, that the current density $\mathbf{j}$ only point in the direction of the x-axis.
To apply perturbation theory in a convenient sense which is as an expansion in a small parameter ε, we rewrite the Thiele equation in the way we will use it in the following calculation

$$\begin{pmatrix} \dot{x}(t) \\ \dot{y}(t) \end{pmatrix} = -\varepsilon \frac{V'(r(t))}{\gamma^2 r(t)} \begin{pmatrix} \mathcal{D} & \mathcal{G} \\ -\mathcal{G} & \mathcal{D} \end{pmatrix} \begin{pmatrix} x(t) \\ y(t) \end{pmatrix} + \begin{pmatrix} j \\ 0 \end{pmatrix} \tag{A.106}$$

with $r^2(t) = x^2(t) + y^2(t)$ the radial coordinate or in the short version

$$\dot{\mathbf{r}}(t) = \varepsilon \mathbf{f}\left(\mathbf{r}(t)\right) + \mathbf{j} \tag{A.107}$$

with boundary conditions $\mathbf{r}(0) = \mathbf{r}_0 = (x_0, y_0)^\mathrm{T}$ and $\varepsilon = 1$ which is only introduced to clearify which term is assumed to be small.
Now we can define the perturbative ansatz $\mathbf{r}_\varepsilon$ by expanding in powers of the small parameter ε to second order where we stop:

$$\mathbf{r}_\varepsilon(t) \approx \mathbf{r}_0(t) + \varepsilon \mathbf{r}_1(t) + \varepsilon^2 \mathbf{r}_2(t). \tag{A.108}$$

This perturbative ansatz we plug into the exact expression for the solution which we gain from integrating the velocity field from equation A.107 over time and recover

$$\mathbf{r}_\varepsilon(t) \approx \int_0^t \varepsilon \mathbf{f}\left(\mathbf{r}_\varepsilon(t')\right) \mathrm{d}t' + \mathbf{j}t + \mathbf{r}_0. \tag{A.109}$$

From this equation we see that due to the prefactor ε in the integral we need to expand the integrand $\mathbf{f}\left(\mathbf{r}_\varepsilon(t)\right)$ only to first order in ε to recover terms of maximally second order in total.

However, the expansion of $\mathbf{f}\left(\mathbf{r}_\varepsilon(t)\right)$ to first order in ε yields

$$\mathbf{f}\left(\mathbf{r}_\varepsilon(t)\right) \approx \mathbf{f}\left(\mathbf{r}_0(t) + \varepsilon\mathbf{r}_1(t)\right) \approx \mathbf{f}\left(\mathbf{r}_0(t)\right) + \varepsilon\mathbf{J}_\mathbf{f}(\mathbf{r}_0(t))\mathbf{r}_1(t) \tag{A.110}$$

where $\mathbf{J}_\mathbf{f}(\mathbf{r}_0(t))$ is the Jacobian matrix defined by the entries $\left(\mathbf{J}_\mathbf{f}(\mathbf{r}_0(t))\right)_{\mathrm{i,j}} = \frac{\partial f_i(\mathbf{r}_0(t))}{\partial x_j}$. Combining this expansion with equation A.109 we recover

$$\begin{aligned}\mathbf{r}_\varepsilon(t) &\approx \int_0^t \varepsilon\mathbf{f}\left(\mathbf{r}_0(t')\right) + \varepsilon^2\mathbf{J}_\mathbf{f}(\mathbf{r}_0(t'))\mathbf{r}_1(t')\mathrm{d}t' + \mathbf{j}t + \mathbf{r}_0 \\ &= \mathbf{j}t + \mathbf{r}_0 + \varepsilon\int_0^t \mathbf{f}\left(\mathbf{r}_0(t')\right)\mathrm{d}t' + \varepsilon^2\int_0^t \mathbf{J}_\mathbf{f}(\mathbf{r}_0(t'))\mathbf{r}_1(t')\mathrm{d}t' \\ &= \mathbf{r}_0(t) + \varepsilon\mathbf{r}_1(t) + \varepsilon^2\mathbf{r}_2(t).\end{aligned} \tag{A.111}$$

This allows us to immediately read off the expressions for the different orders of expansion. In the following we analyze the contributions of the different terms to the offset integral. Here only the second component of the vectors which is the y-component are needed. Further we can apply again $\varepsilon = 1$ as it only was introduced for a better notation.
Starting with the zerost order expansion, $\mathbf{r}_0(t) = \mathbf{j}t + \mathbf{r}_0$, we obtain a constant for the offset integral as

$$\left(\mathbf{r}_0(t)\right)_y = y_0 \tag{A.112}$$

which exactly cancels the constant y_0 which is included in the definition of the offset integral, see equation A.103.
The first order expansion, $\mathbf{r}_1(t) = \int_0^t \mathbf{f}\left(\mathbf{r}_0(t')\right)\mathrm{d}t'$, when including the integration over y_0 which is included in the definition of the offset integral vanishes. This can be shown by the following:

$$\begin{aligned}\int_{-\infty}^{\infty}\mathrm{d}y_0\left(\mathbf{r}_1(t\to\infty, y_0)\right)_y &= \int_{-\infty}^{\infty}\mathrm{d}y_0\int_0^{\infty}\mathrm{d}t'\left(\mathbf{f}\left(\mathbf{r}_0(t')\right)\right)_y \\ &= \int_{-\infty}^{\infty}\mathrm{d}y_0\int_0^{\infty}\mathrm{d}t' - \frac{V'(r_0(t'))}{\gamma^2 r_0(t')}\left(-\mathcal{G}x_0(t') + \mathcal{D}y_0(t')\right)\end{aligned} \tag{A.113}$$

with what we know from equation A.111: $x_0(t') = jt' + x_0$, $y_0(t') = y_0$ and $r_0^2(t') = x_0^2(t') + y_0^2(t')$. We therefore perform the following substitutions:

$$x = x_0(t') = jt' + x_0,\ \mathrm{d}x = j\mathrm{d}t' \tag{A.114}$$

$$y = y_0(t') = y_0, \qquad \mathrm{d}y = \mathrm{d}y_0 \tag{A.115}$$

$$\Rightarrow r = \sqrt{x^2 + y^2} > 0 \tag{A.116}$$

Finally what we have to take care of is that for a propper definition of the offset integral not only $t \to \infty$ has to be applied but also $x_0 \to -\infty$. Thus using the substitution we recover

$$\int_{-\infty}^{\infty}\mathrm{d}y_0\left(\mathbf{r}_1(t\to\infty, y_0)\right)_y = \int_{-\infty}^{\infty}\mathrm{d}(x,y) - \frac{V'(r)}{\gamma^2 r}\left(-\mathcal{G}x + \mathcal{D}y\right) = 0 \tag{A.117}$$

as all functions dependent on the radial coordinate r by definition are even functions. Since they are multiplied with either x or y they become odd with respect to this component and therefore the integral over the whole two-dimensional plane vanishes.

After the first orders of expansion do not yield any contribution except for annihilating the initial offset y_0, the offset integral becomes only dependent on the second order contribution

$$\langle \Delta y \rangle_\infty \approx \int_{-\infty}^{\infty} \left(\mathbf{r}_2(t \to \infty, y_0)\right)_y \, \mathrm{d}y_0 = \int_{-\infty}^{\infty} \mathrm{d}y_0 \int_0^{\infty} \mathrm{d}t' \left(\mathbf{J_f}(\mathbf{r}_0(t'))\mathbf{r}_1(t')\right)_y . \tag{A.118}$$

What we see here is that we only need half of the Jacobian matrix as in the end only the result second components are needed. To apply the derivatives we use that

$$\frac{\partial}{\partial x_i}\frac{V'(r)}{r} = \frac{\partial r}{\partial x_i}\frac{\mathrm{d}}{\mathrm{d}r}\frac{V'(r)}{r} = \frac{x_i}{r}\left(-\frac{V'(r)}{r^2} + \frac{V''(r)}{r}\right) \tag{A.119}$$

so that the terms we obtain for the components of the Jacobian matrix are

$$\left(\mathbf{J_f}(\mathbf{r})\right)_{\mathrm{y,x}} = \frac{\mathcal{G}V'(r)}{\gamma^2 r} - \frac{1}{\gamma^2}\left(-\frac{V'(r)}{r^3} + \frac{V''(r)}{r^2}\right) x(-\mathcal{G}x + \mathcal{D}y) \tag{A.120}$$

$$\left(\mathbf{J_f}(\mathbf{r})\right)_{\mathrm{y,y}} = -\frac{\mathcal{D}V'(r)}{\gamma^2 r} - \frac{1}{\gamma^2}\left(-\frac{V'(r)}{r^3} + \frac{V''(r)}{r^2}\right) y(-\mathcal{G}x + \mathcal{D}y). \tag{A.121}$$

Further we can obtain the expression for $\mathbf{r}_1(t')$ from equation A.113. This contributes another integration over time, $\int_0^{t'} \mathrm{d}t''$, such that there in total are two pairs of variables $\mathbf{r}_0(t')$ and $\mathbf{r}_0(t'')$. Hence we introduce a shorter notation writing $\mathbf{r}_0(t') = (x', y')^{\mathrm{T}}$ and $\mathbf{r}_0(t'') = (x'', y'')^{\mathrm{T}}$. The expression for the integrand of the offset integral then becomes

$$\begin{aligned}\left(\mathbf{J_f}(\mathbf{r}_0(t'))\mathbf{r}_1(t')\right)_y = \int_0^{t'} \mathrm{d}t'' &\frac{1}{\gamma^4}\frac{V'(r')}{r'}\frac{V'(r'')}{r''}\left(-2\mathcal{G}\mathcal{D}x'' - \left(\mathcal{G}^2 - \mathcal{D}^2\right)y''\right) \\ &+ \frac{1}{\gamma^4}\left(-\frac{V'(r')}{r'^3} + \frac{V''(r')}{r'^2}\right)\frac{V'(r'')}{r''} \\ &\cdot \left[x'(-\mathcal{G}x' + \mathcal{D}y')(\mathcal{D}x'' + \mathcal{G}y'') + y'(-\mathcal{G}x' + \mathcal{D}y')(-\mathcal{G}x'' + \mathcal{D}y'')\right].\end{aligned} \tag{A.122}$$

The lengthy expression in the last bracket produces many terms. Fortunately most of them are either odd in the product of y' and y'' or they cancel each other. The terms which are odd in y' respectively y'' drop because due to $y' = y'' = y_0$ they are odd in y_0 which by the integration in the offset integral vanishes. Furthermore this is the reason why the one of the first terms which is linear in y'' also drops after the integration over y_0. The only terms remaining can be summed up to

$$\begin{aligned}\left(\mathbf{J_f}(\mathbf{r}_0(t'))\mathbf{r}_1(t')\right)_y &= \int_0^{t'} \mathrm{d}t'' - \frac{2\mathcal{G}\mathcal{D}}{\gamma^4}\frac{V'(r')}{r'}\frac{V'(r'')}{r''}x'' \\ &\quad + \frac{1}{\gamma^4}\left(-\frac{V'(r')}{r'^3} + \frac{V''(r')}{r'^2}\right)\frac{V'(r'')}{r''}\left[-\mathcal{G}\mathcal{D}x''\left(x'^2 + y'^2\right)\right] \\ &= \int_0^{t'} \mathrm{d}t'' - \frac{\mathcal{G}\mathcal{D}}{\gamma^4}\frac{x''}{r''}V'(r'')\left(\frac{V'(r')}{r'} + V''(r')\right)\end{aligned} \tag{A.123}$$

Now we can use again the first substitution from equation A.114 for the coordinate x'':

$$\int_0^{t'} \mathrm{d}t'' \to \frac{1}{j}\int_{x''(0)=x_0}^{x''(t')=x'} \mathrm{d}x'' \tag{A.124}$$

and further we can use that $\frac{x''}{r''} = \frac{\partial r''}{\partial x''}$, $r''(x_0, y'') = r'(x_0, y') = r_0$ and $r''(x', y'') = r'(x', y') = r'$. Hence a next substitution leads to

$$\int_{x_0}^{x'} \mathrm{d}x'' \, \frac{x''}{r''} V'(r'') = \int_{x_0}^{x'} \mathrm{d}x'' \, \frac{\partial V(r'')}{\partial x''} = V(r') - V(r_0) \overset{r_0 \to -\infty}{\longrightarrow} V(r'). \tag{A.125}$$

Here we use that in the definition of the offset integral we need to take the limit $x_0 \to -\infty$ which also means $r_0 \to -\infty$. The definition of the potential we choose such that $V(-\infty) = V(\infty) = 0$. Consequently we arrive at the expression for the offset integral

$$\langle \Delta y \rangle_\infty \approx -\frac{\mathcal{GD}}{j\gamma^4} \int_{-\infty}^{\infty} \mathrm{d}y_0 \int_0^{\infty} \mathrm{d}t' V(r') \left(\frac{V'(r')}{r'} + V''(r') \right) \tag{A.126}$$

Now again we can perform the substitutions A.114 and A.115 and recover and integral over the full two-dimensional plane which we can simplify even more when changing to cylindrical coordinates

$$\begin{aligned} \langle \Delta y \rangle_\infty &\approx -\frac{\mathcal{GD}}{j^2\gamma^4} \int_{-\infty}^{\infty} \mathrm{d}(x, y) \, V(r) \left(\frac{V'(r)}{r} + V''(r) \right) \\ &= -\frac{\mathcal{GD}}{j^2\gamma^4} \int_0^{2\pi} \mathrm{d}\phi \int_0^{\infty} r \mathrm{d}r \, V(r) \left(\frac{V'(r)}{r} + V''(r) \right) \\ &= -\frac{2\pi\mathcal{GD}}{j^2\gamma^4} \int_0^{\infty} \mathrm{d}r \, \left\{ V(r)V'(r) + rV(r)V''(r) \right\} \end{aligned} \tag{A.127}$$

If we now perform a partial integration on the second term in the integrand we recover

$$\begin{aligned} \int_0^{\infty} \mathrm{d}r \, rV(r)V''(r) &= rV(r)V'(r)\big|_0^{\infty} - \int_0^{\infty} \mathrm{d}r \, \left\{ rV'(r)V'(r) + V(r)V'(r) \right\} \\ &= -\int_0^{\infty} \mathrm{d}r \, rV'^{\,2}(r) - \int_0^{\infty} \mathrm{d}r \, V(r)V'(r) \end{aligned} \tag{A.128}$$

Apart from a new integral which depends on the distance and the derivative of the potential only this reproduces the term we already had in the offset integral but with a different sign. Therefore these terms cancel each other and we arrive at the final expression for the offset integral

$$\langle \Delta y \rangle_\infty^{\mathrm{PT}\ 2} = \frac{2\pi\mathcal{GD}}{j^2\gamma^4} \int_0^{\infty} \mathrm{d}r \, rV'^{\,2}(r). \tag{A.129}$$

In general the potential of the vacancy can only be computed numerically and so does the integral. An example including numerical values is given in section 3.1.2.

A.3. Perturbation Theory Part 2: Speed-Up

The aim of this section is to calculate the speed-up effect resulting from vacancies in the free phase, compare section 3.2. Thus we need to calculate the delay integral according to the delay $\Delta x = j(t - t_0)$ as defined in equation 3.59.

$$\langle \Delta x \rangle_\infty = \int_{-\infty}^{\infty} \Delta x(y_0) \mathrm{d}y_0 = \int_{-\infty}^{\infty} jt + x_0 - (jt_0 + x_0) \mathrm{d}y_0 = \int_{-\infty}^{\infty} jt + x_0 - x(t, y_0) \mathrm{d}y_0. \tag{A.130}$$

In complete analogy to the previous section on the perturbative solution of the Hall effect, we define our perturbative ansatz in powers of ε and recover again in complete analogy to equation A.112 for the zerost order:

$$\left(\mathbf{r}_0(t)\right)_x = jt + x_0 \tag{A.131}$$

which cancels with the initial input in the integral form A.130. Furthermore the first order term of the expansion in ε also is zero as it is linear in the cartesian coordinates, just as is the term in equation A.117. Hence:

$$\left(\mathbf{r}_1(t \to \infty)\right)_x = 0. \tag{A.132}$$

To second order in ε we therefore recover for the delay integral:

$$\langle \Delta x \rangle_\infty^{\mathrm{PT}\ 2} = -\int_{-\infty}^{\infty} \mathrm{d}y_0 \int_0^{\infty} \mathrm{d}t' \left(\mathbf{J_f}(\mathbf{r}_0(t'))\mathbf{r}_1(t')\right)_x \tag{A.133}$$

where we introduced again the Jacobian matrix $\mathbf{J_f}$ as in the previous section.
This time we stay more general to avoid the lengthy calculations. Further we and write the general integral form, replacing $(x, y) = (x_1, x_2)$ to perform implicit summation over double indices:

$$\begin{aligned}
\langle \Delta x_i \rangle_\infty^{\mathrm{PT}\ 2} &= (-1)^i \int_{-\infty}^{\infty} \mathrm{d}y_0 \int_{-\infty}^{\infty} \mathrm{d}t \left(\mathbf{J_f}(\mathbf{r}_0(t))\right)_{i,j} \left(\mathbf{r}_1(t)\right)_j \\
&= (-1)^i \int_{-\infty}^{\infty} \mathrm{d}y_0 \int_{-\infty}^{\infty} \mathrm{d}t \ \ \partial_{x_j} \mathbf{f}_i(\mathbf{r}_0(t)) \int_{-\infty}^{t} \mathrm{d}t' \, \mathbf{f}_j(\mathbf{r}_0(t')) \\
&= (-1)^i \int_{-\infty}^{\infty} \mathrm{d}y_0 \int_{-\infty}^{\infty} \mathrm{d}t \int_{-\infty}^{t} \mathrm{d}t' \ \ \partial_{x_j} \mathcal{A}^{-1}_{i,k} \partial_{x_k} V(r)\Big|_{r=r_0(t)} \ \ \mathcal{A}^{-1}_{j,l} \partial_{x'_l} V(r')\Big|_{r'=r_0(t')} \\
&= (-1)^i \int_{-\infty}^{\infty} \mathrm{d}y_0 \int_{-\infty}^{\infty} \mathrm{d}t \int_{-\infty}^{t} \mathrm{d}t' \ \ \mathcal{A}^{-1}_{i,j} \mathcal{A}^{-1}_{k,l} \partial_{x_j} \partial_{x_k} V(r)\Big|_{r=r_0(t)} \ \ \partial_{x'_l} V(r')\Big|_{r'=r_0(t')} \\
&= (-1)^i \frac{1}{j^2} \int_{-\infty}^{\infty} \mathrm{d}y_0 \int_{-\infty}^{\infty} \mathrm{d}x \int_{-\infty}^{x} \mathrm{d}x' \, \mathcal{A}^{-1}_{i,j} \mathcal{A}^{-1}_{k,l} C_{j,k,l}(x, x', y_0)
\end{aligned} \tag{A.134}$$

Here we used again the substitution as in A.124 for t and t' and thus gain a prefactor $1/j^2$. Further we defined the integrand function $C_{j,k,l}(x, x', y_0)$ from which we can already conclude properties of the indices i, j, k, l:

$$C_{j,k,l}(x, x', y_0) \equiv \partial_{x_j} \partial_{x_k} V(r)\big|_{\mathbf{r}=(x,y_0)^{\mathrm{T}}} \ \ \partial_{x'_l} V(r')\Big|_{\mathbf{r}'=(x',y_0)^{\mathrm{T}}} = C_{k,j,l}(x, x', y_0). \tag{A.135}$$

From this function we see, that any combination of indices j, k, l, which yields an *odd* number of derivatives with respect to $x_2 = y$ will lead to $C_{j,k,l}(x, x', y_0)$ in total being odd in y_0. By the afterwards integration all functions odd in y_0 will vanish, therefore only combinations of indices are allowed, which lead to an even number of derivatives respected to $x_2 = y$:

$$(j, k, l) \in \{(1, 1, 1), (1, 2, 2), (2, 1, 2), (2, 2, 1)\}. \tag{A.136}$$

Furthermore, due to the special form of $\mathcal{A}^{-1}$ being a rotation and scaling matrix few more terms will cancel. To extract only the relevant terms, we rewrite the matrix elements of $\mathcal{A}^{-1}$ also with indices i, j, k, l, compare equation A.105,

$$\mathcal{A}^{-1}_{i,j} = \frac{1}{\gamma^2} \left(\delta_{i,j} \mathcal{D} + \varepsilon_{i,j,3} \mathcal{G}\right) \tag{A.137}$$

using the Kronecker delta $\delta_{i,j}$, which is one if both indices are equal and zero otherwise and the Levi-Civita symbol $\varepsilon_{i,j,k}$, which is one for even permutations and minus one for odd permutations of $(1,2,3)$ and zero otherwise. This leads:

$$\begin{aligned}\langle \Delta x_i \rangle_\infty^{\mathrm{PT}\,2} &\approx \frac{(-1)^i}{j^2\gamma^4}\int_{-\infty}^{\infty}\mathrm{d}y_0\int_{-\infty}^{\infty}\mathrm{d}x\int_{-\infty}^{x}\mathrm{d}x'\;\left(\delta_{i,j}\mathcal{D}+\varepsilon_{i,j,3}\mathcal{G}\right)\left(\delta_{k,l}\mathcal{D}+\varepsilon_{k,l,3}\mathcal{G}\right)C_{j,k,l}(x,x',y_0)\\ &\approx \frac{(-1)^i}{j^2\gamma^4}\int_{-\infty}^{\infty}\mathrm{d}y_0\int_{-\infty}^{\infty}\mathrm{d}x\int_{-\infty}^{x}\mathrm{d}x'\,p_{i,j,k,l}\,C_{j,k,l}(x,x',y_0) \qquad \text{(A.138)}\\ p_{i,j,k,l} &= \delta_{i,j}\delta_{k,l}\mathcal{D}^2+\left(\varepsilon_{i,j,3}\delta_{k,l}+\delta_{i,j}\varepsilon_{k,l,3}\right)\mathcal{D}\mathcal{G}+\varepsilon_{i,j,3}\varepsilon_{k,l,3}\mathcal{G}^2 \qquad \text{(A.139)}\end{aligned}$$

With this prefactor function $p_{i,j,k,l}$ and the constraints on the indices in equation A.136 as well as that C is unchanged when swapping the first two indices as in equation A.135, one can for a fixed index i very fast select the few contributing functions C. Let us start with the known result for the Hall effect, which is already given in equation A.129. In the notation we use now, the offset integral is recovered for $i=2$. With the so far gained constraints on the indices the remaining terms are:

$$\begin{aligned}\langle \Delta y \rangle_\infty^{\mathrm{PT}\,2} &= \frac{1}{j^2\gamma^4}\int_{-\infty}^{\infty}\mathrm{d}y_0\int_{-\infty}^{\infty}\mathrm{d}x\int_{-\infty}^{x}\mathrm{d}x'\,\mathcal{D}\mathcal{G}\left(-C_{1,1,1}-C_{2,2,1}\right)\\ &= -\frac{\mathcal{D}\mathcal{G}}{j^2\gamma^4}\int_{-\infty}^{\infty}\mathrm{d}y_0\int_{-\infty}^{\infty}\mathrm{d}x\int_{-\infty}^{x}\mathrm{d}x'\;\left((\partial_x^2+\partial_y^2)V(r)\big|_{\mathbf{r}=(x,y_0)^{\mathrm{T}}}\;\partial_{x'}V(r')\big|_{\mathbf{r}'=(x',y_0)^{\mathrm{T}}}\right)\\ &= -\frac{\mathcal{D}\mathcal{G}}{j^2\gamma^4}\int_{-\infty}^{\infty}\mathrm{d}(x,y_0)\;\left((\partial_x^2+\partial_y^2)V(r)\big|_{\mathbf{r}=(x,y_0)^{\mathrm{T}}}\;V(r)|_{\mathbf{r}=(x,y_0)^{\mathrm{T}}}\right)\\ &= -\frac{2\pi\mathcal{D}\mathcal{G}}{j^2\gamma^4}\int_0^{\infty}\mathrm{d}r\,V(r)\left(\partial_r r V'(r)\right)\\ &\overset{\text{P.I.}}{=} \frac{2\pi\mathcal{D}\mathcal{G}}{j^2\gamma^4}\int_0^{\infty}\mathrm{d}r\,r\,V'^2(r)\end{aligned} \qquad \text{(A.140)}$$

which exactly reproduces in a few lines the result from section A.2. Now we repeat the calculation for the delay integral which is $i=1$:

$$\begin{aligned}\langle \Delta x \rangle_\infty^{\mathrm{PT}\,2} &= -\frac{1}{j^2\gamma^4}\int_{-\infty}^{\infty}\mathrm{d}y_0\int_{-\infty}^{\infty}\mathrm{d}x\int_{-\infty}^{x}\mathrm{d}x'\,\mathcal{D}^2\left(C_{1,1,1}+C_{1,2,2}\right)+\mathcal{G}^2\left(C_{2,1,2}-C_{2,2,1}\right)\\ &= -\frac{1}{j^2\gamma^4}\int_{-\infty}^{\infty}\mathrm{d}y_0\int_{-\infty}^{\infty}\mathrm{d}x\int_{-\infty}^{x}\mathrm{d}x'\,\mathcal{D}^2\left(C_{1,1,1}+C_{2,2,1}\right)+\gamma^2\left(C_{1,2,2}-C_{2,2,1}\right) \qquad \text{(A.141)}\\ &= \frac{\mathcal{D}}{\mathcal{G}}\langle \Delta y \rangle_\infty^{\mathrm{PT}\,2}+\frac{1}{j^2\gamma^2}\int_{-\infty}^{\infty}\mathrm{d}y_0\int_{-\infty}^{\infty}\mathrm{d}x\int_{-\infty}^{x}\mathrm{d}x'\;\left(C_{1,2,2}-C_{2,2,1}\right)\end{aligned}$$

It is now left to show that the last term drops as after partial integrations the last terms cancel each other. The potential and all its derivatives vanish at infinity, hence all surface terms from the partial integrations drop.

$$\begin{aligned}\int_{-\infty}^{\infty}\mathrm{d}y_0\int_{-\infty}^{\infty}\mathrm{d}x\int_{-\infty}^{x}\mathrm{d}x'\,C_{1,2,2} &= \int_{-\infty}^{\infty}\mathrm{d}y_0\int_{-\infty}^{\infty}\mathrm{d}x\,\partial_x\partial_y V(r)\int_{-\infty}^{x}\mathrm{d}x'\,\partial_{y'}V(r')\\ &= -\int_{-\infty}^{\infty}\mathrm{d}y_0\int_{-\infty}^{\infty}\mathrm{d}x\,\partial_y V(r)\,\partial_y V(r)\end{aligned}$$

$$
\begin{aligned}
&= \int_{-\infty}^{\infty} \mathrm{d}y_0 \int_{-\infty}^{\infty} \mathrm{d}x\, \partial_y \partial_y V(r)\, V(r) \\
&= \int_{-\infty}^{\infty} \mathrm{d}y_0 \int_{-\infty}^{\infty} \mathrm{d}x\, \partial_y \partial_y V(r) \int_{-\infty}^{x} \mathrm{d}x'\, \partial_{x'} V(r') \\
&= \int_{-\infty}^{\infty} \mathrm{d}y_0 \int_{-\infty}^{\infty} \mathrm{d}x \int_{-\infty}^{x} \mathrm{d}x'\, C_{2,2,1}
\end{aligned}
\tag{A.142}
$$

Hence the we could prove that indeed $C_{1,2,2} - C_{2,2,1} = 0$ and therefore the last term drops. The final expression for the delay integral thus becomes:

$$
\langle \Delta x \rangle_{\infty}^{\mathrm{PT}\ 2} = \frac{\mathcal{D}}{\mathcal{G}} \langle \Delta y \rangle_{\infty}^{\mathrm{PT}\ 2} = \frac{2\pi \mathcal{D}^2}{j^2 \gamma^4} \int_0^{\infty} \mathrm{d}r\, r V'^{\,2}(r). \tag{A.143}
$$

Note that the gyrocoupling constant $\mathcal{G} = -4\pi$ is negative and hence the signs of the offset and the delay integral are different.

A.4. The Solution of the Thiele Equation for a Vacancy Wall

We want to solve the two-dimensional Thiele equation in the presence of a vacancy wall. For reasons of simplicity we rotate our system of coordinates such that the wall is on the y-axis at $x = 0$. Hence we have a potential $V(\mathbf{r})$ which we assume to decay exponentially in the x-direction and to be constant in the y-direction. The current density $\mathbf{j}$ we assume to be constant and $j_x > 0$, such that we approach the wall from the left. Using this condition, $x < 0$, and that we cannot overcome the wall, the potential can be written as:

$$
V(x) = a\, \mathrm{e}^{\frac{x}{\xi}} \tag{A.144}
$$

$$
\nabla V(x) = \frac{a}{\xi}\, \mathrm{e}^{\frac{x}{\xi}} \mathbf{e}_x. \tag{A.145}
$$

Plugging this potential into the simplified Thiele equation 2.26 yields:

$$
\begin{aligned}
\begin{pmatrix} \dot{x}(t) \\ \dot{y}(t) \end{pmatrix} &= -\frac{a}{\gamma^2 \xi}\, \mathrm{e}^{\frac{x(t)}{\xi}} \begin{pmatrix} \mathcal{D} & \mathcal{G} \\ -\mathcal{G} & \mathcal{D} \end{pmatrix} \begin{pmatrix} 1 \\ 0 \end{pmatrix} + \begin{pmatrix} j_x \\ j_y \end{pmatrix} \\
&= -\frac{a}{\gamma^2 \xi}\, \mathrm{e}^{\frac{x(t)}{\xi}} \begin{pmatrix} \mathcal{D} \\ -\mathcal{G} \end{pmatrix} + \begin{pmatrix} j_x \\ j_y \end{pmatrix}
\end{aligned}
\tag{A.146}
$$

Note that the first line only includes the variable x. Therefore we solve this line first, starting with a substitution to a dimensionless coordinate $x' = \frac{x}{\xi}$ and thus $\dot{x} = \xi \dot{x}'$ from which follows:

$$
\begin{aligned}
\dot{x}'(t) &= -\frac{a\mathcal{D}}{\gamma^2 \xi^2}\, \mathrm{e}^{x'(t)} + \frac{j_x}{\xi} \\
\Leftrightarrow\ \dot{x}'(t) - \frac{j_x}{\xi} &= -\exp\left[x'(t) + \ln\left(\frac{a\mathcal{D}}{\gamma^2 \xi^2} \right) \right].
\end{aligned}
\tag{A.147}
$$

Now we perform a further substitution $x'' = x' - \frac{j_x}{\xi}t + \ln\left(\frac{a\mathcal{D}}{\gamma^2\xi^2}\right)$ and the corresponding derivative $\dot{x}'' = \dot{x}' - \frac{j_x}{\xi}$ which yields:

$$\begin{aligned}
\dot{x}''(t) &= -\,\mathrm{e}^{x''(t)+\frac{j_x}{\xi}t} \\
\Leftrightarrow\ -\dot{x}''(t)\,\mathrm{e}^{-x''(t)} &= \mathrm{e}^{\frac{j_x}{\xi}t} \\
\Leftrightarrow\ -\int_{t_0}^{t}\mathrm{d}t'\dot{x}''(t')\,\mathrm{e}^{-x''(t')} &= -\int_{x_0''}^{x''(t)}\mathrm{d}x''\,\mathrm{e}^{-x''(t')} = \int_{t_0}^{t}\mathrm{d}t'\,\mathrm{e}^{\frac{j_x}{\xi}t'} \\
\Leftrightarrow\ \mathrm{e}^{-x''(t)} - \mathrm{e}^{-x''(t_0)} &= \frac{\xi}{j_x}\left(\mathrm{e}^{\frac{j_x}{\xi}t} - \mathrm{e}^{\frac{j_x}{\xi}t_0}\right)
\end{aligned} \tag{A.148}$$

such that we can plug in back the substitutions $x'' = \frac{x}{\xi} - \frac{j_x}{\xi}t + \ln\left(\frac{a\mathcal{D}}{\gamma^2\xi^2}\right)$ and recover:

$$\begin{aligned}
\mathrm{e}^{-x''(t)} &= \mathrm{e}^{-\frac{x(t)}{\xi}+\frac{j_x}{\xi}t-\ln\left(\frac{a\mathcal{D}}{\gamma^2\xi^2}\right)} = \frac{\xi}{j_x}\left(\mathrm{e}^{\frac{j_x}{\xi}t} - \mathrm{e}^{\frac{j_x}{\xi}t_0}\right) + \mathrm{e}^{-\frac{x_0}{\xi}+\frac{j_x}{\xi}t_0-\ln\left(\frac{a\mathcal{D}}{\gamma^2\xi^2}\right)} \\
\Leftrightarrow\ \mathrm{e}^{-\frac{x(t)}{\xi}} &= \frac{a\mathcal{D}}{\gamma^2\xi j_x}\left(1 - \mathrm{e}^{\frac{j_x}{\xi}(t_0-t)}\right) + \mathrm{e}^{-\frac{x_0}{\xi}+\frac{j_x}{\xi}(t_0-t)} \\
&= \mathrm{e}^{-\frac{x_0}{\xi}-\frac{j_x}{\xi}(t-t_0)}\left[1 + \frac{a\mathcal{D}}{\gamma^2\xi j_x}\,\mathrm{e}^{\frac{x_0}{\xi}}\left(\mathrm{e}^{\frac{j_x}{\xi}(t-t_0)} - 1\right)\right] \\
\Leftrightarrow\ x(t) &= x_0 + j_x(t-t_0) - \xi\ln\left[1 + \frac{a\mathcal{D}}{\gamma^2\xi j_x}\,\mathrm{e}^{\frac{x_0}{\xi}}\left(\mathrm{e}^{\frac{j_x}{\xi}(t-t_0)} - 1\right)\right].
\end{aligned} \tag{A.149}$$

This time-dependent solution for the x-coordinate we can now use to solve the second component of the differential equation A.146. Here we can just use the result of the second step in equation A.149, invert it and use it as an expression for the potential:

$$\begin{aligned}
\dot{y}(t) &= \frac{a\mathcal{G}}{\gamma^2\xi}\,\mathrm{e}^{\frac{x(t)}{\xi}} + j_y \\
&= \frac{a\mathcal{G}}{\gamma^2\xi}\frac{\mathrm{e}^{\frac{x_0}{\xi}+\frac{j_x}{\xi}(t-t_0)}}{1 + \frac{a\mathcal{D}}{\gamma^2\xi j_x}\,\mathrm{e}^{\frac{x_0}{\xi}}\left(\mathrm{e}^{\frac{j_x}{\xi}(t-t_0)} - 1\right)} + j_y \\
&= \frac{a\mathcal{G}}{\gamma^2\xi}\,\mathrm{e}^{\frac{x_0}{\xi}}\frac{1}{\frac{a\mathcal{D}}{\gamma^2\xi j_x}\,\mathrm{e}^{\frac{x_0}{\xi}} + \left(1 - \frac{a\mathcal{D}}{\gamma^2\xi j_x}\,\mathrm{e}^{\frac{x_0}{\xi}}\right)\mathrm{e}^{-\frac{j_x}{\xi}(t-t_0)}} + j_y \\
&= j_x\frac{\mathcal{G}}{\mathcal{D}}\frac{1}{1 + \left(\frac{\gamma^2\xi j_x}{a\mathcal{D}}\,\mathrm{e}^{-\frac{x_0}{\xi}} - 1\right)\mathrm{e}^{-\frac{j_x}{\xi}(t-t_0)}} + j_y \\
&= j_x\frac{\mathcal{G}}{\mathcal{D}}\frac{1}{1 + c\,\mathrm{e}^{-\frac{j_x}{\xi}(t-t_0)}} + j_y
\end{aligned} \tag{A.150}$$

with the time independent constant $c = \frac{\gamma^2\xi j_x}{a\mathcal{D}}\,\mathrm{e}^{-\frac{x_0}{\xi}} - 1$. Now we can integrate both sides of the equation over time to recover an expression for the time-dependent y-component:

$$\begin{aligned}
\int_{t_0}^{t}\mathrm{d}t'\dot{y}(t) &= \int_{t_0}^{t}\mathrm{d}t'\left\{j_x\frac{\mathcal{G}}{\mathcal{D}}\frac{1}{1 + c\,\mathrm{e}^{-\frac{j_x}{\xi}(t'-t_0)}} + j_y\right\} \\
\Leftrightarrow\ y(t) - y_0 &= j_y(t-t_0) + j_x\frac{\mathcal{G}}{\mathcal{D}}\int_{t_0}^{t}\frac{\mathrm{d}t'}{1 + c\,\mathrm{e}^{-\frac{j_x}{\xi}(t'-t_0)}}.
\end{aligned} \tag{A.151}$$

We now introduce a further substitution $t'' = \frac{j_x}{\xi}(t' - t_0)$, $\mathrm{d}t'' = \frac{j_x}{\xi}\mathrm{d}t'$ and solve the integral expression:

$$\begin{aligned} j_x \frac{\mathcal{G}}{\mathcal{D}} \int_{t_0}^{t} \frac{\mathrm{d}t'}{1 + c\,\mathrm{e}^{-\frac{j_x}{\xi}(t'-t_0)}} &= \xi \frac{\mathcal{G}}{\mathcal{D}} \int_0^{\frac{j_x}{\xi}(t-t_0)} \frac{\mathrm{d}t''}{1 + c\,\mathrm{e}^{-t''}} \\ &= \xi \frac{\mathcal{G}}{\mathcal{D}} \ln\left[c + \mathrm{e}^{t''}\right]\Big|_0^{\frac{j_x}{\xi}(t-t_0)} \\ &= \xi \frac{\mathcal{G}}{\mathcal{D}} \ln\left[\frac{c + \mathrm{e}^{\frac{j_x}{\xi}(t-t_0)}}{c+1}\right]. \end{aligned} \tag{A.152}$$

Finally we plug back in the lengthy expression $c + 1 = \frac{\gamma^2 \xi j_x}{a\mathcal{D}}\,\mathrm{e}^{-\frac{x_0}{\xi}}$ to obtain the final result for the time-dependent y-coordinate:

$$\begin{aligned} y(t) &= y_0 + j_y(t - t_0) + \xi \frac{\mathcal{G}}{\mathcal{D}} \ln\left[\frac{c + \mathrm{e}^{\frac{j_x}{\xi}(t-t_0)}}{c+1}\right] \\ &= y_0 + j_y(t - t_0) + \xi \frac{\mathcal{G}}{\mathcal{D}} \ln\left[1 + \frac{a\mathcal{D}}{\gamma^2 \xi j_x}\,\mathrm{e}^{\frac{x_0}{\xi}}\left(\mathrm{e}^{\frac{j_x}{\xi}(t-t_0)} - 1\right)\right]. \end{aligned} \tag{A.153}$$

Note that the logarithm is the same as for the x-coordinate. Further the first terms again just describe the movement of a free skyrmion and all corrections from the vacancy come from the last term. Hence we can combine the solutions for the two coordinates in one equation:

$$\mathbf{r}(t) = \mathbf{r}_0 + (t - t_0)\mathbf{j} - \frac{\xi}{\mathcal{D}} \ln\left[1 + \frac{a\mathcal{D}}{j_\mathrm{x}\gamma^2\xi}\mathrm{e}^{\frac{x_0}{\xi}}\left(\mathrm{e}^{\frac{j_\mathrm{x}}{\xi}(t-t_0)} - 1\right)\right]\begin{pmatrix}\mathcal{D}\\ -\mathcal{G}\end{pmatrix} \tag{A.154}$$

Of physical importance is the long time limit $t \gg t_0$. In this limit the logarithm becomes:

$$\begin{aligned} \xi \ln\left[1 + \frac{a\mathcal{D}}{j_\mathrm{x}\gamma^2\xi}\mathrm{e}^{\frac{x_0}{\xi}}\left(\mathrm{e}^{\frac{j_\mathrm{x}}{\xi}(t-t_0)} - 1\right)\right] &\approx \xi \ln\left[\frac{a\mathcal{D}}{j_\mathrm{x}\gamma^2\xi}\mathrm{e}^{\frac{x_0}{\xi}}\,\mathrm{e}^{\frac{j_\mathrm{x}}{\xi}(t-t_0)}\right] \\ &= \xi \ln\left[\frac{a\mathcal{D}}{j_\mathrm{x}\gamma^2\xi}\right] + x_0 + j_\mathrm{x}(t - t_0) \end{aligned} \tag{A.155}$$

which cancels exactly the terms that describe the free motion in x-direction apart from a constant.

$$\begin{aligned} x(t \gg t_0) &\approx x_0 + j_x(t - t_0) - \left(\xi \ln\left[\frac{a\mathcal{D}}{j_x\gamma^2\xi}\right] + x_0 + j_x(t - t_0)\right) \\ &= -\xi \ln\left[\frac{a\mathcal{D}}{j_x\gamma^2\xi}\right] \end{aligned} \tag{A.156}$$

$$\begin{aligned} y(t \gg t_0) &\approx y_0 + j_y(t - t_0) + \frac{\mathcal{G}}{\mathcal{D}}\left(\xi \ln\left[\frac{a\mathcal{D}}{j_x\gamma^2\xi}\right] + x_0 + j_x(t - t_0)\right) \\ &= y_0 + \frac{\mathcal{G}}{\mathcal{D}}x_0 + \left(j_y + \frac{\mathcal{G}}{\mathcal{D}}j_x\right)(t - t_0) + \frac{\mathcal{G}}{\mathcal{D}}\xi \ln\left[\frac{a\mathcal{D}}{j_x\gamma^2\xi}\right] \end{aligned} \tag{A.157}$$

References

[1] T. H. R. Skyrme. A Non-Linear Field Theory. *Proceedings of the Royal Society of London. Series A. Mathematical and Physical Sciences*, 260(1300):127–138, 1961.

[2] A. Bogdanov and A. Hubert. Thermodynamically stable magnetic vortex states in magnetic crystals. *Journal of Magnetism and Magnetic Materials*, 138(3):255–269, 1994.

[3] S. Mühlbauer, B. Binz, F. Jonietz, A. Rosch, A. Neubauer, R. Georgii, and P. Böni. Skyrmion Lattice in a Chiral Magnet. *Science*, 323, Februar 2009.

[4] T. Adams, S. Mühlbauer, C. Pfleiderer, F. Jonietz, A. Bauer, A. Neubauer, R. Georgii, P. Böni, U. Keiderling, K. Everschor, M. Garst, and A. Rosch. Long-Range Crystalline Nature of the Skyrmion Lattice in MnSi. *Phys. Rev. Lett.*, 107:217206, Nov 2011.

[5] Yu X. Z., Kanazawa N., Onose Y., Kimoto K., Zhang W. Z., Ishiwata S., Matsui Y., and Tokura Y. Near room-temperature formation of a skyrmion crystal in thin-films of the helimagnet FeGe. *Nat Mater*, 10(2):106–109, feb 2011. 10.1038/nmat2916.

[6] W. Münzer, A. Neubauer, T. Adams, S. Mühlbauer, C. Franz, F. Jonietz, R. Georgii, P. Böni, B. Pedersen, M. Schmidt, A. Rosch, and C. Pfleiderer. Skyrmion lattice in the doped semiconductor Fe1−xCoxSi. *Phys. Rev. B*, 81:041203, Jan 2010.

[7] Yu X. Z., Onose Y., Kanazawa N., Park J. H., Han J. H., Matsui Y., Nagaosa N., and Tokura Y. Real-space observation of a two-dimensional skyrmion crystal. *Nature*, 465(7300):901–904, jun 2010. 10.1038/nature09124.

[8] T. Adams, A. Chacon, M. Wagner, A. Bauer, G. Brandl, B. Pedersen, H. Berger, P. Lemmens, and C. Pfleiderer. Long-Wavelength Helimagnetic Order and Skyrmion Lattice Phase in Cu2OSeO3. *Phys. Rev. Lett.*, 108:237204, Jun 2012.

[9] Karin Everschor. *Current-Induced Dynamics of Chiral Magnetic Structures.* PhD thesis, Universität zu Köln, 2012.

[10] A. Neubauer, C. Pfleiderer, B. Binz, A. Rosch, R. Ritz, P. G. Niklowitz, and P. Böni. Topological Hall Effect in the A Phase of MnSi. *Phys. Rev. Lett.*, 102:186602, May 2009.

[11] Minhyea Lee, W. Kang, Y. Onose, Y. Tokura, and N. P. Ong. Unusual Hall Effect Anomaly in MnSi under Pressure. *Phys. Rev. Lett.*, 102:186601, May 2009.

[12] Schulz T., Ritz R., Bauer A., Halder M., Wagner M., Franz C., Pfleiderer C., Everschor K., Garst M., and Rosch A. Emergent electrodynamics of skyrmions in a chiral magnet. *Nat Phys*, 8(4):301–304, apr 2012. 10.1038/nphys2231.

[13] Michael Stone. Magnus force on skyrmions in ferromagnets and quantum Hall systems. *Phys. Rev. B*, 53:16573–16578, Jun 1996.

[14] F. Jonietz, S. Mühlbauer, C. Pfleiderer, A. Neubauer, W. Münzer, A. Bauer, T. Adams, R. Georgii, P. Böni, R. A. Duine, K. Everschor, M. Garst, and A. Rosch. Spin Transfer Torques in MnSi at Ultralow Current Densities. *Science*, 330(6011):1648–1651, 2010.

[15] Karin Everschor, Markus Garst, R. A. Duine, and Achim Rosch. Current-induced rotational torques in the skyrmion lattice phase of chiral magnets. *Phys. Rev. B*, 84:064401, Aug 2011.

[16] Karin Everschor, Markus Garst, Benedikt Binz, Florian Jonietz, Sebastian Mühlbauer, Christian Pfleiderer, and Achim Rosch. Rotating skyrmion lattices by spin torques and field or temperature gradients. *Phys. Rev. B*, 86:054432, Aug 2012.

[17] Pfleiderer Christian and Rosch Achim. Condensed-matter physics: Single skyrmions spotted. *Nature*, 465(7300):880–881, jun 2010. 10.1038/465880a.

[18] Yu X.Z., Kanazawa N., Zhang W.Z., Nagai T., Hara T., Kimoto K., Matsui Y., Onose Y., and Tokura Y. Skyrmion flow near room temperature in an ultralow current density. *Nat Commun*, 3:988, aug 2012. 10.1038/ncomms1990.

[19] Iwasaki Junichi, Mochizuki Masahito, and Nagaosa Naoto. Universal current-velocity relation of skyrmion motion in chiral magnets. *Nat Commun*, 4:1463, feb 2013. 10.1038/ncomms2442.

[20] Shi-Zeng Lin, Charles Reichhardt, Cristian D. Batista, and Avadh Saxena. Driven Skyrmions and Dynamical Transitions in Chiral Magnets. *Phys. Rev. Lett.*, 110:207202, May 2013.

[21] Shi-Zeng Lin, Charles Reichhardt, Cristian D. Batista, and Avadh Saxena. Particle model for skyrmions in metallic chiral magnets: Dynamics, pinning, and creep. *Phys. Rev. B*, 87:214419, Jun 2013.

[22] Niklas Romming, Christian Hanneken, Matthias Menzel, Jessica E. Bickel, Boris Wolter, Kirsten von Bergmann, André Kubetzka, and Roland Wiesendanger. Writing and Deleting Single Magnetic Skyrmions. *Science*, 341(6146):636–639, 2013.

[23] SampaioJ., CrosV., RohartS., ThiavilleA., and FertA. Nucleation, stability and current-induced motion of isolated magnetic skyrmions in nanostructures. *Nat Nano*, 8(11):839–844, nov 2013.

[24] Nagaosa Naoto and Tokura Yoshinori. Topological properties and dynamics of magnetic skyrmions. *Nat Nano*, 8(12):899–911, dec 2013.

[25] R. A. Duine, A. S. Núñez, Jairo Sinova, and A. H. MacDonald. Functional Keldysh theory of spin torques. *Phys. Rev. B*, 75:214420, Jun 2007.

[26] M. E. Lucassen, H. J. van Driel, C. Morais Smith, and R. A. Duine. Current-driven and field-driven domain walls at nonzero temperature. *Phys. Rev. B*, 79:224411, Jun 2009.

[27] S. Zhang and Z. Li. Roles of Nonequilibrium Conduction Electrons on the Magnetization Dynamics of Ferromagnets. *Phys. Rev. Lett.*, 93:127204, Sep 2004.

[28] Karin Everschor. Manipulating Magnetic Structures in Chiral Metals by Currents, June 2009.

[29] A. A. Thiele. Steady-State Motion of Magnetic Domains. *Phys. Rev. Lett.*, 30:230–233, Feb 1973.

[30] J. He, Z. Li, and S. Zhang. Current-driven vortex domain wall dynamics by micromagnetic simulations. *Phys. Rev. B*, 73:184408, May 2006.

[31] Christoph Schütte, Junichi Iwasaki, Achim Rosch, and Naoto Nagaosa. Inertia, diffusion and dynamics of a driven skyrmion. dec 2013.

[32] C. Schütte and M. Garst. Magnon-skyrmion scattering in chiral magnets. *ArXiv e-prints*, May 2014.

[33] Iwasaki Junichi, Mochizuki Masahito, and Nagaosa Naoto. Current-induced skyrmion dynamics in constricted geometries. *Nat Nano*, 8(10):742–747, oct 2013.

Danksagung

Ich möchte *Prof. Dr. Achim Rosch* danken für die exzellente Betreuung bei der Masterarbeit: von der Auswahl eines Themas, welches mir viel Freude bereitet hat, über viele kontroverse Diskussionen bis hin zur Fertigstellung der Arbeit. Sein physikalisches Verständnis und seine Intuition erstaunten mich immer wieder und ich denke viel davon für meine weitere akademische Laufbahn mitnehmen zu können. Außerdem danke ich für die Ermöglichung der Teilnahmen an den Workshops und Konferenzen meiner Wahl und der Unterstützung dabei.
Besonderer Dank geht auch an *Dr. Christoph Schütte*. Teile des Basisprogramms der LLG-Iteration stammen aus seiner Arbeit, auf der meine basiert, und er nahm sich immer Zeit für die Beantwortung meiner Fragen und für Diskussionen.
Danke auch an die *BCGS*, Bonn-Cologne Graduate School of Physics and Astronomy, für die finanzielle und bildende Unterstützung während meines Masters und insbesondere *Prof. Dr. Corinna Kollath*, die mich als meine zweite Mentorin nach Herrn Rosch ebenfalls exzellent betreut hat.
Weiterhin danke ich den Mitgliedern der Arbeitsgruppen Rosch, Trebst und Bulla. Das Arbeitsklima ist immer enorm freundlich und motivierend und ich bin froh an dieser Gruppendynamik teilhaben zu dürfen. Hier möchte ich besonders *Jonathan Lux* danken, der mich in den Umgang mit *Mathematica* eingewiesen hat, sowie *Christopher Max*, der sich immer meinen mathematischen Fragen stellen musste.
Zuletzt danke ich noch meiner Familie. Ohne sie wäre diese Arbeit nicht in der Kürze der Zeit zustande gekommen, wenn sie am Ende leider doch etwas zu lange gedauert hat. Danke daher auch für den Rückhalt in den schwierigen Situationen abseits der Physik.

Eigenständigkeitserklärung

Hiermit versichere ich, dass ich die vorliegende Arbeit selbstständig verfasst und keine anderen als die angegebenen Quellen und Hilfsmittel verwendet habe, sowie Zitate als solche kenntlich gemacht habe.

Köln, 30. Juni 2014 .....

Jan Müller